Applied Bionics and Biomechanics

Biomechanical Perspectives in Traumatic Events

Lead Guest Editor: Christopher Rene# Torres-San Miguel
Guest Editors: Guillermo Manuel Urriolagoita Caldero#n, Luis Martínez-Sáez, and Dante Eli#as

Biomechanical Perspectives in Traumatic Events

Applied Bionics and Biomechanics

Biomechanical Perspectives in Traumatic Events

Lead Guest Editor: Christopher Rene# Torres-San Miguel
Guest Editors: Guillermo Manuel Urriolagoita Caldero#n, Luis Martínez-Sáez, and Dante Eli#as

Contents

Hindawi
Applied Bionics and Biomechanics
Volume 2021, Article ID 9922210, 13 pages
https://doi.org/10.1155/2021/9922210

Research Article

Numerical Assessment of a Safety System to Minimize Injuries during a Cyclist Run-Over

E. H. López-García,[1] **M. F. Carbajal-Romero**,[1] **J. A. Flores-Campos**,[2] **and C. R. Torres-SanMiguel**[3]

[1]*Instituto Politécnico Nacional, Escuela Superior de Ingeniería Mecánica y Eléctrica Sección de Estudios de Posgrado e Investigación, Azcapotzalco, 02519 CDMX, Mexico*
[2]*Instituto Politécnico Nacional, Unidad Profesional Interdisciplinaria en Ingeniería y Tecnologías Avanzadas, 07340 CDMX, Mexico*
[3]*Instituto Politécnico Nacional, Escuela Superior de Ingeniería Mecánica y Eléctrica Sección de Estudios de Posgrado e Investigación, Zacatenco, 07738 CDMX, Mexico*

Correspondence should be addressed to C. R. Torres-SanMiguel; ctorress@ipn.mx

Received 19 March 2021; Revised 18 July 2021; Accepted 11 August 2021; Published 27 August 2021

Academic Editor: Wen-Ming Chen

Background. The World Health Organization has reported that 1.35 million people die on the roads every year due to road traffic accidents. This paper focuses on exploring a passive safety system that reduces lesions in the overtaking run-over scenario. *Methods*. Head Injury Criterion (HIC) and Combined Thoracic Index (CTI) were evaluated through numerical simulations using LS-Dyna®; in order to compare the computed results, three different speed scenarios were carried out (velocity of running over 40, 50, 60 km/h). *Results*. The computed results were divided into groups, A for the run-over test without a passive security system and B for the run-over test with a passive security system. For case A.1, the HIC15 was 3325. For case A.2, the HIC15 was 1510, and for case A.3, the HIC 15 was 1208. For case B.1, the HIC15 2605, for case B.2, the HIC15 was 1282, and for case B.3, the HIC was 730. *Conclusion*. The comparative results show that the passive safety system installed on the bicycle has an increased benefit impact on the severity of the injury on vulnerable road users, decreasing the probability of cranioencephalic lesions in all study cases. In addition, the thorax injuries are cut down only in the impact scenario at a speed of 40 km/h.

1. Introduction

The World Health Organization (WHO) reported 1.35 million deaths in a year due to road traffic crashes [1]. This problem was the leading cause of death in people between 15 and 29 years in 2012 [2]. A specific group called vulnerable road users (VUR) that include motorcyclist, cyclist, and pedestrians are exposed to a greater danger during their circulation inroads because they do not have any structure that protects them from a road accident and is more susceptible suffer severe or deadly injuries [3]. The cyclist run-over is the smallest group among all road accidents, representing 4% of the victims. Although the numbers of deaths due to the cyclist run-over are a few, it was informed around 52,000 in 2013 [2]. In the United States, 783 cases of cyclist deaths due to motor vehicle crashes were reported in 2017 [4], while in Mexico, the cases of death of cyclists in road accidents totaled 199 in the same year [5]. The cyclist run-over scenarios can be identified according to different characteristics. The Pedestrian and Bicycle Crash Analysis Tool (PBCAT) distinguishes around 79 scenarios that consider different factors such as the vehicle's position before the impact, the direction in which one respects the other, and the impact causes [6]. The scenario reported a greater probability of cyclist death, where the motor vehicle is moving in the same direction as the cyclist and the bicycle is reached in the rear side by the front of the car; this scenario is called the overtaking scenario [7, 8]. Also, in National Highway Traffic

Safety Administration (NHTSA) in the database called Fatality Analysis Reporting System (FARS) from 2008 to 2012, the crash scenario that presented the highest death rate of the cyclist in the United States is the overtaking crash scenario [9], repeating this trend in subsequent years until 2017, which is the last update. It is essential to consider the type of motor vehicle studied because this directly affects the severity of the injury that a cyclist can present since its geometric characteristics alter the VUR kinematics. The data issued by the NHTSA show that passenger cars have the second place in deaths caused to cyclists [10–12]. In different industrial designs, existing systems are used to decrease injuries in vulnerable road users, as shown below: the patent [13] presents a bumper used in children's bicycles that has the function of attenuating the frontal collision in front of any surface to protect the bicycle upon impact and reduce the impact force and protect the user. Similarly, the patent [14] presents a pneumatic bumper with an internal chamber that stores air, which is released controlled when the front and rear parts of the bumper cushion impact. Also, the device [15] is designed to be used in motor vehicles. It has two subsystems, an impact mitigation device placed in the front of the vehicle, responsible for absorbing minor impacts that do not exceed the material's yield point, and an internal bumper that deforms plastically and absorbs the impact energy. The patent [16] consists of a U-shaped bumper joined at the motorcycle to protect the vehicle structure from possible shocks. The device [17] is a rigid structure installed on the front or rear of a bicycle to protect the damage by an impact. Finally, the patent [18] shows a bumper placed on the rear wheel of the bicycle, serving as a support for a light source projected towards the ground, marking the minimum safe distance for the circulation of the cyclist to prevent road accidents caused by the lack of vision towards the cyclist.

The research is aimed at proposing a framework used to perform vehicle-bicycle crash simulations to investigate the effects of the rear rubber bumper on cyclist injuries. The novelty is the rear passive safety system rubber bumper and the numerical analysis carried out. The modeling methods used to predict biomechanical responses for run-over simulations are well-established and can help predict biomechanical response in this scenario. A sedan vehicle was chosen for this study due to its high commercial demand and its incidence in cyclists' road accidents. In addition, the head and chest lesions suffered by the cyclist are evaluated since those are the body's main region that causes a person's death in run-over scenarios.

2. Materials and Methods

Three cyclists' crash impact simulations were carried out using the finite element method by Ls-Dyna® Software, through a detailed analysis due to the high nonlinearities, the inertial components, and the short duration of the phenomenon. All the simulations are carried out in the overtaking crash scenario, where the car impacts the bicycle's rear wheel while the bicycle and the vehicle are in the same direction [19]. The characteristics for each case of run-over are described in Table 1.

Table 1: Characteristics of run-over tests.

Group A (without passive security system)	Case A.1	
	Automobile speed	Cyclist speed
	60 km/h	0 km/h
	Case A.2	
	Automobile speed	Cyclist speed
	50 km/h	0 km/h
	Case A.3	
	Automobile speed	Cyclist speed
	40 km/h	0 km/h
Group B (with passive security system)	Case B.1	
	Automobile speed	Cyclist speed
	60 km/h	0 km/h
	Case B.2	
	Automobile speed	Cyclist speed
	50 km/h	0 km/h
	Case B.3	
	Automobile speed	Cyclist speed
	40 km/h	0 km/h

Bicycle and cyclist position was proposed before the vehicle's impact to measure injuries generated under the cyclist's head. The initial position before impact can be seen in Figure 1.

Three meshed models corresponding to the vehicle, bicycle, and cyclist were used, described in detail below. The automobile model consists of a meshed geometry compatible with the Ls-Dyna® software of a Toyota Yaris 2010, developed by George Mason University, contracted by the Federal Highway Administration (FHWA). This model has validations under the various frontal and lateral impact tests and a substantial barrier impact [20]. The anthropomorphic virtual dummy used during the simulations to represent the cyclist run-over scenario corresponds to a male Hybrid III percentile 50th, developed by the Livermore Software Technology Corporation, developing the LS-Dyna® software. The bicycle model was developed in the SolidWorks® Computer-Aided Design (CAD) software to later export the geometry to the LS-Dyna® software, where it proceeded to mesh and configure the corresponding contacts and joints. The bicycle frame was based on the Bicyclist and bike targets specifications manual version 1.1, developed by CATS/4a companies, to provide the necessary specifications of a cyclist objective vehicle detection tests. This research used the size of bicycles for an average man in the Dutch population [21]. The characteristics of the vehicle, dummy, and bicycle model are shown in Table 2.

The bicycle frame and wheel discretization were made with shell elements. The element type used in the model was quadrangular elements with 4 nodes, and we used the mesh algorithm provided by the LS-PrePost® software to create a preliminary mesh, then carried out a manual mesh refinement process to achieve a high mesh quality, especially in areas of interest of the model, where correct discretization is critical for the reliability of the results. To ensure that the quality of the mesh was acceptable, mesh quality checks

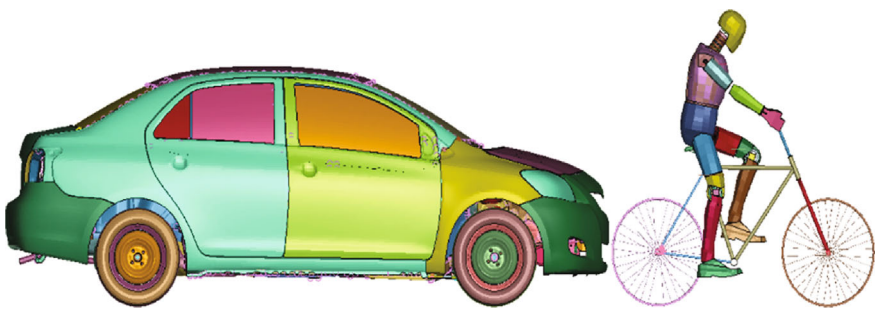

Figure 1: Initial position cyclist/automobile.

Table 2: Toyota Yaris 2012 and Hybrid III 50th percentile characteristics [20, 21].

Model characteristics	Yaris 2012	Hybrid 50th	Bicycle
Number of parts	919	115	12
Number nodes	393165	7353	53314
Number of solid elements	15234	2644	—
Number of shell elements	358457	1606	56724
Number of beam elements	4685	3	—
Number of restriction joints	19	48	—

shown in Table 3 were carried out, where it was observed that the mesh of the bicycle parts had a good quality, especially in critical areas for the results.

The LS-Dyna® software has a large number of material models used for different applications. For this research, to represent the behavior of the metallic parts, bicycle, and the passive safety device, we used the MAT_PIECEWISE_LINEAR_PLASTICITY model. The material selected for the bicycle frame was AISI 4130 steel, a common material for bicycle frames. In order to properly simulate impact behavior, the material's linear and nonlinear mechanical properties are needed to be configured appropriately within LS-PrePost®. Table 4 shows the parameters necessary to define those mechanical properties.

The bicycle frame was validated through the tests described in Mexican Standards nmx-d-198-2-1985 and nmx-d-198-3-1985, specifically in points 4.3.1 and 4.3.2 corresponding to the mass impact test in frame-scissor assembly and drop of the frame-scissor assembly, respectively, which were performed in LS-Dyna®. The frame drop safety test consists of fixing the frame's rear axle, then a mass (M1) of 70 kg must be fixed on the seat post, and the assembly is dropped on a steel anvil [22]. The conditions necessary for the bicycle frame to be considered safe are as follows:

(i) The frame must not suffer any visible fracture [22]

(ii) The permanent deformation measured between the initial and final position of the center of the front axle of the wheel must not exceed 60 mm [22]

In the frame impact safety test, a mass (M) of 22.5 kg was dropped from a height (a) of 180 mm and hit the front part aligned with the centers of the wheels [22]. Therefore, the parameters necessary for the bicycle frame to be considered safe must meet two conditions:

(i) The frame must not suffer any visible fracture [22]

(ii) The permanent deformation measured between the wheel axles' centers must not exceed 40 mm [22]

Figure 2 shows the diagram for the frame drop safety test and frame impact safety test.

2.1. Passive Safety Device. The strain energy density influences the severity of cyclist's injuries. This property quantifies the stored and dissipated energy in a material when it suffers a deformation. This energy is quantified from the different parts of the virtual dummy that represents the cyclist's body. Therefore, the passive safety device seeks to dissipate the most significant deformation energy before the cyclist's body hits the car's surface. The graphic method of material selection is used, also called the Ashby method [24].

The device was based on automotive bumpers systems consisting of a frame, an energy absorber, and a plastic fascia. A passive safety system was designed, consisting of a frame made of ASIS 201 stainless steel and a polyurethane rubber elastic energy absorption system. These materials were chosen due to their high capacity to absorb impact energy. The frame part is responsible for absorbing the most outstanding amount of plastic deformation energy from being run over by a vehicle. In contrast, the polyurethane rubber parts seek to protect minor impacts by absorbing the most significant elastic deformation energy. The assembly of the system is carried out through arrangements of nuts and screws. The system dimensions were established for the bumper's average height, which was used to place the bicycle's passive safety system. Since the average height of a vehicle's bumper is 500 mm [25], the system must be placed within this measurement. Figure 3 shows how the passive safety system is mounted on a bicycle.

The passive safety device's frame was discretized similarly to the bicycle's frame by using shell elements to optimize computational resources without sacrificing accuracy. Mesh quality check results are shown in Table 2. The material model was again MAT_PIECEWISE_LINEAR_PLASTICITY due to the characteristics already described; the mechanical properties necessary to simulate the correct

Table 3: Mesh quality checks for bicycle and passive security system model.

Variable	Definition	Acceptable value	Percentage of valid elements	Percentage of valid elements
Aspect ratio	The ratio between the largest and smallest dimensions of an element	<10	99.76%	99.86%
Skewness	Angular deviation of the element from an ideal shape	<45°	97.51%	99.95%
Warp angle	The angle between the normal two planes is formed by split the quadrilateral element along the diagonals	<100°	99.36%	99.46%

Table 4: Mechanical properties of AISI 4130 and AISI 201 Steel.

Material	Mass density. (Ton/mm^3)	E (MPa)	Poisson's ratio	σ_{YS} (MPa)	$\widetilde{\sigma_R}$ (MPa)	$\widetilde{\varepsilon_f}$	n	E_t (MPa)
AISI 4130	$7.850\times$	205×10^3	0.29	460.00	914.481	0.224	0.1456	2.48
AISI 201	7.810×10^{-9}	200×10^3	0.27	360.00	1377.5	.03715	0.2099	2.61

E = Young's modulus; σ_{YS} = yield stress; $\widetilde{\sigma_R}$ = true fracture stress; $\widetilde{\varepsilon_f}$ = true fracture strain; n = strain hardening exponent; E_t = tangent modulus.

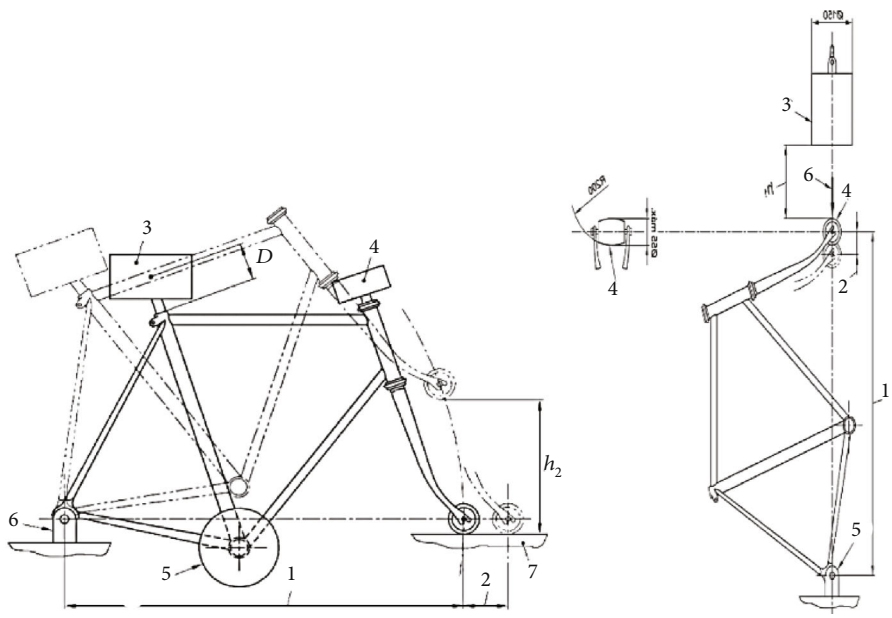

Figure 2: Frame drop safety test and frame impact safety test [23].

impact behavior are shown in Table 3. In polymer blocks, the MAT_MOONEY-RIVLIN_RUBBER model specialized in this group of materials was used. The mechanical properties necessary to simulate the behavior of this part of the passive safety device are shown in Table 5.

3. Results

The safety framework tests were carried out to bring the following results. First, the front scissors' axis's deformation was measured at the maximum position upon reaching rest (at time $t = 2000$ ms) against the position instants before hitting the rigid wall (at time $t = 752.0$ ms). Figure 4 shows the stages of the frame drop test and the results, where the maximum deformation was 3 mm, indicating that this value is established by the standard on which the tests are based.

The axis deformation at the front scissors was measured at the maximum position when the impactor is not in contact with the bicycle's frame to measure the permanent deformation in it. Figure 5 shows the stages of the frame impact test and the results where the permanent deformation (without load) presented in the frontal part of the frame was 16.7 mm, being within the tolerable limits of permanent deformation indicated by the standards on which the simulations are based.

3.1. Vehicle-Cyclist Impact Simulations. Bodily, the injuries happen when its resistance exceeds the withstand energy. Thus, for an object to lose speed, its energy of motion must

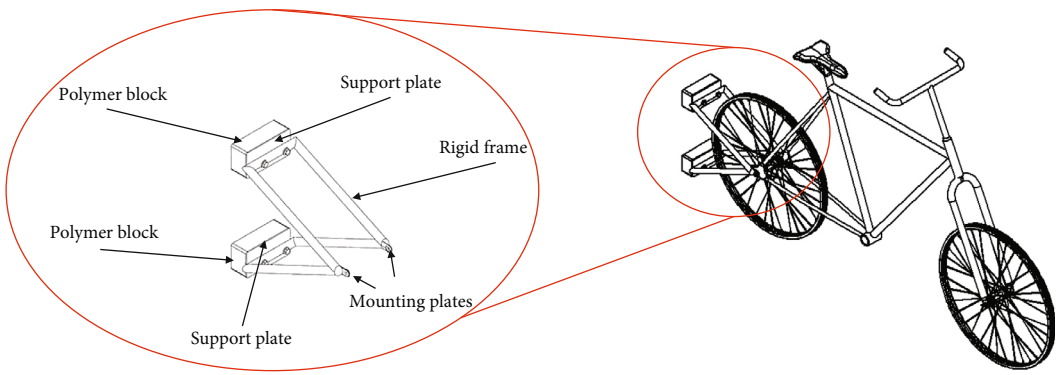

Figure 3: Passive security system fixed to the bicycle.

be transferred to another object. This transfer of energy also occurs in the case of an accident in the human body. The kinetic energy dissipated during the cyclist's collision is transformed into the structure deformation, leaving less residual energy to be absorbed for the mechanical properties of the hard and soft tissue. The dispersion of kinetic energy, both in space and in time, is determinant in reducing the severity of injuries and can make the difference between surviving and not. The most severely injured body areas are the head and thorax. In this research, Head Injury Criterion (HIC) and Combined Thoracic Index (CTI) determine the energy generated during the cyclist's collision. These injury rates are calculated according to the following equations.

A suitable measurement to scale the possible cranioencephalic injuries is used the HIC. This criterion reflects the change in acceleration that the passenger's head undergoes moments after the collision. The calculation is performed by selecting the maximum limits of integration of the area under the acceleration curve. NHTSA and AAMA (American Association of Medical Assistants) have established a time interval of 15 milliseconds after the impact. This interval favors the reduction of the HIC calculation error. In addition, this value provides a more rigorous measurement of injury probability.

$$\mathrm{HIC} = \left\{ (t2 - t1) \left[\frac{1}{t2 - t1} \int_1^2 a(t)dt \right]^{2.5} \right\}. \quad (1)$$

HIC uses $t2$ and $t1$ as a period of deceleration curve, a is the acceleration, and t is the total period of the curve. In order to determine a HIC value, it is necessary to obtain the velocity and acceleration of the body at the moment of impact. Therefore, the dummy's dimensional characteristics are crucial to establish a way to generate such kinematic parameters.

Additionally, the Combined Thoracic Index sums the ribs and skin deflection, measured on cadavers using chest bands. However, the chest deflections measured on the dummy represent only the internal chest deflections of the ribs. Thus, the combined thoracic injury criteria, CTI, is defined with the following equation

$$\mathrm{CTI} = \frac{A_{\max}}{A_{\mathrm{int}}} + \frac{D_{\max}}{D_{\mathrm{int}}}, \quad (2)$$

Table 5: Mechanical properties of polyurethane rubber with Mooney-Rivlin formulation.

Mass density (Ton/mm^3)	Poisson's ratio	A	B
1.20 ×	0.27	1.24	0.01

A and B are the constants of the Mooney-Rivlin constitutive equation for rubber. In the case of polyurethane rubber, the corresponding coefficients are $A = 1.24$ and $B = 0.01$ [26].

where $A_{\max}$ is the maximum value of 3 ms clip spinal acceleration (As), $D_{\max}$ is the maximum value of the dummy deflection (D), and A_{int} and D_{int} are the respective intercepts as defined above.

The dummy used has accelerometers in different parts of the body. For example, the accelerometer location in the head is at node 133919, while that of the thorax is node 135705, shown in Figure 6. Those nodes measure the accelerations, and the LSDyna software calculates the HIC and CTI reached during the run-over.

This section shows the results of simulations performed with the characteristics mentioned in Table 6, evaluating the cyclist's head injuries HIC and the CTI index for chest injuries. The simulation results were compared in two cases with the same vehicle's same speed but with and without a passive safety system to observe the injuries differences.

3.2. Comparison between Case A.1 and Case B.1. For the case in which the car moves at 60 km/h, Figure 7 shows the kinematic of the cyclist in cases A.1 and B.1, while Table 6 shows the corresponding HIC and CTI values. Finally, Figure 8 shows the required parameters to assess head and thorax injury severity at 60 km/h.

By using the results of the Combined Thoracic Index acceleration of the chest center of gravity as well as chest deflection during a traffic accident, it is possible to know the probability that the cyclist suffers AIS ≥ 3 and AIS ≥ 5 injuries is 99.23% and 43.22%, respectively, for case A.1. For case B.1, the probabilities are 99.58% and 55.77%, respectively.

3.3. Comparison between Case A.2 and Case B.2. For the case in which the car moves at 50 km/h, Figure 9 shows the kinematics of cyclists in cases A.2 and B.2, while Table 6 shows the corresponding HIC and CTI values. Finally, Figure 10

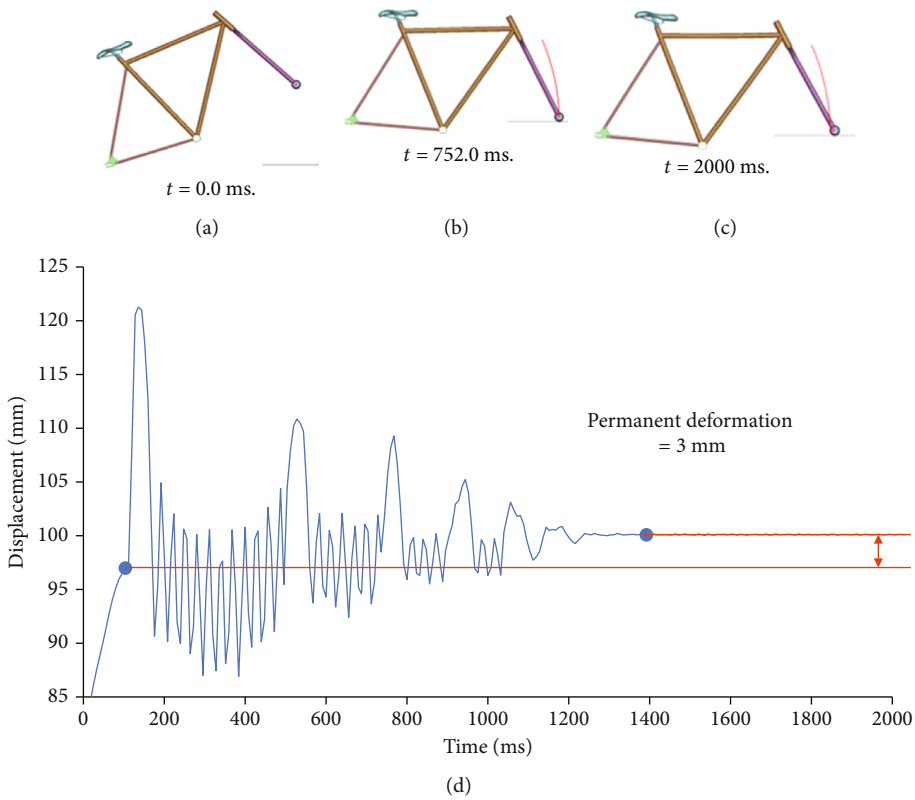

Figure 4: Front scissors' deformation: (a) initial position of the frame drop test; (b) moment before impact; (c) maximum permanent deformation position; (d) longitudinal displacement of the center of the front scissors' axis for the frame drop test.

shows the required parameters to assess head and thorax injury severity at 50 km/h.

By using the results of the Combined Thoracic Index acceleration of the chest center of gravity as well as chest deflection during a traffic accident, it is possible to know the probability that the cyclist suffers AIS ≥ 3 and AIS ≥ 5 injuries is 94.72% and 13.23%, respectively, for case A.2. For case B.2, the probabilities are 97.37% and 21.54%, respectively.

By obtaining the resulting acceleration graph at the center of gravity of the cyclist's head in both cases, it is possible to know that the HIC15 parameter is 1510 for case A.2, while for case B.2, it is 1282. This difference is because there is less acceleration in the center of gravity of the cyclist's head. After all, the safety device modifies the cyclist's kinematics during a collision, causing that the head hits closer to the center of the vehicle's windshield, as shown in Figure 11(b), which is less rigid than the contour.

3.4. Comparison between Case A.3 and Case B.3. For the case in which the car moves at 40 km/h, Figure 12 shows the cyclist's kinematics in cases A.3 and B.3, while Table 6 shows the corresponding HIC and CTI values. Finally, Figure 13 shows the required parameters to assess head and thorax injury severity at 50 km/h.

The HIC and the Abbreviated Injury Scale (AIS) correlation is estimated life-threatening without the passive security system. On the other hand, with the device being installed, the results show that HIC15 turns out to be close to the limit allowed by the Federal Motor Vehicle Safety Standards (FMVSS) [26, 27], and the injuries that the cyclist may have ranged from moderate to minor.

By using the results of the Combined Thoracic Index acceleration of chest center of gravity as well as chest deflection during a traffic accident, it is possible to know the probability that the cyclist suffers AIS ≥ 3 and AIS ≥ 5 injuries is 97.79% and 24.09%, respectively, for case A.3. For case B.3, the probabilities are 80.77% and 4.48%, respectively.

4. Discussion

It shows that the kinematics of the cyclist during impact is quite similar to the results obtained in the present work, as shown in Figure 14. In addition, the HIC parameters for cases of 50 km/h and 40 km/h are quite similar when presenting only 9.32% and 6.09% errors, respectively, compared to their tests. Only when the impact is at 60 km/h, the results differ from each other. It can be explained due to the different geometry between the fronts of the vehicles used because the cyclist's head hits a higher area of the windshield at this speed, which has a higher stiffness, which significantly increases HIC. On the other hand, Raslavicius et al. use a multibody solver, while this work uses a finite element model that can make specific differences in body deformations in contact during impact [7]. The results obtained are steady with the severity of the literature's injuries by agreeing that this crash scenario generates severe or fatal injuries [8, 28].

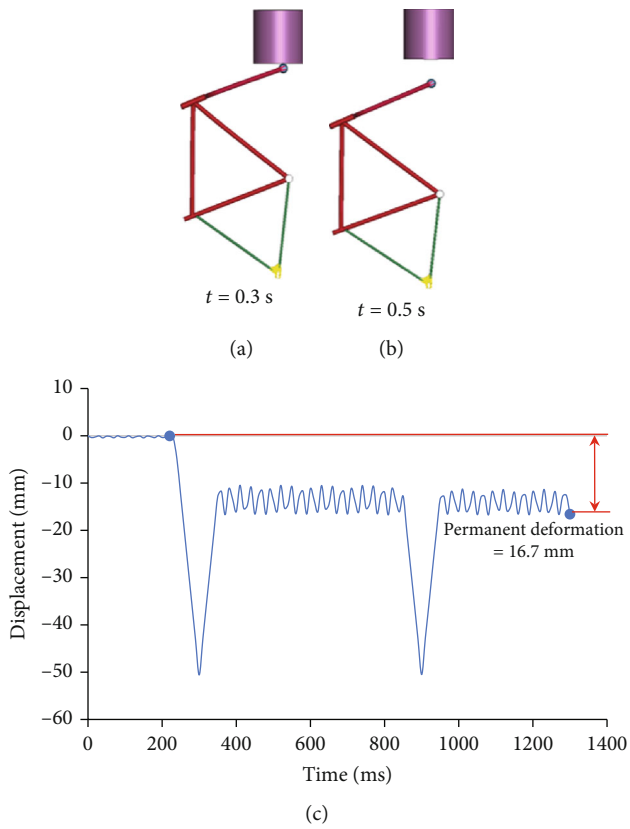

Figure 5: Frame deformation: (a) frame contact with impactor; (b) moment after contact with impactor (maximum permanent deformation); (c) longitudinal displacement of the center of the front scissors' axis for frame impact safety test.

Figure 6: The head and thorax accelerometer location.

Table 6: Evaluation of HIC 15 and CTI with and without a passive safety system.

Velocity	Case	HIC15	AIS head	CTI	AIS chest
60 km/h	A.1	3325	AIS ≥ 6	1.933	AIS ≥ 5 = 55.77%
60 km/h	B.1	2605	AIS ≥ 5	2.03	AIS ≥ 5 = 43.22%
50 km/h	A.2	1510	AIS ≥ 5	1.62	AIS ≥ 5 = 21.54%
50 km/h	B.2	1282	AIS ≥ 4	1.73	AIS ≥ 5 = 13.23%
40 km/h	A.3	1208	AIS ≥ 4	1.76	AIS ≥ 5 = 24.09%
40 km/h	B.3	730	AIS ≥ 3	1.39	AIS ≥ 5 = 4.48%

The vehicle model used in this work was validated under the various front and lateral impact tests [20], the dummy model was provided by Livermore Software Technology Corporation, and the bicycle was validated according to the Mexican Standards nmx-d-198-2-1985 and nmx-d-198-3-1985.

A bumper placed at the bicycle's rear mitigates injuries caused by the vehicle's impact on the cyclist and absorbs kinetic energy due to the impact. The system is also useful for changing the body's kinematics. The head hits an area closer to the windscreen center due to the same principle of deformation energy density, being less rigid, reducing the possible severity of craniocerebral injuries. It can be seen that the rate of craniocerebral injury for the scenario with the passive safety device installed on the bicycle is considerably lower, which influences the probability and severity of the injury, going from being incompatible with survival to having a chance of survival. However, with critical and non-reversible injuries, a skull fracture is presented, with a loss of consciousness for more than 24 hours, and intracranial hemorrhage occurs. In the case of the thorax injuries, the two cases' probabilities are similar since it is estimated that there will be a fracture of multiple ribs in both cases. Likewise, there is a 43.22% and 57.77% probability in cases A.1 and B.1, respectively, of complex thoracic injuries with

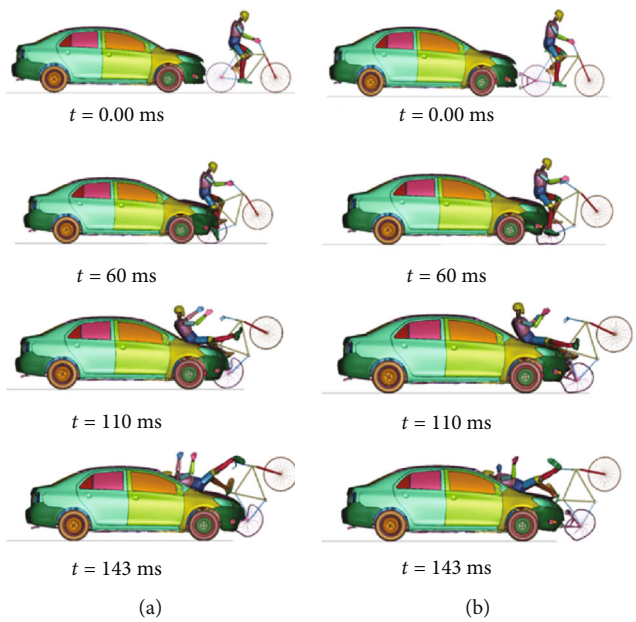

Figure 7: Impact on a cyclist on the overtaking stage at 60 km/h without a passive safety system (a) and with a passive safety system (b).

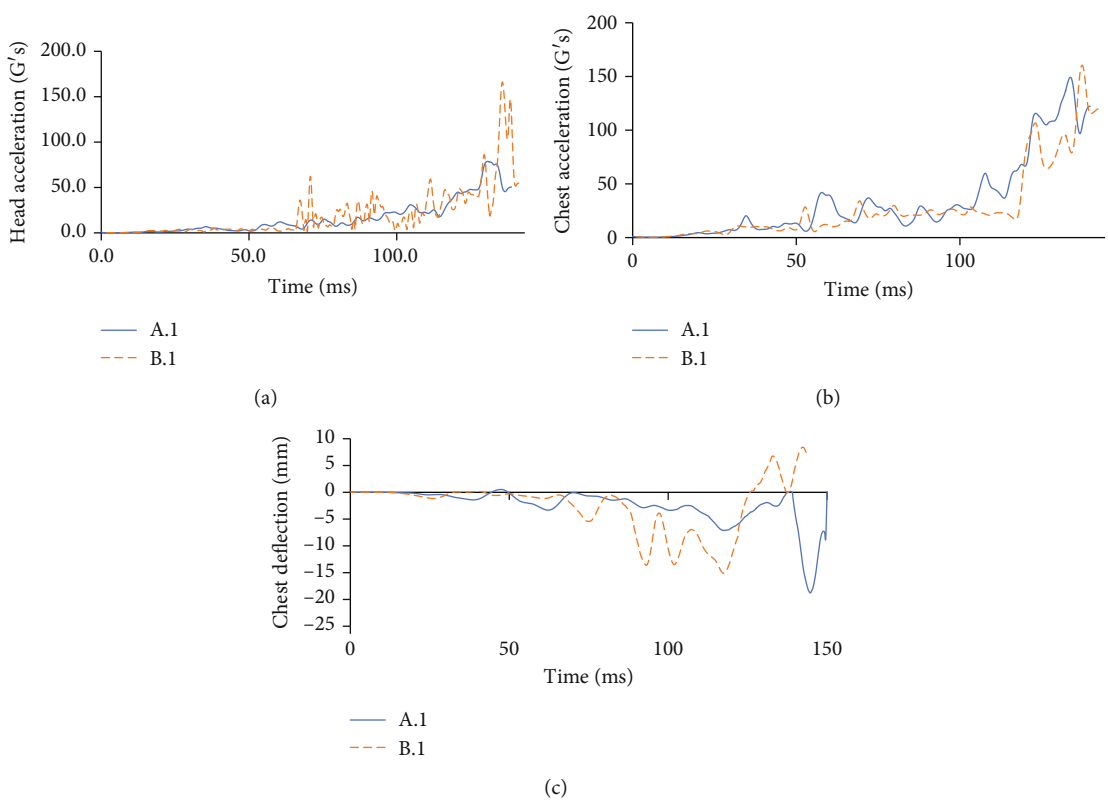

Figure 8: (a) Acceleration in the head and HIC's gravity center at a speed of 60 km/h. (b) Acceleration of chest gravity center in G's at a speed of 60 km/h. (c) Chest deflection in mm during a traffic accident at a speed of 60 km/h.

respiratory difficulty, production of massive hemothorax, and cardiac rupture or contusion, which fall into the category of critical injuries with uncertain survival. For the lower limbs, it is essential to mention that only the right limb is referred to in the tables since, due to the setup of the hit-and-run scenarios, and the left lower limb always presents injuries far below those generated in the right limb. Both hit and run cases show similar results, where there is a

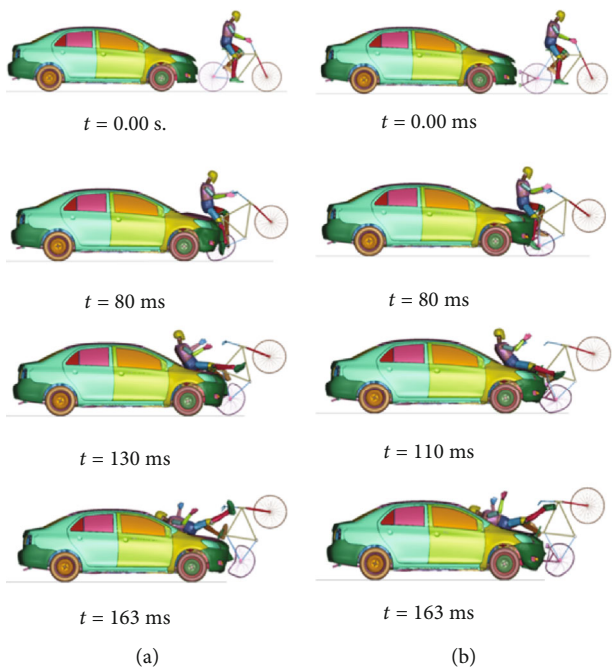

Figure 9: Cyclist overtaking impact at 50 km/h without a passive safety system (left) and with a passive safety system (right).

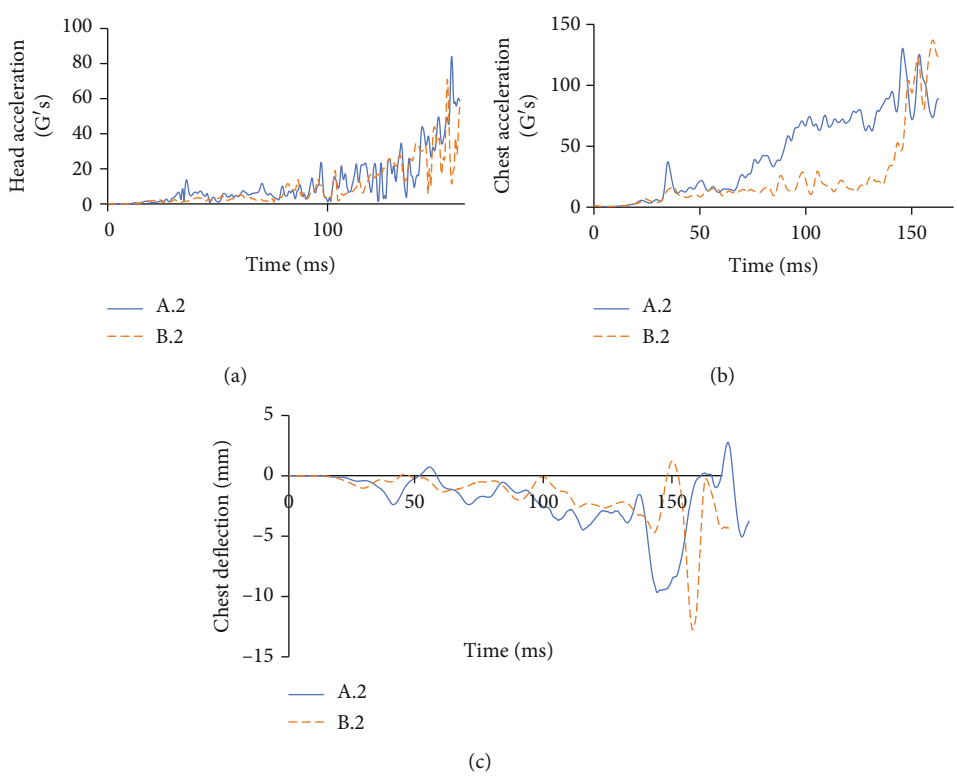

Figure 10: (a) Acceleration of head gravity center and HIC at a speed of 50 km/h. (b) Acceleration of chest gravity center in G's at a speed of 50 km/h. (c) Chest deflection in mm during the accident at a speed of 50 km/h.

probability of less than 50% of presenting a nondisplaced fracture of the femur, an injury categorized as moderate on the AIS scale. In comparison, the probability of presenting an exposed fracture of this bone is less than 20% in both cases, although this probability is lower when the bicycle has a passive safety device installed. There are injuries to the cyclist's right tibia; injuries, show an AIS = 2 level injury will undoubtedly occur, indicating a fracture of this bone due to the impact.

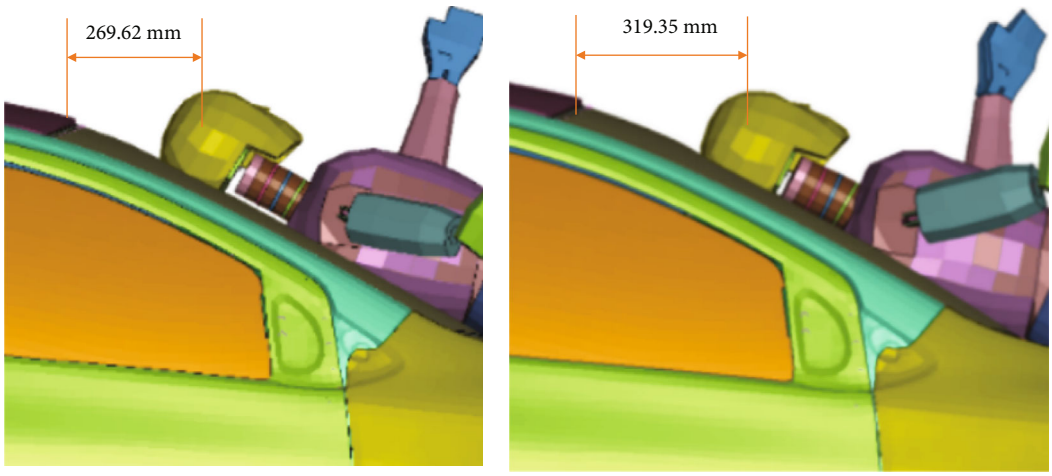

(a) (b)

Figure 11: Cyclist's head windshield contact at the vehicle. (a) No passive safety device (b) with a passive safety device.

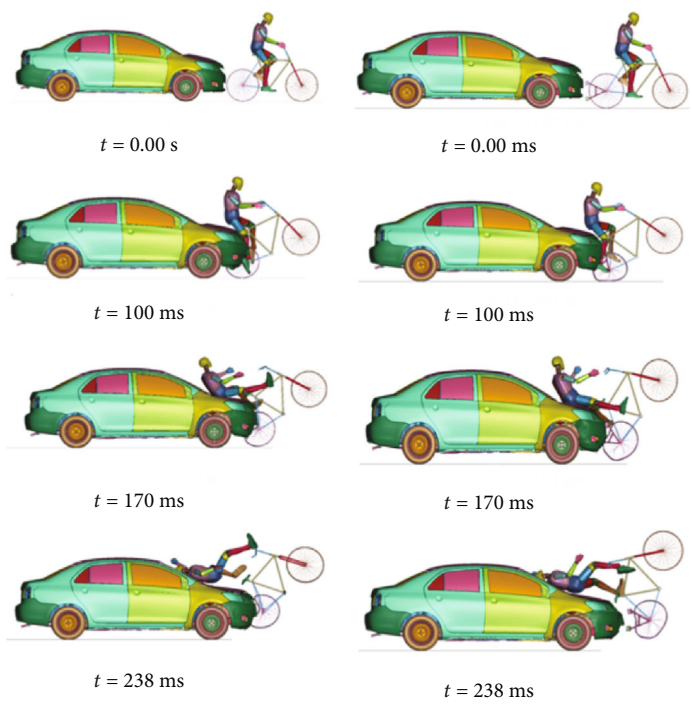

(a) (b)

Figure 12: Cyclist overtaking impact at 40 km/h without a passive safety system (a) and passive safety system (b).

The results show the craniocerebral injury rate for the scenario with the passive safety device fitted to the bicycle is again considerably lower, classified on the AIS-4, which is severe, but with probable survival, where cranioencephalic trauma with or without fractures may occur, accompanied by unconsciousness and neurological signs such as posttraumatic amnesia for 3-12 hours. On the other hand, the most likely injuries when the bicycle does not have a passive safety device are categorized at AIS = 5 level, critical injuries where survival is uncertain. In the case of injuries to the thorax, the probabilities between the two cases are again similar, since it is estimated that in both cases, there will be a fracture of multiple ribs, with a probability of practically 100% of presenting an AIS = 3 level injury; likewise, there is a 13.23% and 21.54% probability in cases A.2 and B.3, respectively, with a 13.23% and 21.54% probability of presenting an AIS = 3 level injury, respectively. Moreover, case B.3, respectively, has a 13.23% and 21.54% probability of AIS = 5 thoracic injuries, complex injuries with respiratory difficulty, production of massive hemothorax, and cardiac rupture or contusion, which fall into the category of critical injuries with uncertain survival [29, 30]. For the lower limbs, in this case,

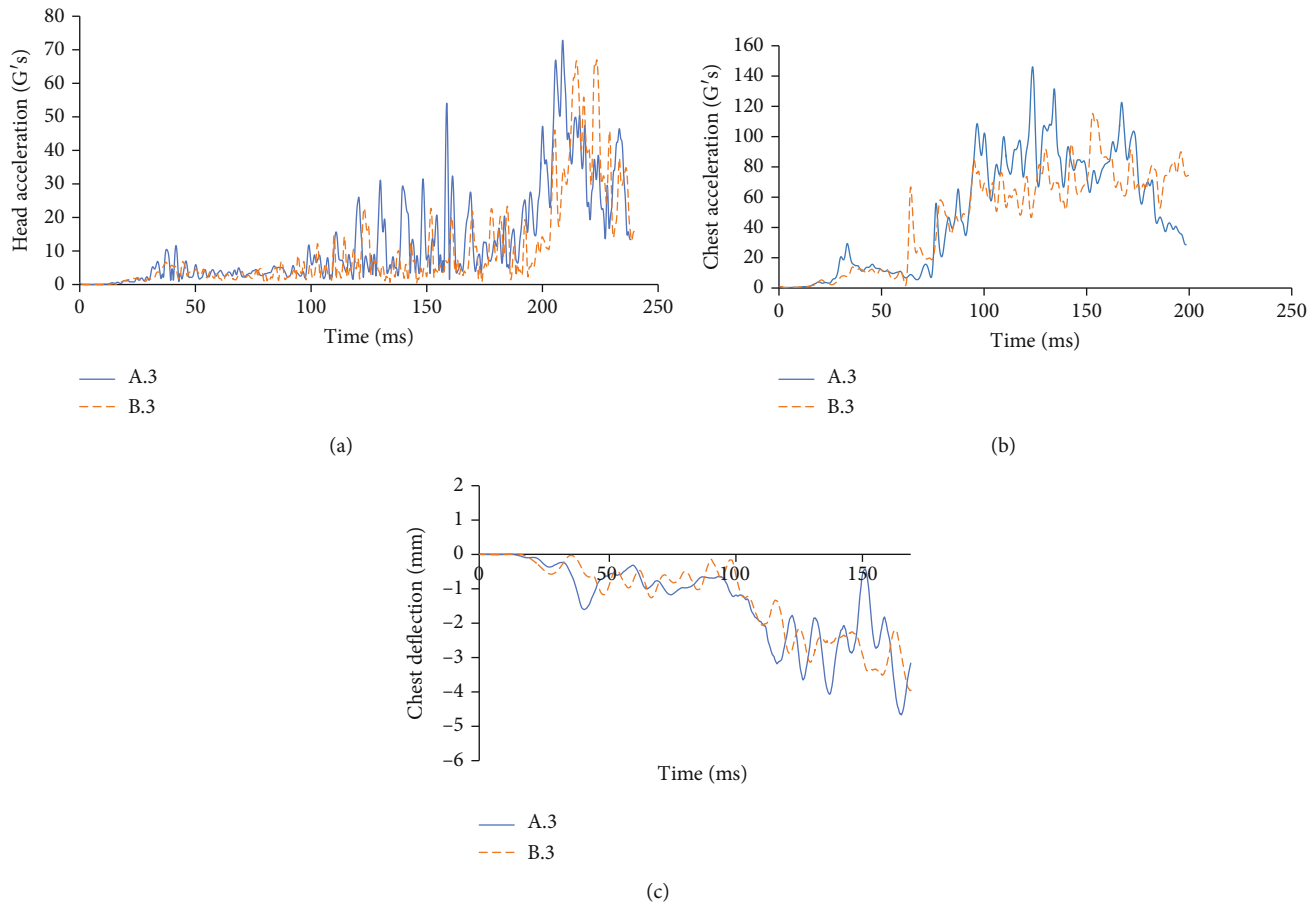

Figure 13: (a) Head acceleration in the center of gravity and HIC at a speed of 40 km/h. (b) Chest acceleration in G's at a speed of 40 km/h. (c) Chest deflection in mm during the accident at a speed of 40 km/h.

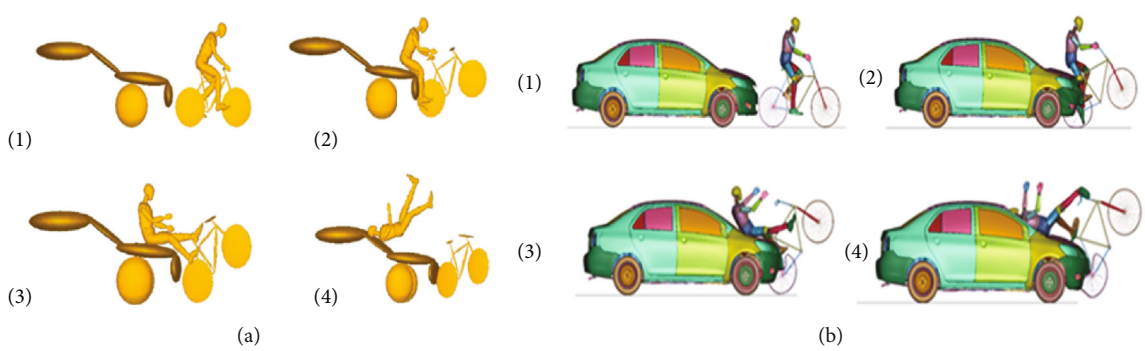

Figure 14: Cyclist's kinematics during an overtaking crash. (a) MADYMO run-over simulation; (b) FEM simulation.

there is a considerable difference in the probability of injury to the cyclist's right femur, since in the case where the bicycle does not have the safety device installed, the probability of suffering a nondisplaced fracture is 8.18%.

In comparison, if the device is installed, the probability increases to 28.4%. In presenting an exposed fracture in this bone, the probability remains less than 20% in both cases, although it is higher when the bicycle has a passive safety device installed. The cyclist's right tibia shows an AIS = 2, which indicates the fracture of this bone due to the impact.

The results the tables have shown are again considerably lower, which influences the likelihood and severity of the injury, being categorized on the AIS scale as level 3 injuries that are serious but not life-threatening and are fully reversible, although hospitalization is necessary. On the other hand, the most likely injuries when the bicycle is not fitted with the passive safety device are categorized at AIS level 4, severe, life-threatening injuries, but with probable survival. In the case of injuries to the thorax, the probabilities between the two cases show a more significant variation than in the

previous cases, since the probability of suffering an ASI = 3 or greater injury for the case where the bicycle does not have the passive safety device installed is very close to 100% (97.79). In contrast, if the bicycle does have this device installed, the probability decreases to 80.77%. The same pattern is observed in the probability of suffering injuries ASI = 5 or greater, where case A.3 has 24.09%, while case B.1 has 4.48%. For the lower limbs, specifically the cyclist's right femur, the results between both cases are again quite similar, approaching the null probability of injury to the femur, whether AIS = 2 or AIS = 3, with a variation of no more than 2% between the results and a percentage of injury of less than 5%. In the case of cyclist's right tibia, the results again show that an AIS = 2 level injury will occur, which indicates the fracture of this bone injury is a consequence of the impact since the percentage of presenting this injury remains at the same value as the previous cases with a 100% probability of fracture.

For the cranioencephalic injuries generated in the accident, in all cases where the passive safety device was used, the HIC index decreased considerably, reducing the severity of the injuries by one level according to the AIS scale. However, the impact of this is not minor, as it has several implications.

(1) In cases where a cyclist is hit at a speed of 60 km/h, the device's use can reduce the likelihood of injury to such a degree that survival is possible, which is not the case where the device is not fitted

(2) For the 50 km/h cases, the use of the device can reduce the probability of injury, compared to the results obtained for the run-over cases where the device is not installed, so that the expected injuries correspond to the ASI = 4 level, where survival is likely, as opposed to the AIS = 5 level, where the injuries generated are critical

(3) In a collision at a speed of 40 km/h, the injuries generated on the cyclist, when using the passive safety device, are reduced to an AIS = 3 level, where the cyclist's life is not at risk, although the injuries are categorized as severe, whereas without the device, the injuries grow to an AIS = 4 level, where the person is likely to die

The first limitation of this work is the dummy model used. A pedestrian dummy for the collision model was mounted on the bicycle and then used to report the injuries as a vulnerable road user. For this reason, it is important to corroborate the results with a specific case of the study by means of MADYMO® models. Another limitation of this work is the possibility of using THUMS® anthropomorphic dummies to determine the state of stress and deformation of soft tissue and hard tissue. Finally, the most critical limitation is the lack of other experimental dummies to report similar injuries on vulnerable road users. It is then essential to carry out studies with shielding equipment such as helmets and lower limb protectors to corroborate the presented results. An important aspect worth mentioning in this study is the change in the severity of the injury due to the use of bicycle helmets during vehicular accidents. The characteristics and operation of a bicycle helmet do not significantly impact the cyclist's kinematics during the accident until the cyclist's head comes into contact with the car [31, 32].

5. Conclusions

The passive safety device significantly reduced the severity of craniocerebral injuries by decreasing the magnitude of the HIC index by 775, 228, and 478 points for impact speeds of 60 km/h, 50 km/h, and 40 km/h, respectively. The passive safety device's use did not significantly reduce the severity of thoracic injuries at high speeds (60 km/h and 50 km/h); however, it did reduce them at low speeds (40 km/h) by obtaining a 19.61% less of the probability of suffering an injury, presenting an AIS ≥ 5 injury when using the device. The forces applied to the cyclist's femur indicated a 28.4% greater variation in the probability of sustaining an AIS ≥ 2 injury when using the passive safety device. In conclusion, the design fulfilled its primary function by reducing the severity of cranioencephalic injuries to one level in the AIS system in all cases, which implies the significant decrease in risk of death by cranioencephalic trauma, especially at low-speed cases in this particular run-over scenario, because this type of injury is the one with the highest risk of mortality for cyclists.

Data Availability

The data used to support the findings of this study are available from the corresponding author upon request.

Conflicts of Interest

The authors declare that there is no conflict of interest regarding the publication of this paper.

Acknowledgments

The authors acknowledge the financial support for the realization of this work of the Mexico Government by Consejo Nacional de Ciencia y Tecnología (CONACyT) and the Instituto Politécnico Nacional (IPN). The authors also thank the support of project 20210282 and EDI grant, all by SIP/IPN.

References

[1] WHO, "OMS|10 datos sobre la seguridad vial en el mundo," November 2018, http://www.who.int/features/factfiles/roadsafety/es/.

[2] M. Peden, "Informe mundial sobre prevención de los traumatismos causados por el tránsito Informe mundial sobre prevención de los traumatismos," in *Informe mundial sobre prevención de los traumatismo*, pp. 16–95, Pan American Health Organization, 2004.

[3] "Administración Pública del distrito Federal, Reglamento de Tránsito del Distrito Federal," 2015, http://www.data.obras

.cdmx.gob.mx/wp-content/themes/obrastheme/htmlimages/normatividad/ReglamentoTransitoDF.pdf.

[4] National Highway Traffic Safety Administration, *2017 Data: Bicyclists and Other Cyclists*, Washington, DC, USA, 2019.

[5] Instituto Nacional de Estadística y Geografía, "Consulta interactiva de datos," October 2019, https://www.inegi.org.mx/sistemas/olap/proyectos/bd/continuas/transporte/accidentes.asp?.

[6] D. L. Harkey, S. Tsai, L. Thomas, and W. W. Hunter, "Pedestrian and Bicycle Crash Analysis Tool (PBCAT): Version 2.0 Application Manual," Federal Highway Administration, Washington, DC, USA, 2006.

[7] L. Raslavicius, L. Bazaras, A. Keršys, V. Lukoševicius, R. Makaras, and V. Eidukynas, "Assessment of bicycle-car accidents under four different types of collision," *Proceedings of the Institution of Mechanical Engineers, Part H: Journal of Engineering in Medicine*, vol. 231, no. 3, pp. 222–234, 2017.

[8] M. Van Schijndel, S. De Hair, C. Rodarius, and R. Fredriksson, "Cyclist kinematics in car impacts reconstructed in simulations and full scale testing with polar dummy," in *2012 IRCOBI Conference Proceedings - International Research Council on the Biomechanics of Injury*, pp. 800–812, Dublin, Ireland, 2012.

[9] A. MacAlister and D. S. Zuby, "Cyclist crash scenarios and factors relevant to the design of cyclist detection systems," in *2015 IRCOBI Conference Proceedings - International Research Council on the Biomechanics of Injury*, pp. 373–384, Lyon, France, 2015.

[10] National Highway Traffic Safety Administration, 2018, 2016 Data: Bicyclists and Other Cyclists.

[11] National Highway Traffic Safety Administration, 2015, 2015 Data: Bicyclists and Other Cyclists.

[12] C. Tan, *Crash-Type Manual for Bicyclists*, University of North Carolina Highway Safety Research Center, Washington, DC, USA, 2016.

[13] Sanheshun Industry And Trade Co Ltd, "Child bicycle bumper with anti-collision function," 2013, US Patent CN203581225U.

[14] A. Montenare, "Pneumatic cycle bumper," 1993, US Patent US3975042A.

[15] Honda Motor Co Ltd, "Vehicle having shock relaxing device, and vehicle having bumper," 2006, US Patent JP2007269271A.

[16] L. Yong, "Novel motorcycle bumper device," 2012, US Patent CN103895758A.

[17] W. Huff, N. C. Asheville, and C. Huff, "BICYCLE GUARD," 1940, US Patent US2194660A.

[18] B. Loibl, "Bicycle bumper with a light generating a bike lane," 2018, US20080219014A1.

[19] I. L. Cruz-Jaramillo, C. R. Torres-San-Miguel, O. Cortes-Vasquez, and L. Martinez-Saez, "Numerical low-back booster analysis on a 6-year-old infant during a frontal crash test," *Applied Bionics and Biomechanics*, vol. 2018, Article ID 235926, 6 pages, 2018.

[20] D. Marzougui, R. R. Samaha, C. Cui, and Y. K. S. Opiela, "Extended validation of the finite element model for the 2010 toyota yaris passenger sedan," *The National Crash Analysis Center (NCAC)*, vol. 2012-W-005, pp. 12–15, 2012.

[21] M. Fritz, T. Wimmer, and S. van Montfort, "CATS/4a CATS D3.4 Bicyclist Target Specifications," in *TNO - innovation for life, Identifier 564756*, pp. 5–8, Helmond, Netherlands, 2016.

[22] Dirección General De Normas, Nmx-d-198/2-1985, "autotransporte - bicicletas – especificaciones," 1985, https://docplayer.es/85390565-Nmx-d-198-autotransporte-bicicletas-metodos-de-prueba-autotransport-bicycles-test-methods.html.

[23] Comité Europeo de Normalización, "Bicicletas de montaña Requisitos de seguridad y métodos de ensayo," *Diario Oficial de la Unión Europea L 200/35*, vol. 14766, p. 117, 2005.

[24] W. W. Feng and J. O. Hallquist, "On Mooney-Rivlin Constants for Elastomers," *Stress*, vol. 1, 2012.

[25] C. K. Simms and D. Wood, "Pedestrian and cyclist impact," in *A biomechanical perspective*, Springer, 2009.

[26] V. Kanyanta and A. Ivankovic, "Mechanical characterisation of polyurethane elastomer for biomedical applications," *Journal of the Mechanical Behavior of Biomedical Materials*, vol. 3, no. 1, pp. 51–62, 2010.

[27] M. Kleinberger, E. Sun, R. Eppinger, S. Kuppa, and R. Saul, "Development of Improved Injury Criteria for the Assessment of Advanced Automotive Restraint Systems," *NHTSA Docket*, vol. 440, 1998.

[28] G. Prati, L. Pietrantoni, and F. Fraboni, "Using data mining techniques to predict the severity of bicycle crashes," *Accident Analysis and Prevention*, vol. 101, pp. 44–54, 2017.

[29] O. Ramirez, M. Ceccarelli, M. Russo, C. R. Torres-San-Miguel, and G. Urriolagoitia-Calderon, "Experimental dynamic tests of RIB implants," *Mechanisms and Machine Science*, vol. 68, pp. 353–361, 2019.

[30] O. Ramirez, C. R. Torres-San-Miguel, and M. Ceccarelli, "Urriolagoitia-Calderon G Experimental characterization of an osteosynthesis implant," *Mechanisms and Machine Science*, vol. 73, 2019.

[31] M. R. Begley and F. W. Zok, "Optimal material properties for mitigating brain injury during head impact," *Journal of Applied Mechanics*, vol. 81, 2014.

[32] P. A. Cripton, D. M. Dressler, C. A. Stuart, C. R. Dennison, and D. Richards, "Bicycle helmets are highly effective at preventing head injury during head impact: head-form accelerations and injury criteria for helmeted and unhelmeted impacts," *Accident Analysis and Prevention*, vol. 70, pp. 1–7, 2014.

Hindawi
Applied Bionics and Biomechanics
Volume 2021, Article ID 5555218, 14 pages
https://doi.org/10.1155/2021/5555218

Research Article

Aortic Blunt Trauma Analysis during a Frontal Impact

Mario Alberto Grave-Capistrán, Arturo Yishai Prieto-Vázquez, and Christopher René Torres-SanMiguel

Instituto Politécnico Nacional, Escuela Superior de Ingeniería Mecánica y Eléctrica, Sección de Estudios de Posgrado e Investigación Unidad Zacatenco, 07738, Mexico

Correspondence should be addressed to Christopher René Torres-SanMiguel; ctorress@ipn.mx

Received 19 March 2021; Revised 1 June 2021; Accepted 2 July 2021; Published 20 July 2021

Academic Editor: Marco Parente

The aorta is the largest artery of the human body, and it is considered in the continuous medium mechanics as a hyperelastic material for its biological properties. The thoracic aorta is directly affected in vehicular collision events by compression generated between the ribcage and the three-point seatbelt tension producing injuries in the artery wall. A three-dimensional model of the thoracic aorta was constructed from digital tomographic images considering the ascending aorta, the aortic arch, and the descending aorta. The model obtained presents acceptable characteristics such as a length of 222.8 mm and an ascending aortic diameter of 22.7 mm, 22.7 mm in the aortic arch, and 16.09 mm in the descending aorta. A 150 ms time numerical simulation was developed through the finite element method (MEF), and the model was analyzed simulating a compression load on the artery at its front location. Boundary conditions were considered by selecting specific nodes in the model, such as the points where the artery is held in the thorax with other elements. In addition, displacement nodes were considered to establish a natural behavior of the artery. The outcomes show significant displacements in the artery wall. The most affected areas are the aortic arch and descending aorta, whose displacements reach 14 mm from their original position. Based on the abbreviated injury scale (AIS), the degree of injury to the aorta in this collision event is estimated, an AIS 2 with a moderate severity index and required medical attention.

1. Introduction

Traffic accidents are considered scenarios in which the human body can suffer several traumas. Three-point retention systems prevent the head and thorax from impacting the dash and steering wheel, causing injuries on the rib cage due to the compression effect between the seat belt and thorax. The aorta is one of the affected arteries structurally, harming the aortic wall. Aortic trauma is a life-threatening event characterized by fatal injuries such as lacerations and tears in the aorta. Blunt trauma spontaneously interrupts the circulation of the human body blood flow to the vital organs, affecting the victim's life. The worst situation causes immediate death, and traffic accidents are the leading cause of this trauma. Compression injuries to the thoracic aorta are generally in the aortic arch and descending aorta. Forceful cardiac rupture occurs more frequently in traffic accident events (73%), and cardiac injury has a mortality rate of 89%. 98% of the victims involved in car accidents with aortic injuries are classified in AIS3, and most of them died at the scene accident. The literature reports that the aortic arch suffers a critical injury, and 95% of victims with an aortic rupture undergo immediate surgical intervention survive [1–4]. Statistics about injuries on the chest in crash scenarios have been made by analyzing the most common injuries by wearing a seat belt. Percentages were established for a fatal aortic injury; the United Kingdom with 98.10% and the United States of America with 91% in frontal car collisions using a seatbelt. Although the seat belt reduces the risk of traumatic injuries in the body, there is a possibility of blunt trauma in the organs after a high impact which transfers energy directly to the thorax affecting the thoracic aorta. The study indicates a high percentage of aortic injuries using the seatbelt in a frontal collision. Although the airbag is activated, chest

injuries are still serious to the internal organs. The traumatic injuries occur in the arms and pelvic area, and bruises are also generated through the chest and abdomen. The arteriograms confirm that there are traumatic injuries in the thoracic aorta, mainly in the descending aorta, it was determined that the harm was caused by the compression of the two-point or three-point seat belt, associating them with the "seatbelt syndrome" [5, 6]. Studies have been carried out on thoracic trauma and aortic rupture in frontal collision traffic accidents. The energy required to compress a soft tissue is proportional to the stress applied and material deflection. It has been established that the organs are described as viscous material characteristics, and the compressive force is proportional to the impact speed. In a certain amount of energy, when the impact speed rises, the consequence is that chest compression tolerance decreases. It has been confirmed by experimental evaluations of the theories about frontal and lateral impacts in high-speed events (more than 33 km/hr). In addition, high-speed situations produced injuries in the thoracic internal organs which are critical, particularly heart ruptures such as the thoracic aorta and large vessels of the circulatory system [7]. The aorta has been evaluated in its parts (ascending aorta, aortic arch, and descending aorta) considering that there is a joint to the thoracic spine, the heart, and the supra-aortic trunks, and it is estimated that the causes of the rupture of the artery are a sudden displacement of blood flow towards the aortic isthmus (hammer blood), a compression of the bony artery structure of the rib cage with the thoracic spine, and the effect of tension-torsion due to a sudden deceleration [8].

On the other hand, numerical simulations have been developed involving the behavior of the thoracic aorta when it is subjected to compression loads, simulating both lateral and frontal vehicular collision events. Demiray and Holzapfel developed numerical simulations applying mathematical tensors to represent the aorta mechanical properties. Boundary conditions are considered in specific parts of the artery (the aortic arch, supra-aortic trunks, and descending aorta). Tension in the artery is generated, severely injuring the ascending aorta [9]. The Wayne State Human Body Model (WSHBM) is a computational tool that integrates somebody's region such as the shoulders, ribs, and thorax, and it has been found that the maximum principal stresses after applying stress to the aorta are between 102 kPa and 136 kPa [10]. With LS-DYNA software, the aorta was considered as a transversely isotropic element of an incomprehensible hyperelastic material. It has been found that in a left lateral collision at a speed of 27.6 km h-1 in a time of 90 ms, the Von Mises stress peak is 1.8 MPa [11]. The following mechanical properties were assigned considering the aorta as an elastic material: density of 1.20 E-06, Young's modulus of 5.00 E-03, and Poisson's ratio of 0.40. Results reveal that the descending aorta presents a maximum peak value of 0.148 kPa. On the other hand, the maximum value obtained for the aortic bulb was 0.263 kPa, and the maximum value of stress was 55.4 kPa.

These values are interpreted as serious in specific artery areas such as the aortic arch [12]. The methodology for the three-dimensional modeling of parts of the human body is considered important; studies on compression loads with an average acceleration of 6.51 in the human thorax were performed, and it has been found that a compression load of 5.16 N generates a deflection in the rib cage of the human body causing injuries to internal organs. The rib cage is one area in the human body that suffers injuries due to car accidents or high-energy traumas. Studies report that injuries to the thorax can be fatal in a car accident. Studies conducted on the chest's behavior in different load scenarios show that the energy generated by the automotive impact is transmitted to the organs inside the rib cage. Analyses were performed on lesions in the thorax using a six-year-old Hybrid III finite element model. Applying standards based on the evaluation of rollover car crashes; it was recorded that the thorax of the human body gets more damage when a seat belt 3 points is used, and the deflection in the chest reaches up to 6.21 mm. Applying the Chest Severity Index using a finite element model Hybrid III dummy type in a frontal car collision, lesions in the thorax with a high degree of mortality are reported. Numerical simulations of 120 ms period time have been created, and the lesions in the thorax have been analyzed in frontal crash tests, boundary conditions are considered and are automatically assigned by the software, passive safety elements such as the seat belt generates compression loads that cause injuries to the rib cage [13–16]. Finally, a viscoelastic fractional model applying MEF has been used to create numerical simulations dividing the artery wall into its 3 layers: the intima, the media, and the adventitia. The layer's behavior determines the distribution of stresses and the deformation in the artery under the Von Mises criteria [17].

This research is aimed at analyzing the structural behavior of the aorta by a numerical simulation in different compression steps due to frontal crashes. Furthermore, the results focus on establishing a relationship with the type of injury and structural damage working as a predicting damage method of the thoracic artery. In addition, the present study goes further than the available literature on the aortic wall analysis through the construction of a numerical simulation based on programmable control instructions solved by specialized mathematical language and using the FEM applied to three-dimensional modeling obtained from TC. Thus, results show a perspective of the structural behavior of the aorta in different compression steps due to frontal impacts in a car, highlighting substantial displacements in the artery wall.

2. Materials and Methods

Following the proposed methodology presented in Figure 1, a detailed model was developed with the literature's characteristics and will allow it to be subjected to numerical simulations applying FEM. The thoracic aorta's three-dimensional model began by identifying the parts and the specific location within the human body. The research was carried out based on clinical and biological reports. A computer program that allows artery reconstruction was also selected to develop a three-dimensional model. The parts were evaluated from a

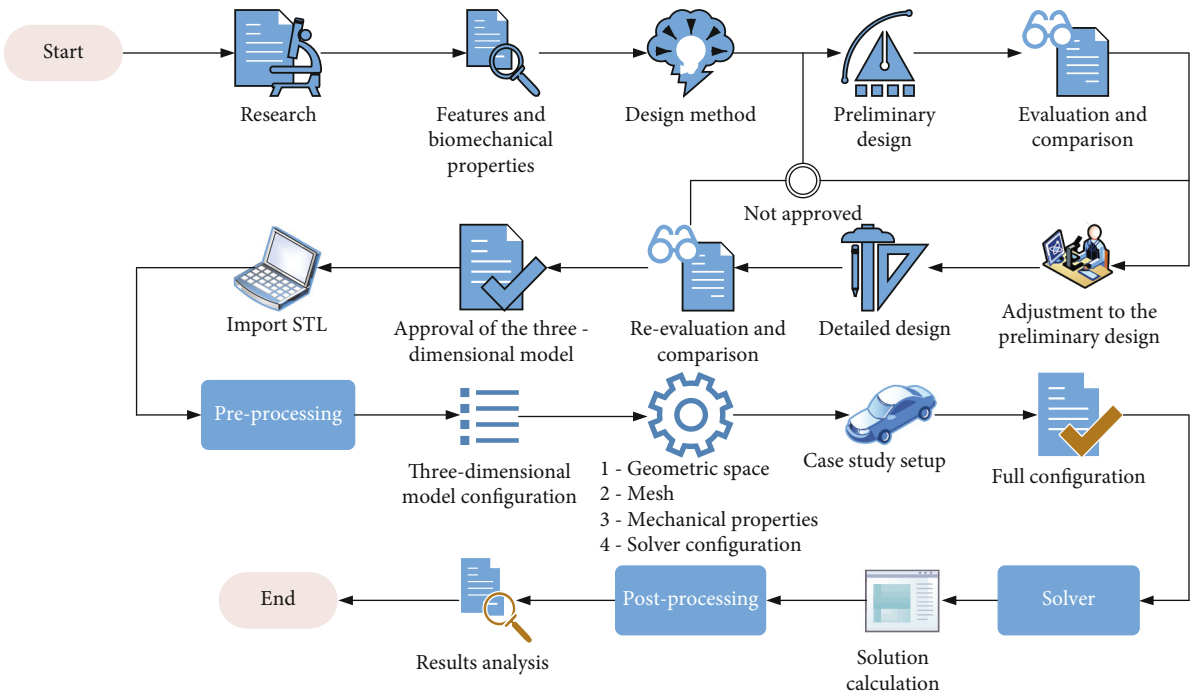

Figure 1: Flow diagram for the three-dimensional modeling of the aorta.

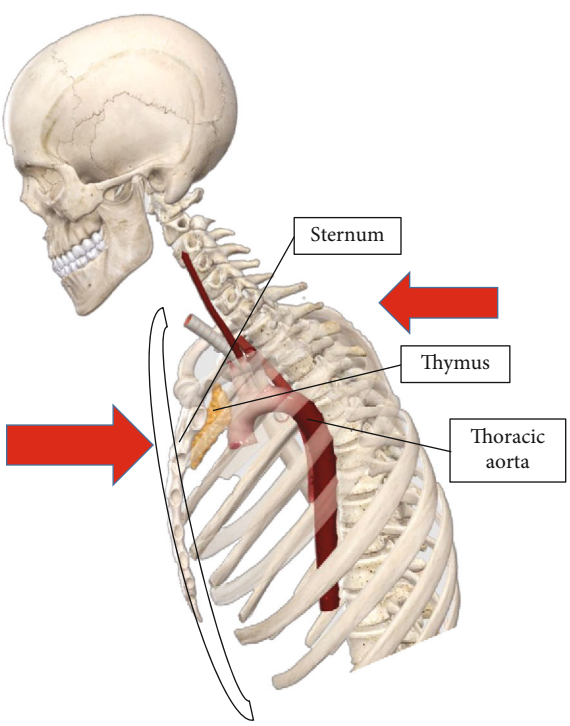

Figure 2: Thoracic injuries by seat belt compression.

preliminary model with the characteristics to be subjected to numerical analysis.

Based on the literature on the artery's biomechanics and the clinical reports collected for this research, it is determined that the aorta receives compression stress from the tension generated by the three fastening points that the seatbelt integrates into a car. The inertial force of the frontal impact forces the human body to move forward with an inclination towards the car's steering wheel. The seat belt is activated, retaining the human body avoiding an impact with the dashboard, awning, or steering wheel. From this event, the compression stress is generated towards the thorax, initially affecting the bone structure of the rib cage and, in particular, the sternum, the stress transmission towards the internal organs of the human body, such as the thymus and the aorta. Figure 2 represents the frontal collision event and the parts of the human body affected by the retention of the seat belt (sternum, thymus, and aorta).

2.1. Three-Dimensional Modeling of the Aorta. The three-dimensional modeling of the thoracic aorta was developed through the SCANIP® computer program. First, the artery was reconstructed from a sequence of 222 digital images belonging to the thorax of the human body of a 50th percentile Mexican patient. The best way to obtain a three-dimensional model is through computed tomography (CT). Therefore, these digital images were configured as a complete data range in order to obtain the best resolution in each image. In addition, a mask was configured to identify the parts of the thoracic aorta, and through the work interface of the computer program divided into the three cross-sections it uses (horizontal, sagittal, and frontal), the three-dimensional model reconstruction of the thoracic aorta contemplates the geometry based on clinical reports.

The reconstruction process identifies the specific areas of the thorax in which the thoracic aorta is located. The mask created has the purpose of indicating the parts of interest of the model to be generated (ascending aorta, aortic arch, and descending aorta). Also, the artery elements are

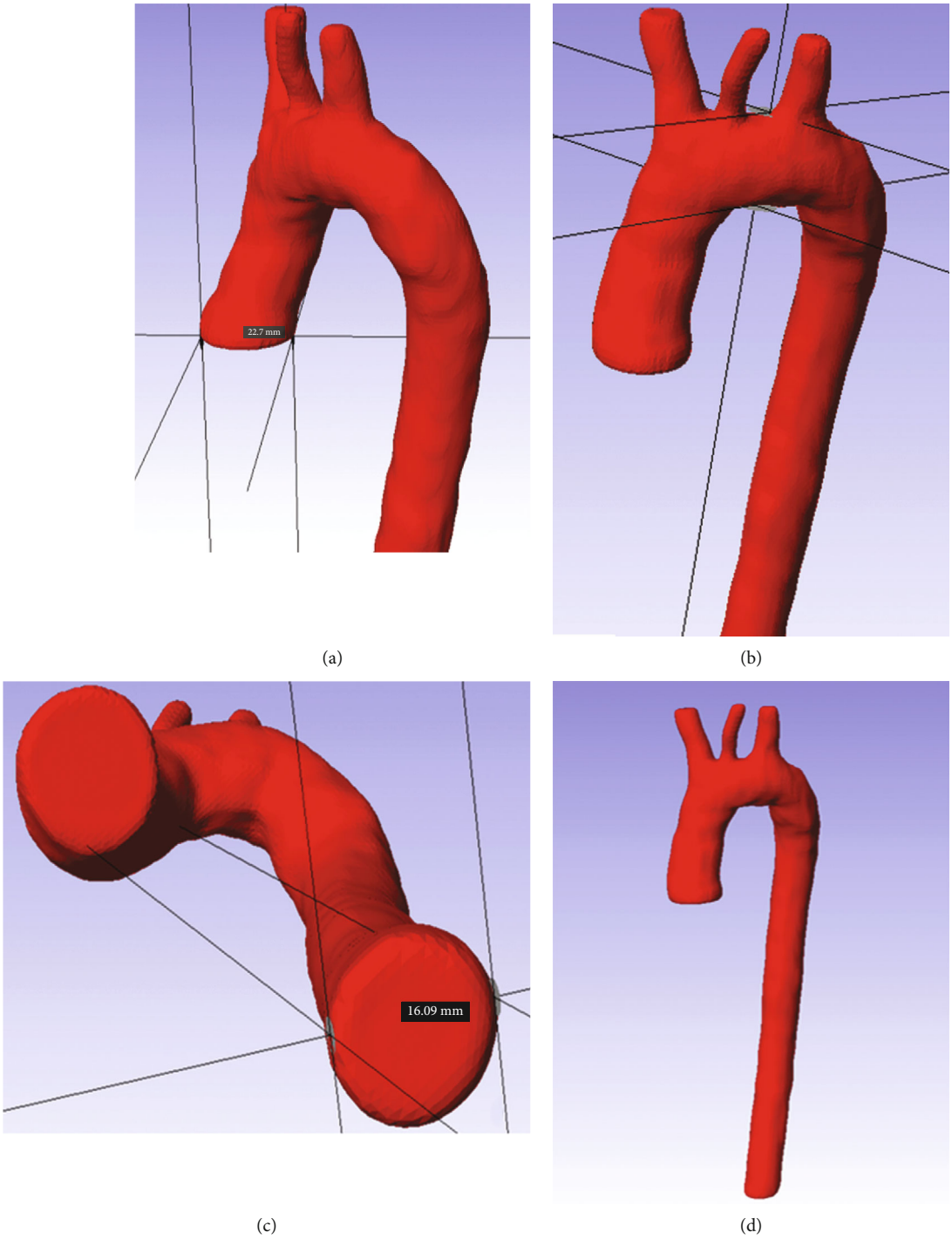

Figure 3: Aortic characteristics obtained from SCANIP®: (a) aortic bulb diameter (22.7 mm), (b) Aortic arch diameter (21.96 mm), (c) Aorta descending diameter (16.09 mm), and (d) 3D model of the aorta.

considered boundary conditions, as fixation points were considered: the aortic bulb and the supra-aortic trunks (brachiocephalic trunk, left common carotid artery, and subclavian artery). The cleaning process of the digital images was carried out by preserving the pixels that make up the thoracic aorta in each layer. The model generated in SCANIP® is a three-dimensional solid body, and a Gaussian filter was applied to erase roughness on the surface of the three-dimensional model to be used in any other computer program. Figure 3 shows the three-dimensional model of the thoracic aorta. The geometric dimensions are indicated in each of the parts of the artery.

2.2. Numerical Requirements. The Meshmixer® software provides tools to repair the 3D model obtained from SCANIP®. First, the whole model was inspected and fixed; the artery

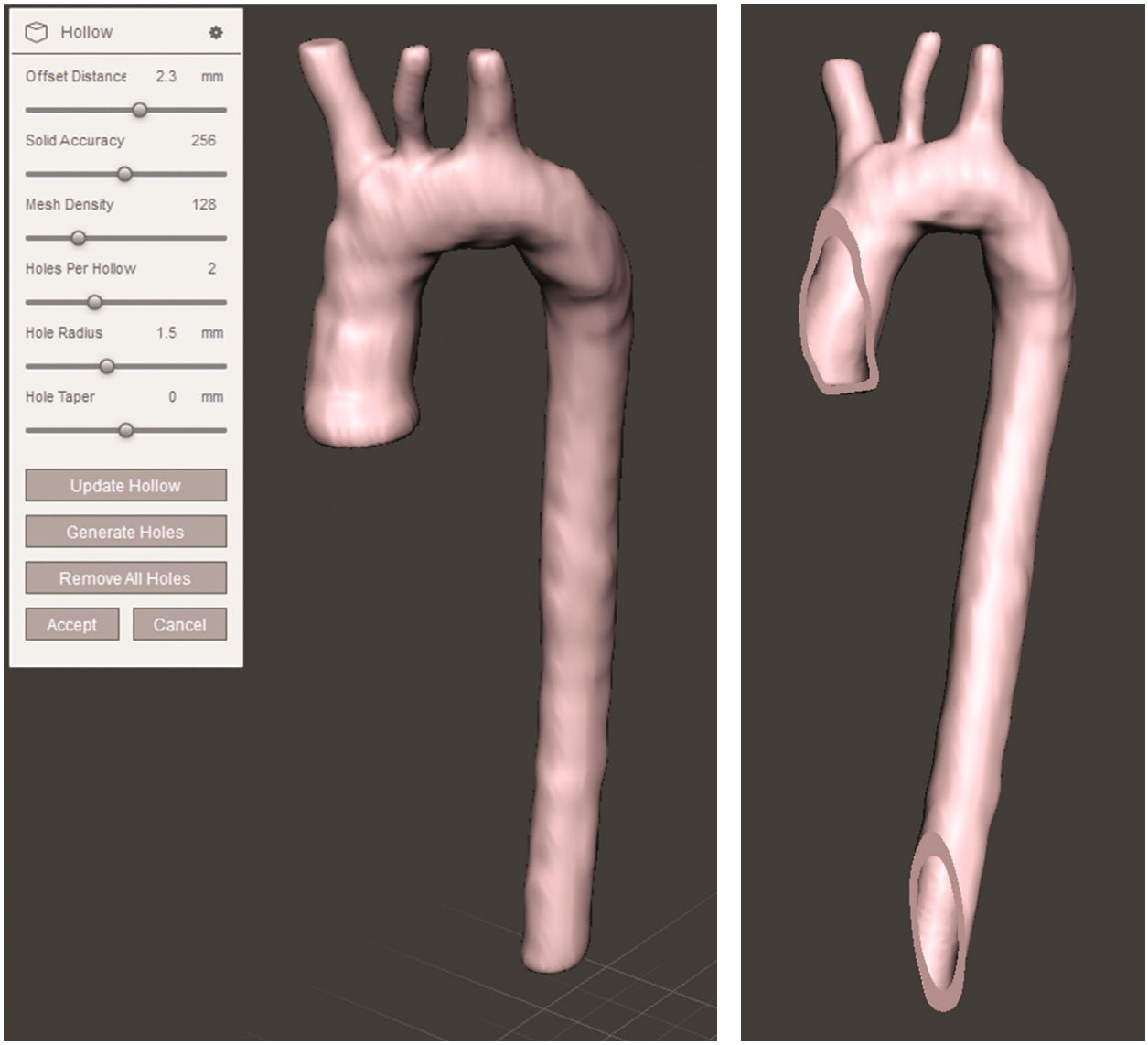

(a) (b)

Figure 4: Human aorta 3D model. (a) Thickness assignation to the model of the aorta. (b) Ascending aorta and descending aorta cuts.

wall thickness was specified based on the literature, with a tubular layer of 2.3 millimeters, and was configurated for the three parts of the aorta (ascending, aortic arch, and descending). In Figure 4 is observed a human aorta model for numerical simulation.

In Meshmixer®, it is established in the surface boundary conditions in the aortic bulb and the supra-aortic trunks. Figure 5 shows the flat faces created in the aortic arch corresponding to the ligamentum arteriosum and the anterior longitudinal ligament of the thoracic aorta located in the third vertebra and where the aorta is attached.

Once the anatomical characteristics of the aorta and the boundary conditions had been established, in a final stage, the complete model was created as a solid to avoid errors during the numerical simulation to obtain correct results. A file with STL characteristics was created to import to Matlab® software for numerical simulation.

High-energy traffic accidents in frontal collision scenarios are responsible for blunt trauma to the human body due to their impact on different parts. The purpose of using restraint systems (three-point seatbelt) is to avoid the most significant number of injuries to the passenger. However, when the impact is brutal, compression loads are generated between the thorax and the seat belt, causing injuries directly to the human aorta, producing from superficial signs such as ecchymosis in the chest to closed traumas in the aorta such as lacerations, aortic dissections, and ruptures that represent chronic complications to the victim and sometimes immediate death. The NCAP (New Car Assessment Program) is a European standard used in the automotive to evaluate motor vehicles' structural functionality and safety systems. The Latin-NCAP is the current regulation applying in Mexico. Its evaluation analyses frontal collision events against objects such as safety barriers, concrete structures, and other vehicles [18, 19].

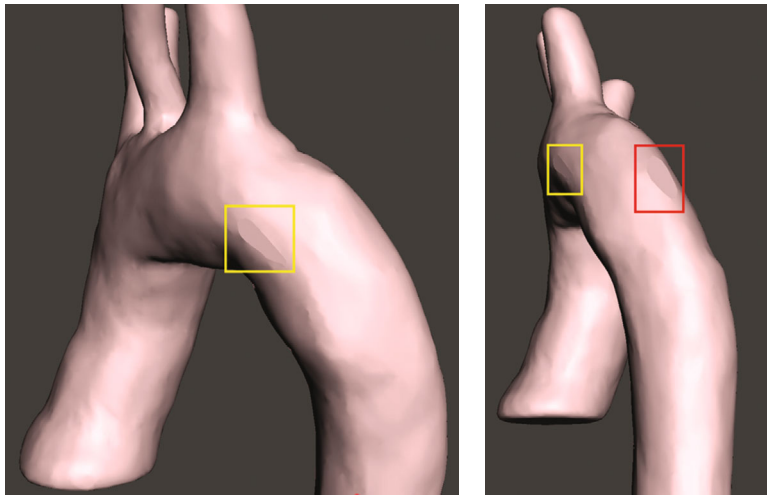

(a) (b)

Figure 5: Lateral and posterior aortic arch boundary conditions. (a) Flat face for the arterial ligament of the pulmonary artery and (b) flat face for the anterior longitudinal ligament of the thoracic spine.

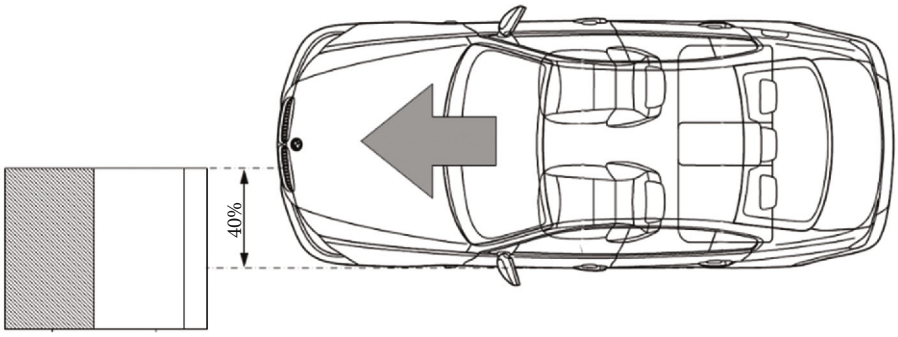

Figure 6: Frontal impact against deformable element structure from Satué-Vallvé.

For the construction of the numerical simulation, the standards and evaluation criteria of the Latin-NCAP are considered. The basic assessment configuration in safety systems proposed by the standard in frontal collision events in sedan-type cars with a mass between 1500 kg and 2000 kg is described below:

(1) The frontal impact occurs at a speed of 64 km/h (40 m/h)

(2) The vehicle hits an off-center barrier in the driver's position

(3) The front of the barrier is deformable

(4) The safety systems (3-point seatbelt, front and side airbags)

The standard considers that 40% of the frontal impacts the structure against another element in most traffic accidents. The vehicle's energy absorption is high in the impacted part (driver or front passenger), so injuries to the human body can be severe and fatal. Figure 6 represents the frontal collision event standardized by Latin-NCAP [20].

The Latin-NCAP evaluates the impacts in 150 ms, using the Abbreviated Injury Scale (AIS) to determine the injury in the human body. In most of the passengers, the chest protection is adequate during a frontal impact. However, critical injuries in internal organs such as the aorta that can be affected are not ruled out.

The numerical simulation is focused on the displacements generated in the three-dimensional model when stress compression occurs. It also contemplates the inertial action acquired by the frontal impact and the compression stress generated in the thorax by the seatbelt, which transmits payloads to the ascending aorta of the human body. The artery model is considered hyperelastic material in the geometric structure, bringing the numerical simulation to real conditions and verifying the proposal under the standards by the regulation considered. The three-dimensional model is in a vertical position, the loads are applied to the back of the 3D model (descending aorta) as an effect of the inertial movement of the frontal impact and in the frontal part (ascending aorta) due to the compression exerted by the three-point seatbelt, and Figure 7 shows the assigned forces on the "y" axis.

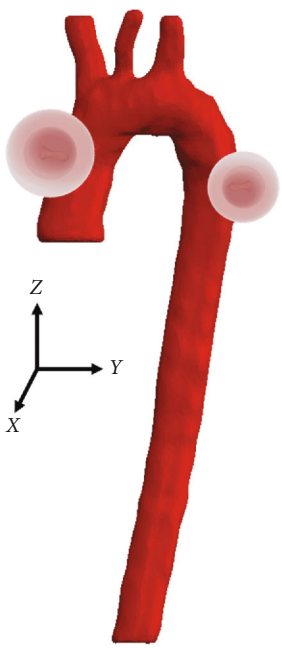

Figure 7: Forces application areas at the three-dimensional model parts.

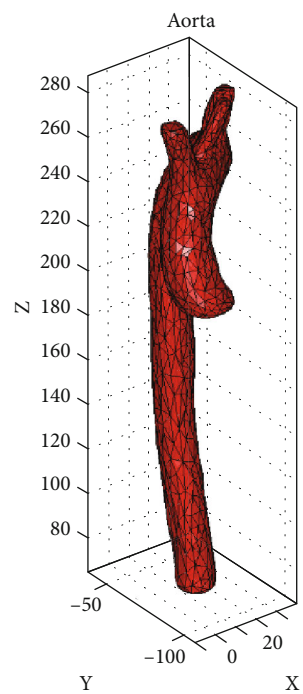

Figure 8: STL model imported to Matlab®.

Table 1: Mechanical properties of the thoracic aorta.

Mechanical properties of the arterial wall of the aorta	
Young's modulus (E)	1000 kPa
Density (ρ)	$1.2e^{-6}$ kg/mm^3
Poisson's ratio (γ)	0.45
Shear modulus (G)	137 ± 18 kPa

Mechanical properties were assigned considering the Ogden constitutive model. Table 1 shows the values for the structural configuration of the aorta model [21, 22].

2.3. Methodology for the Numerical Analysis. Matlab® software was used to import the STL, and through an open-source computer program, the preprocessing and postprocessing were structured. The STL file was load with specific commands, preserving the original model without disturbing the geometry and structure. This computer program allows the user to establish criteria on the model that allow it to be adapted to carry out numerical simulations in different circumstances. Initially, the general configuration was established through instructions based on C languages, such as font size, label location, and the three-dimensional model's visual field. Once the preliminary configuration was completed, the model was imported, instructions were established to specify the origin of the file, and finally, Matlab® shows it in the default graphical interface. Thus, the model preserves the original geometry established in the previous packages. Hence, it should be noted that the three axes' dimensions are those obtained from the 3D model built-in SCAN IP®. Figure 8 shows the 3D model of the aorta with the assigned characteristics.

Table 2: Elements for construction of the tetrahedral mesh in the 3D model of the thoracic aorta.

Mesh element	Number of elements
Points	1310
Tetrahedral	4118
Faces	9518
Faces on the outer limit	2564
Faces on the input facets	2564
Edges on input segments	3846
Steiner points within the domain	26

The numerical simulation will perform in the region for the 3D model. The generated code analyses the input elements in the imported model and transforms them into tetrahedral finite elements. The imported model contains an internal conduit that also acquires the same mesh. Table 2 shows the values of the assigned mesh to the imported 3D model.

The model is completely mapped in the finite elements selected for the structural analysis. The size of each of these tetrahedral elements is adequate concerning the computational resource required to build the numerical simulation. The finite elements created are shown in Figure 9, a close-up image, the facets of the tetrahedral elements are appreciated.

Based on the human body's anatomy and chest, specific boundary conditions are contemplated in the three-dimensional model, such as the ascending aorta, the aortic arch, and the descending aorta selected by control structures code created on the faces and nodes the model's surface. Each

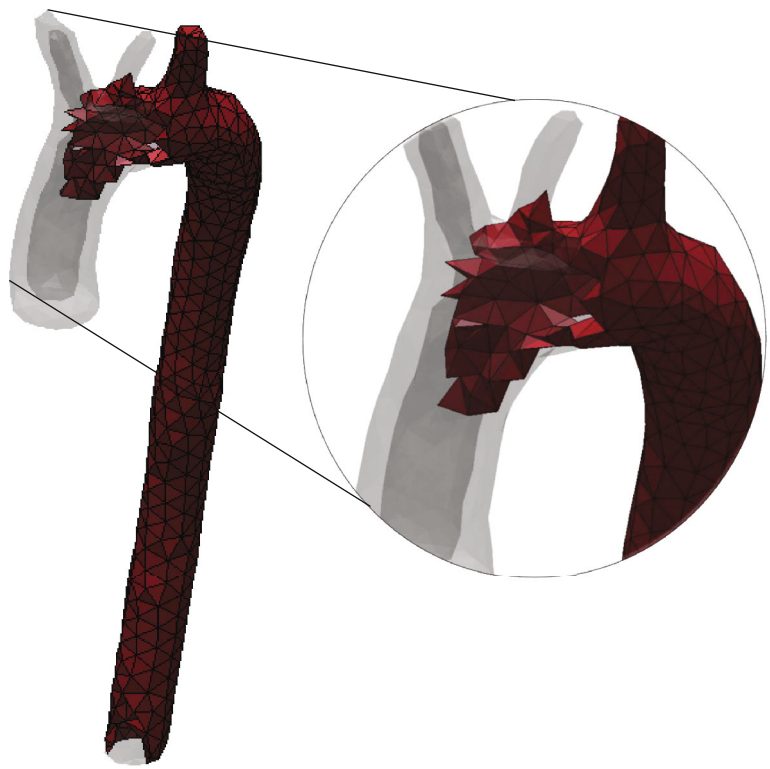

Figure 9: Three-dimensional model of the thoracic aorta in tetrahedral second-order finite elements.

node's location contains a specific value for each of the axes, including negative values that are part of the imported three-dimensional model space. Matlab® software interprets the entire model in a three-dimensional space in which each point in the model has a specific coordinate and the size of the finite element. The selection of the boundary conditions was through commands and logical operators that allowed the points and nodes' location within the three-dimensional model. In the reconstruction of the 3D model of the aorta, the final part of the aortic bulb was considered a flat face to adapt and obtain the selection of corresponding nodes. The aortic arch is the following part of the thoracic aorta; it joins the ascending aorta and the descending aorta. In addition, on the crest of the aortic arch, there are the supra-aortic trunks distributed towards the arms of the human body and the right and left frontal lobes of the brain. The boundary condition zones in the aortic arch were considered based on literature. The support nodes were attached in the same way as in the ascending aorta, and the mapping was carried out in this area and the nodes corresponding to the points considered. The aortic arch section presents the most significant number of nodes selected for the boundary conditions, adapting to the conditions involved in the human body anatomy. The last part of the thoracic aorta is the descending aorta. It acquires this name since it is directed towards the lower part of the human body. In this particular area, the end of the three-dimensional modeling is considered a boundary condition, as in the ascending aorta, a flat face was adapted at the end of the duct to achieve the mapping identification of the node's coordinates. Furthermore, since the case study only involves the thoracic aorta, it was decided to close the duct of the descending aorta without affecting the geometry; most of the nodes of movement (blue ones) are found in this section of the aorta, between the aortic arch and the descending aorta.

On the other hand, movement faces and nodes in the model also represent a fundamental function for developing the numerical simulation. During frontal vehicular collision events, the human body suffers a forward displacement due to deceleration. The safety restraints prevent the impact of the thorax and head with the car's internal elements but generate compression loads on the rib cage. The aorta undergoes compression stress that displaces the aorta in its free parts and does not share contact, such as the boundary conditions described above. It is determined that the nodes in blue tonality without considering the designated boundary conditions assume the characteristic of movement in the three axes that involve the three-dimensional working space. Figure 10 shows specific points to set the boundary conditions and the boundary conditions set.

Boundary condition points established in the model are very close and similar approximations compared to the literature. In addition, the settings integrated into the model must also be configured concerning the appropriate axis allowing to determine the points that should not be displaced when a load is presented. However, if it is of high magnitude, the clamping points are affected.

The FEBIO® solver with Matlab® was used to simulate compression in the frontal part of the 3D model. A color bar shows the displacements generated in the modeling; load simulation shows the displacements from the initial position and acquires shades concerning the color bar. In addition,

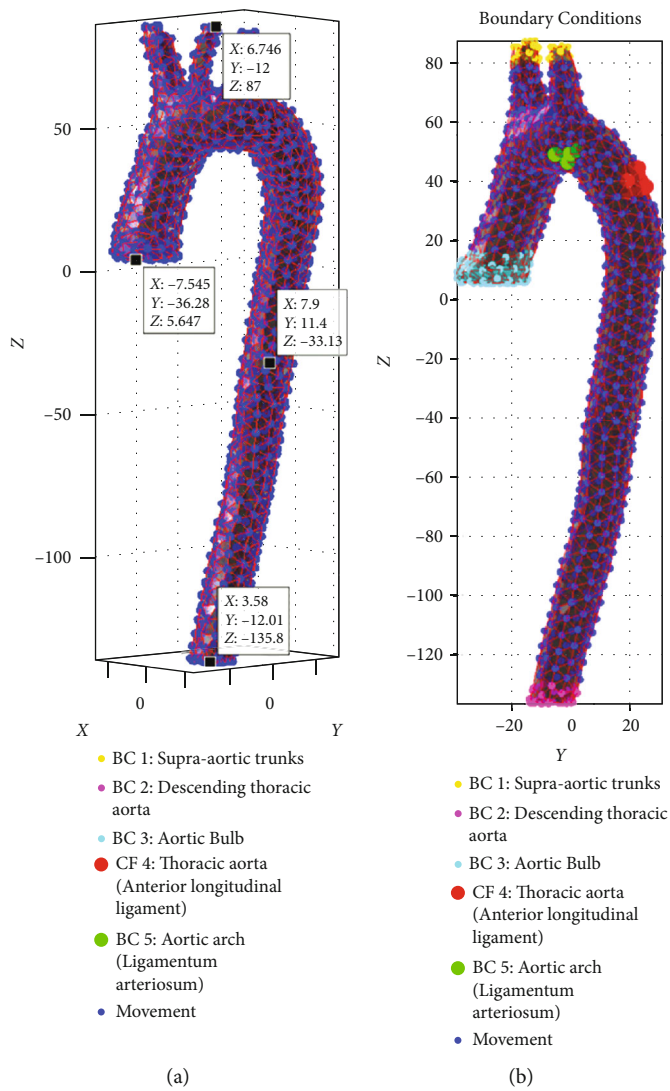

Figure 10: (a) Dimensional model in (b) boundary conditions set.

the results are shown graphically as a function of the stress applied. The Cauchy stress is considered a function of time, and a graph of the displacements is generated in the model; the duration of the simulation (applied load) does not exceed 150 ms as established by the Latin-NCAP regulations. Figure 11 shows the components of the numerical simulation.

The frontal collision focuses on evaluating the artery compression by seatbelt load generated by the restraint system. During the numerical simulation, results were obtained for the three specific parts of the aorta: ascending aorta, aortic arch, and descending aorta. The aortic bulb, the supra-aortic trunks, and the descending aorta are unable to move in the three three-dimensional axes. In comparison, the boundary conditions of the left pulmonary artery and the boundary condition in the posterior part of the model are assigned to disable the movement in the three axes. AIS classifies the injuries that are generated in the human body. It is divided into body region, type of anatomic structure and specific anatomic structure. The displacements, and type of injury in the elements of the rib cage (internal organs) are related to the AIS scale considering the type of injury generated in the aorta. Table 3 shows the classification about the blunt trauma at the aorta according to AIS codes.

Holzapfel's constitutive model is one of the most accepted models to describe arteries. It is a simplified model of the arterial wall in which it is assumed that the response is by two materials that make up the structure of the artery wall. This model is formulated based on the terms of the invariant, the function of the strain energy of the tension-based Cauchy and quasi-incompressible, obtaining the following expression:

$$W = \frac{\mu}{2}(I_1 - 3) + \frac{k_1}{2k_2}\sum_{\alpha=4,6}\left[e^{k_2(I_\alpha - 1)^2} - 1\right]. \quad (1)$$

Furthermore, Holzapfel's viscoelasticity determines the energy density to infinite time can be described as follows:

$$W^{\infty}(C) = W^{\infty}_{\text{vol}}(J) + W^{\infty}_{\text{iso}}(\bar{C}). \quad (2)$$

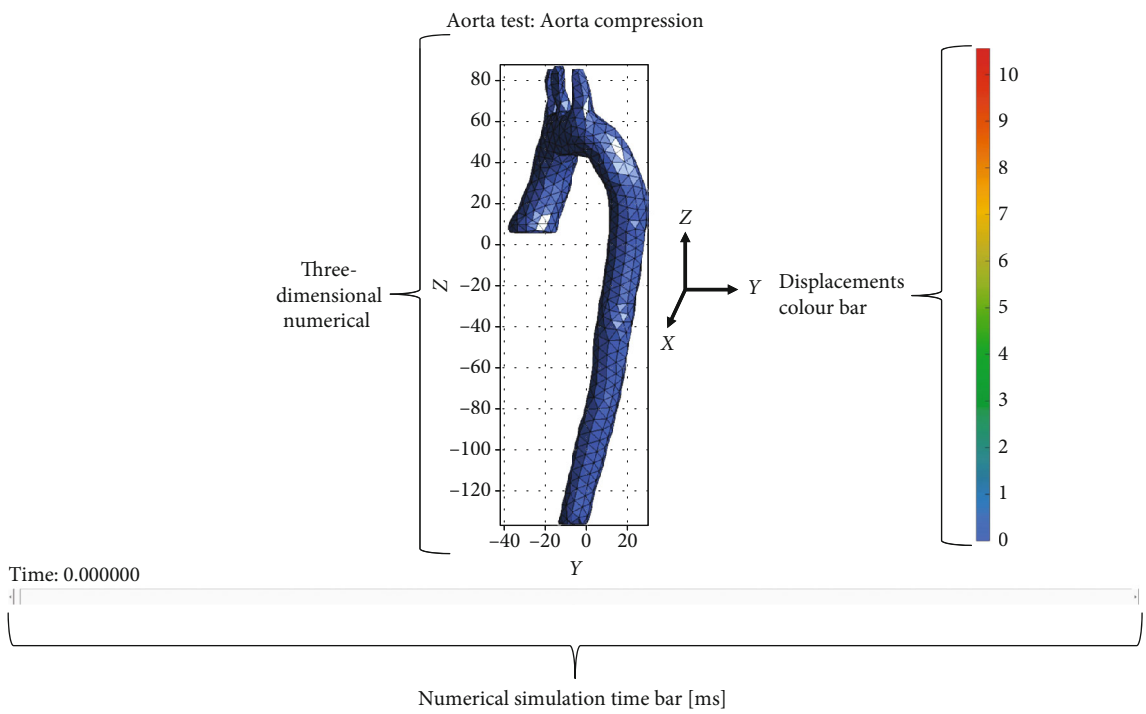

Figure 11: Numerical simulation elements.

Table 3: AIS code and zones for the analysis of lesion in the thoracic aorta.

	AIS code	Zone
Body region	04	Chest
Type of anatomic structure	02	Blood vessels
Specific anatomic structure		
Type of injury	04	Contusion
Head-loss of consciousness (LOC)	N/A	N/A
Spine	04	Thoracic
Vessels, nerves, organs, bones, joints	02	Blood vessels

The function of energy density is determined from C and considering certain internal variables of deformation $\Gamma_a, a = 1, ,, ,m$, as follows:

$$W = W(C, \Gamma_1, , ,\Gamma_m) = W_{vol}^{\infty}(J) + W_{iso}^{\infty}(\bar{C}) + \sum_{a=1}^{m} Y_a(\bar{C}, \Gamma_a). \tag{3}$$

Acquiring the following normalization conditions:

$$\begin{aligned} W_{\text{vol}}^{\infty}(1) &= 0, \\ W_{\text{iso}}^{\infty}(\mathbf{I}) &= 0, \\ \sum_{a=1}^{m} Y_a(\boldsymbol{I}, \boldsymbol{I}) &= 0. \end{aligned} \tag{4}$$

Description through models for describing the mechanical behavior in order to obtain stress and strain patterns applied in organic tissues such as the human aorta. Ogden model is considered as an applicable model with hyperelastic material behavior and expresses the strain energy W considering the main extensions: $\lambda_1, \lambda_2, \lambda_3$.

This mathematical model generates results with an acceptable approximation in stress tests. The applicable expression is

$$\boldsymbol{W} = \sum_{p=1}^{n} \frac{u_p}{\alpha_p} \bullet \left(\lambda_1^{\alpha p} + \lambda_1^{\alpha p} + \lambda_1^{\alpha p} - 3\right). \tag{5}$$

3. Results

During the execution of the numerical simulation, there are specific points in which the aorta's behavior is appreciated when compression stress is applied. For example, in the milliseconds of 24.90, 49.80, 74.70, 99.60, 124.50, and 149.40; it is possible to visualize the displacements in specific areas of the aorta from the aortic bulb to the descending aorta, and the behavior based on the mechanical properties and characteristics of the model is adequate considering the stress applied. Although the numerical simulation duration is 298.00 ms, the compression effect in the aorta ends at the instant of 149.40 ms, and total displacements in the artery are generated at this period. Figure 12 presents the behavior of the aorta at the periods mentioned.

The artery displacements generated explicitly in the descending aorta between the aortic arch and the last part of the descending aorta model considered all boundary conditions. However, the movement on the plane " x " involves esophagus contact (thoracic part). Therefore, the behavior

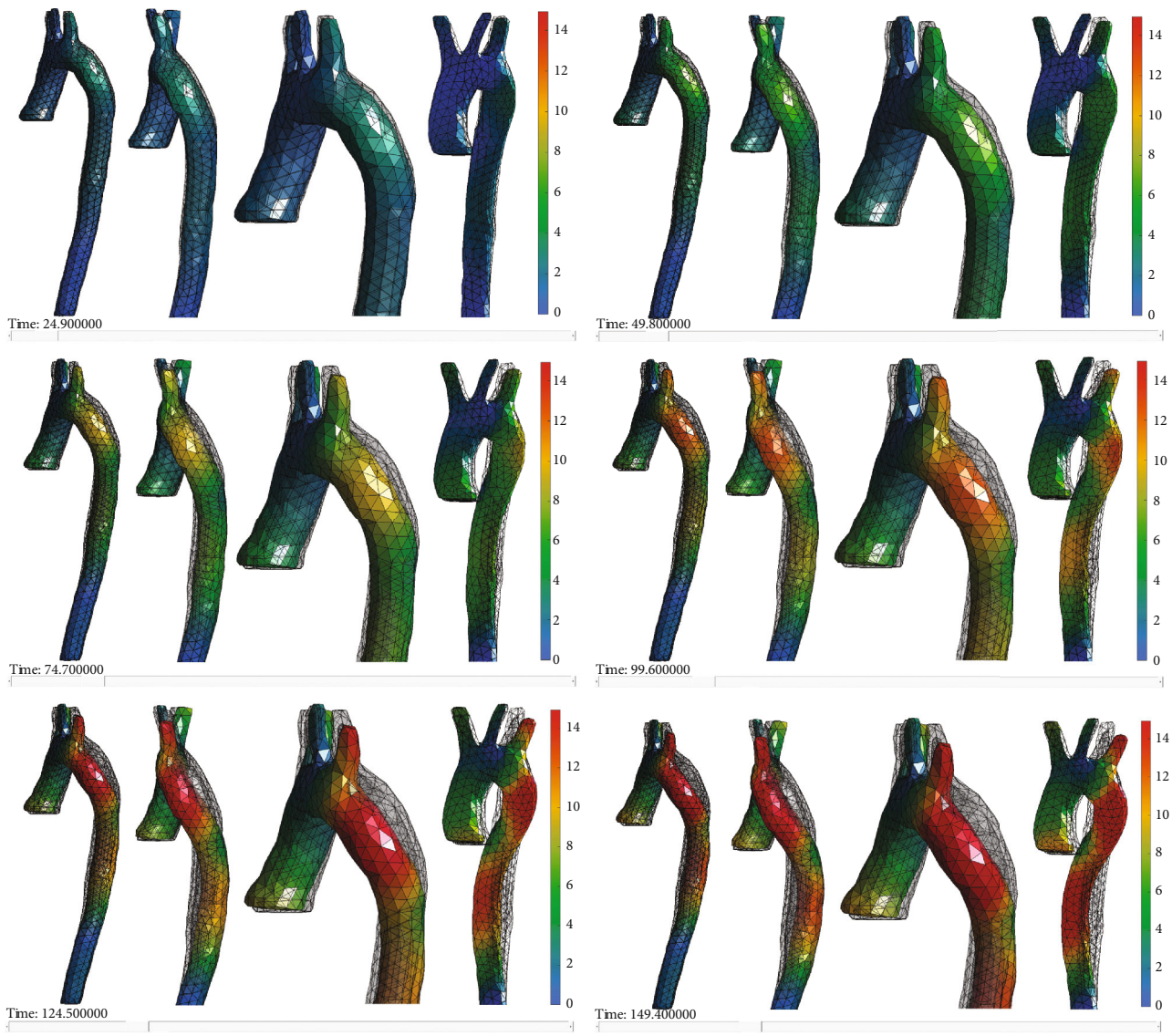

Figure 12: Aorta behavior by compression in milliseconds periods, 24.90, 49.80, 74.70, 99.60, 124.50, and 149.40.

of the thoracic aorta is essential, highlighting that the aortic arch is the area in which the highest displacement is generated from its position, the displacement in 124.50 ms increases to 14 mm, and is considered important because it is where the compression stress is concentrated.

4. Discussions

The study carried out presents a static analysis simulation on the behavior of the arterial wall of the thoracic aorta using MEF. The three-dimensional model developed is configured considering the mechanical properties of hyperelastic soft tissue. In addition, the study considers the origin of blunt trauma by compression loads due to a car collision. However, elements such as the car, passenger compartment, and seat belt are not considered.

An interesting behavior is observed in the common carotid artery since, during compression of the thoracic aorta, the central supra-aortic trunk presents a minimum, and constant displacement through time simulation, which is 1 mm. The position is away from areas that undergo displacement in the thoracic aorta (ascending aorta and aortic arch). The left subclavian artery shows a linear increase from 3 mm to 13 mm of displacement due to its proximity to the aortic arch, while the brachiocephalic trunk presents a maximum displacement reaching 7 mm. The ascending aorta has a maximum displacement up to 6 mm at 149.40 ms. Although the displacement is minimal, it can be considered fatal in higher-speed collision scenarios. Nevertheless, the aorta area does not present serious injuries based on the numerical simulation. Finally, the descending aorta increases an average of 2 mm simultaneously with a total displacement of 14 mm.

It should be noted that considering the numerical simulation constructed, the behavior of the tubular structure near the aortic arch is forced to move to the esophagus (thoracic area). Figure 13 presents the relation of the results shown in Figure 12, and the most affected area at 149.40 ms is the

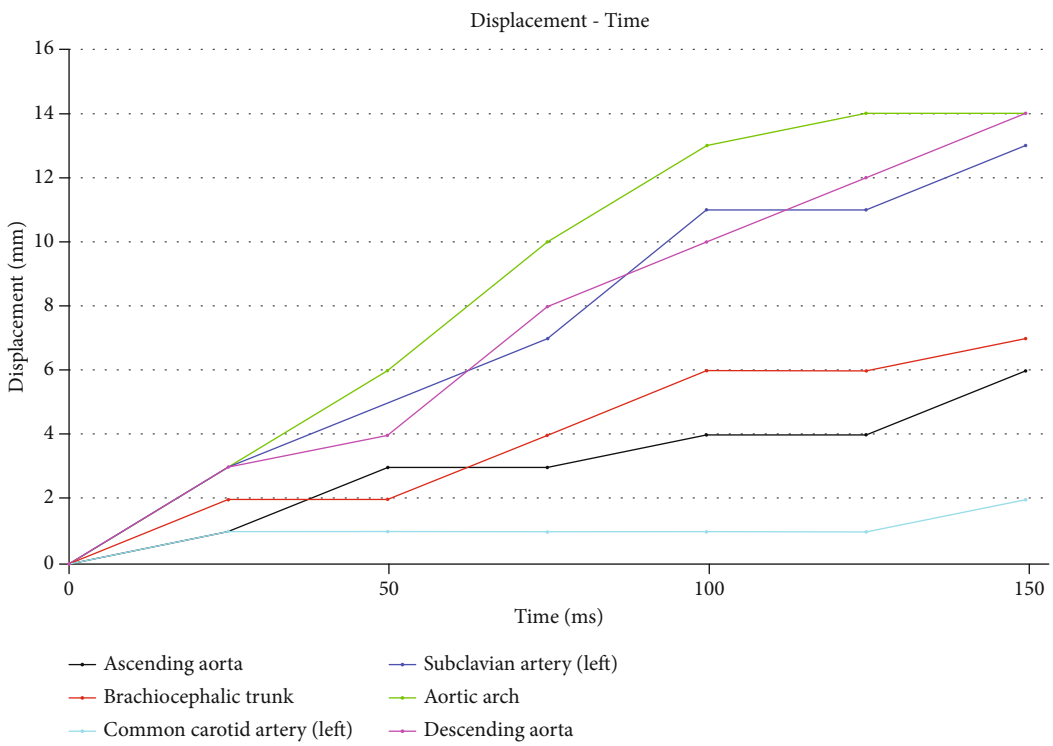

Figure 13: Displacement-time graph of the thoracic aorta artery.

Table 4: AIS coding system.

AIS score	Injury	Description
0	None	None
1	Minor	Superficial
2	Moderate	Reversible injuries; required medical attention
3	Serious	Reversible injuries: hospitalization required
4	Severe	Life-threatening; not fully recoverable without care
5	Critical	Irreversible injury; not fully recoverable even with medical care
6	Unsurvivable	Deadly

aortic arch, which is considered the part of the aorta with the most probability of a rupture. It is also observed that the points where the boundary conditions are concentrated to sustain the model are respected and present minimal displacements as part of the behavior that exists within the rib cage.

The displacements in the arterial wall generated by the compression load during the numerical simulation represent deformations in the artery. The properties that characterize the aorta are of the hyperelastic and viscoelastic types. Although the artery's displacements in the event of a frontal collision are considerable, they do not represent a failure in the material of the artery, so it can be considered that the artery suffers a sudden displacement in the aortic arch that can severely affect blood flow.

During the thorax's impact due to the tension of the seatbelt, the aforementioned car safety systems and the rib cage are also involved. Initially, the element that receives the highest stress compression is the sternum, and it is considered that the transfer of energy towards the aorta is important in relation to the car's impact speed. For this case study, at 64 km/h, the artery undergoes displacements up to 14 mm in the aortic arch and the descending aorta forcing the artery and the left pulmonary ligament to displace. Finally, based on the AIS scale, the degree of injury in the aorta is classified. Therefore, the code corresponds to an AIS 2 with required medical attention and injuries which are reversible. Results show that the aorta is displaced 14 mm from its original position and moderately affected due to contusion in the rib cage. According to the aorta structural behavior in the numerical simulation, it can compare with clinical analysis by Lorenzo et al., which report that the main deformation is at the aortic arch. Wei et al. made a 27 km/h lateral impact simulation, which describes the same behavior at the aortic arch in less displacement due to the stress by the 27 km/h scenario. Zhengwei et al. show the same aortic arch and descending aorta behavior with 5 mm displacement in 30 ms simulation compression load. Finally, Belwadi et al.'s lateral collision

simulation shows that the left subclavian artery is also injured by the stress compression followed by the descending aorta according to its fringe level.

Thus AIS 2 is the code selected for the trauma in this study case as a moderate injury describing there are no affectations to the organs as the numerical results shown in Figure 12. Table 4 shows the AIS coding and its description.

Developed numerical simulations allow analyzing the thoracic aorta's structural behavior in compression load events due to stress by the car seatbelt. The numerical simulation can also set compression stress in three-dimensional models considering boundary conditions to emulate collision scenarios. Numerical simulation construction through specialized computational code by FEM allows creating a three-dimensional workspace, importing an STL object, setting any finite element, assigning material properties, and solving a case study applying stress on the object to predict material behaviors. The aorta's behavior with the applied mechanical characteristics is similar, establishing that the area most affected during compression loads by retention systems is in the aortic arch. It should be noted that the numerical simulation of this work does not include elements that are part of the case study (seatbelt and car) due to the limitation provided by the computer programs used. However, the numerical simulation built by programmed instructions contributes to the construction of any scenario for simulation in organs of the human body.

5. Conclusions

In this work, a numerical simulation of the structural aorta behavior was carried out in a static field, applying compression loads in the ascending aorta of a 3D model, which TC developed. Compression load simulation in the artery was carried out considering the boundary conditions at specific parts of the aorta emulating the stress applied by the tension of the strap of the restraint system of a car. The use of mathematical models based on mechanical tensioners allows the numerical simulation construction to establish the type of material according to the family of soft tissues in which the arterial wall belongs. Ogden and Viscoelastic model application in the solution by matrix methods sets the behavior in the mechanics of the continuous medium of hyper-elastic materials. According to the mathematical applied models, displacements were analyzed through a matrix solver considering the collision event. The anatomical-based coding system by AIS score describes the severity of injuries. Numerical results show that the thoracic aorta at the aortic arch reaches 14 mm displacement and does not represent major injuries to the artery. However, according to the AIS score and medical reports, sudden stress at 64 km/h on the thorax requires medical attention as a protocol in collision scenarios. The results of the proposal for this work are compared with those of other authors and clinical reports.

Data Availability

The data used to support the findings of this study are available from the corresponding author upon request.

Conflicts of Interest

The authors declare that there is no conflict of interest regarding the publication of this paper.

Acknowledgments

The authors acknowledge the financial support for the realization of this work to the Mexico Government by Consejo Nacional de Ciencia y Tecnología (CONACYT) and the Instituto Politécnico Nacional (IPN). The authors also thank the support of project 20210282 and an EDI grant, all by SIP/IPN.

References

[1] C. M. Miguel, *Libro de la salud cardiovascular del Hospital Clínico San Carlos y la Fundación BBVA*, Fundacion BBVA, 2007.

[2] P. Timonov, M. Goshev, I. Brainova-Michich, A. Alexandrov, D. Nikolov, and A. Fasova, "Safety belt abdominal trauma associated with anthropometric characteristics of an injured person—a case report," *Egyptian Journal of Forensic Sciences*, vol. 8, no. 1, 2018.

[3] D. V. Feliciano, "Cardiac, great vessel, and pulmonary injuries," in *Rich's Vascular Trauma*, pp. 71–99, 2016.

[4] K. H. Yang and B. R. Presley, *Modeling the Thorax for Impact Scenarios*, Elsevier Inc., 2018.

[5] J. R. Perry, E. M. Escobedo, and F. A. Mann, "Abdominal aortic injury associated with 'seat belt syndrome," *Emergency Radiology*, vol. 7, no. 5, pp. 312–314, 2000.

[6] M. Fitzharris, M. Franklyn, R. Frampton, K. Yang, A. Morris, and B. Fildes, "Thoracic aortic injury in motor vehicle crashes: the effect of impact direction, side of body struck, and seat belt use," *The Journal of Trauma: Injury, Infection, and Critical Care*, vol. 57, no. 3, pp. 582–590, 2004.

[7] A. E. H. Lorenzo, M. Wilhelmi, and A. M. Anduaga, "Traumatismo torácico y rotura aórtica," *Puesta Al Día En Urgencias, Emergencias y Catástrofes*, vol. 9, pp. 134–145, 2009.

[8] M. M.-C. C. Arregui-Dalmases, J. A. Aso-Escario, F. Bandrés-Moya et al., "Biomecánica del tórax," in *Biomecánica en la valoración médico legal de las lesiones*, pp. 122–128, ADEMAS, Ed, Madrid, 2011.

[9] G.-H. Claudio, *Comportamiento Mecánico de la Aorta Ascendente : Caracterización Experimental y Simulación Numérica*, Universidad Politécnica de Madrid, 2012.

[10] A. Belwadi, J. H. Siegel, A. Singh, J. A. Smith, K. H. Yang, and A. I. King, "Finite element aortic injury reconstruction of near side lateral impacts using real world crash data," *Journal of Biomechanical Engineering*, vol. 134, no. 1, 2012.

[11] J. E. Palomares Ruiz, M. Rodriguez Madrigal, J. G. Castro Lugo, A. Ramirez Treviño, and A. A. Rodriguez Soto, "Modelación y simulación de la arteria aorta a partir de datos clínicos utilizando un modelo fraccional viscoelástico y el método del elemento finito," *Revista Mexicana de Ingeniería Biomédica*, vol. 36, no. 3, pp. 207–219, 2015.

[12] W. Wei, C. J. F. Kahn, and M. Behr, "Fluid–structure interaction simulation of aortic blood flow by ventricular beating: a preliminary model for blunt aortic injuries in vehicle crashes," *International Journal of Crashworthiness*, vol. 25, no. 3, pp. 299–306, 2020.

[13] O. Ramirez, M. Ceccarelli, M. Russo, C. R. Torres-San-Miguel, and G. Urriolagoitia-Calderon, *Experimental Dynamic Tests of RIB Implants*, vol. 68, Springer International Publishing, 2019.

[14] O. Ramirez, C. Torres-San-Miguel, M. Ceccarelli, and G. Urriolagoitia-Calderon, "Experimental characterization of an osteosynthesis implant," *Advances in Mechanism and Machine Science*, vol. 73, no. 16, pp. 53–62, 2019.

[15] I. L. Cruz-Jaramillo, C. R. Torres-SanMiguel, J. A. Leal-Naranjo, and L. Martínez-Sáez, "Numerical child restraint system analysis in 6 years old infant during a dolly rollover test," *International Journal of Crashworthiness*, pp. 1–9, 2020.

[16] I. L. Cruz-Jaramillo, C. R. Torres-San-Miguel, O. Cortes-Vásquez, and L. Martínez-Sáez, "Numerical low-back booster analysis on a 6-year-old infant during a frontal crash test," *Applied Bionics and Biomechanics*, vol. 2018, Article ID 2359262, 2018.

[17] M. Zhengwei, J. Lele, and J. Lianbo, "Development and validation of an occupant biomechanical model for the aortic injury analysis under side impacts," *MATEC Web of Conferences*, vol. 256, article 01001, 2019.

[18] E. G. Janssen, "Eevc test methods to evaluate pedestrian protection afforded by passenger cars," in *Proceedings: International Technical Conference on the Enhanced Safety of Vehicles*, pp. 1212–1225, Washington, DC, USA, 1996, http://www-nrd.nhtsa.dot.gov/departments/nrd-01/esv/esv.html.

[19] D. Pinzón, "La Seguridad Vial, un Asunto de Prioridad Mundial," *Fasecolda*, vol. 155, pp. 67–70, 2015, https://revista.fasecolda.com/index.php/revfasecolda/issue/view/5.

[20] R. Satué-Vallvé, *Análisis de la influencia de la rigidez y la absorción de energía de los materiales aplicados al diseño de una barrera de choque frontal para la evaluación de la compatibilidad entre vehículos*, Universisda Politécnica de Cataluña, 2012.

[21] P. R. Hoskins and I. B. Wilkinson, *Cardiovascular Biomechanics*, Springer, Switzerland, 2017.

[22] J. Gulliver and E. G. Brooks, *Diseases of the Aorta*, Springer, Switzerland, 2019.

Hindawi
Applied Bionics and Biomechanics
Volume 2021, Article ID 9986395, 7 pages
https://doi.org/10.1155/2021/9986395

Research Article

Study on the Effect of Sample Temperature on the Uniaxial Compressive Mechanical Properties of the Brain Tissue

Fengjiao Guan,[1] Guanjun Zhang,[2] Xiaohang Jia,[2] and Xiaopeng Deng[2]

[1]*Laboratory of Science and Technology on Integrated Logistics Support, College of Intelligence Science and Technology, National University of Defense Technology, Changsha 410073, China*
[2]*State Key Laboratory of Advanced Design and Manufacturing for Vehicle Body, Hunan University, Changsha 410082, China*

Correspondence should be addressed to Guanjun Zhang; zgjhuda@163.com

Received 18 March 2021; Accepted 3 July 2021; Published 14 July 2021

Academic Editor: C. R. Torres-San Miguel

Craniocerebral injury has been a research focus in the field of injury biomechanics. Although experimental endeavors have made certain progress in characterizing the material behavior of the brain, the temperature dependency of brain mechanics appears to be inconclusive thus far. To partially address this knowledge gap, the current study measured the brain material behavior via unconstrained uniaxial compression tests under low strain rate ($0.0083\,s^{-1}$) and high strain rate ($0.83\,s^{-1}$) at four different sample temperatures (13°C, 20°C, 27°C, and 37°C). Each group has 9~12 samples. One-way analysis of variance method was used to study the influence of sample temperature on engineering stress. The results show that the effect of sample temperature on the mechanical properties of brain tissue is significant under the high strain rate, especially at low temperature (13°C), in which the hardening of the brain tissue is very obvious. At the low strain rate, no temperature dependency of brain mechanics is noted. Therefore, the current results highlight that the temperature of the brain sample should be ensured to be in accordance with the living subject when studying the biomechanical response of living tissue.

1. Introduction

Craniocerebral injury is one of the common injuries and major causes of death in traffic accidents [1]. Marion showed that 84.1% of cases of severe craniocerebral trauma in children were caused by road traffic accidents and 72.5% of cases of severe craniocerebral trauma in adults were also caused by traffic accidents [2]. Therefore, craniocerebral injury has been a research hotspot in the field of injury biomechanics [1, 3–5]. Compared to biomechanical experiments that can be either hardly possible to perform due to moral reasons or extremely difficult associated with technical challenges and enormous expenses [6–12], the finite element simulation method is a particularly instrumental approach to evaluate the mechanical response of biological tissues under various load conditions and further uncover the mechanism of craniocerebral injury [4, 13, 14]. However, the biofidelity of the finite element model relies on accurate material constitutive parameters. Therefore, it is of great significance to study the factors affecting the constitutive parameters of brain tissue materials.

Brain tissue contains 70% water, 10%~12% lipids, 8% proteins, inorganic salts, organics, and carbohydrates [15]. Its high water content makes the volume modulus of the brain tissue almost equal to that of water with low shear resistance; the brain tissue is prone to shear deformation with respect to volume alteration [16, 17]. Thus far, the biomechanical properties of brain tissue were studied under various loading modes, such as stretching [11, 18, 19], compressing [10, 18, 20, 21], shearing [12, 18], and indentation method [5, 7]. The research indicated that the brain tissue is a medium exhibiting hyperelasticity [7, 10, 11, 19, 20, 22, 23], nonlinear elasticity [3], and nonlinear viscoelasticity [12, 18, 21]. These experimental data can be fitted by the constitutive models, through which the stresses are related to the strains in the form of mathematical expressions governed by model-specific material parameters. For example, Budday et al. compared the five commonly used constitutive models

(e.g., neo-Hookean, Mooney Rivlin, Demiray, Gent, and Ogden) and pointed out that the Ogden model could better represent the hyperelasticity of brain tissue under stretching, compression, and shear conditions [12].

It should be pointed out that there are many factors affecting the mechanical properties of brain tissue, such as anatomical location [12, 13, 18], loading direction [1, 3, 13, 18], sample age [12, 13, 21], and temperature [1, 3, 4, 9, 20]. The experimental results obtained by different research teams are quite different. The mechanical heterogeneity of brain tissue and the inconsistency of test conditions are important reasons for the different experimental results. Although temperature has been recognized as one of the important factors affecting the mechanical properties of brain tissue [1, 3, 4, 20], consistent findings have not been reached yet. For example, Zambra et al. conducted the uniaxial compression test on fresh porcine brain tissue (coronal, Φ13 mm × 2 mm) using split-Hopkinson bar. The results showed that, when the strain was 10%, engineering stress and tangent modulus at storage temperature of 37°C are 3.5 times and 3.2 times than that of 0°C, respectively. By increasing the strain to 70%, engineering stress and tangent modulus at storage temperature of 37°C are 2.4 times and 2.2 times than that of 0°C, respectively [9]. Hrapko et al. studied the shear mechanical properties of fresh porcine brain tissue (corona radiata, Φ12 mm × 2 mm) at five temperatures of 37°C, 30°C, 23°C, 15°C, and 7°C (not explicitly stated as sample temperature or ambient temperature) and suggested that the dynamic shear modulus of brain tissue samples has a significant temperature dependence and the hardening phenomenon increases with decreasing temperature [1, 3]. Contrarily, Rashid et al. showed that there is no significant difference in unconstrained compression engineering stress of fresh porcine brain tissue samples (coronal, Φ15.0 mm × 6.1 mm) within the temperature range of 22°C to 37°C [20].

The above studies about the effect of temperature on the mechanical properties of brain tissue have reached inconsistent conclusions. This may be partially related to test methods and biomechanical response parameters. The above-mentioned study on the effect of temperature on the mechanical properties of brain tissue involves the sample preservation temperature, the test environment temperature, and the sample temperature. It is well known that longer preservation time affects the biomechanical properties of brain tissue [9, 24–26], so more fresh samples are used for biomechanical research. The ambient temperature will affect the temperature of the sample, which depends on the temperature difference between the two, the size of the sample, and the placing time, while the temperature of the sample itself is the direct factor affecting its mechanical properties. Therefore, this paper will study the influence of sample temperatures (13°C, 20°C, 27°C, and 37°C) on the mechanical properties of brain tissue under an unconstrained uniaxial compression test by controlling the consistency of sample temperature and ambient temperature.

2. Method

2.1. Sample Preparation. Twenty-four adult (about 8 months) fresh porcine brain tissue was obtained from the slaughterhouse and stored in a physiological saline solution at 4°C.

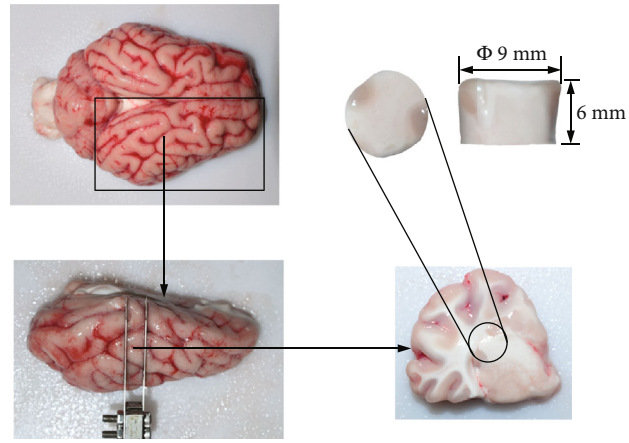

Figure 1: Preparation of brain tissue specimen.

The brain tissue was divided into two symmetrical hemispheres along the corpus callosum with a scalpel blade, and then the hemispheres were cut into slices about 6 mm thick using a combination cutter. With a cylindrical blade cutter (the inner diameter of the cutter is 9 mm) facing the section (coronal plane), a cylindrical sample with a diameter of about 9 mm and a height of about 6 mm mixed with gray matter and white matter was cut from the front to the back (as shown in Figure 1) [9, 20]. Two samples were prepared for each brain hemisphere and randomly assigned to low and high-speed compression tests. During the cutting process, 0.9% saline was continuously sprayed, and all the samples were tested within 6 hours in vitro.

2.2. Experimental Protocol. The experimental equipment is as shown in Figure 2. The air conditioning system was turned on to maintain the ambient temperature in the laboratory at the temperature required to carry out the test (13°C, 20°C, 27°C, and 37°C). The sample, together with the support plate, was placed on an INSTRON 5985 (Instron Corp., Norwood, MA USA) test machine. The sample was subjected to preheating treatment at a set temperature for about 2 minutes using an environmental chamber (MTS-651, Eden Prairie, MN USA), and the compression test was performed after the temperature of the sample reached the ambient temperature. Preheated phosphate-buffered saline (PBS) was sprayed on the support plate and press plate for lubrication to reduce the effect of friction on the biomechanical response of the sample [20]. The sample was preloaded at 0.02 N before formal loading [19, 27]. The compression speed was divided into low speed (0.05 mm/s) and high speed (5 mm/s). The corresponding strain rates were 0.0083 s^{-1} and 0.83 s^{-1}, respectively. The compression ratio was controlled to 50% per compression test. Compression force in the experiment was measured by a force sensor (wmc-1000, Interface Inc., USA) with a range of 9.8 N and recorded by a data acquisition system (DT9838, Data Translation, USA) with a sampling frequency of 1000 Hz.

3. Results

Compression tests at four different sample temperatures (13°C, 20°C, 27°C, and 37°C) under two different loading

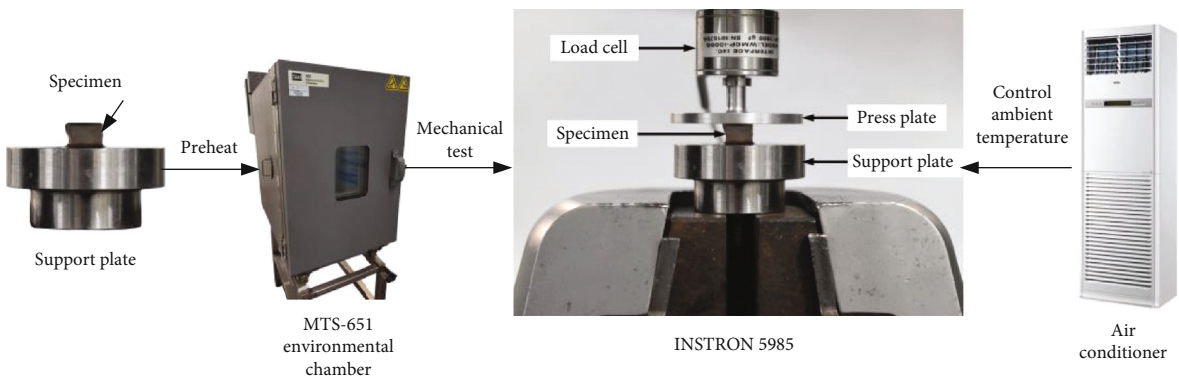

Figure 2: The setup of brain tissue compression test.

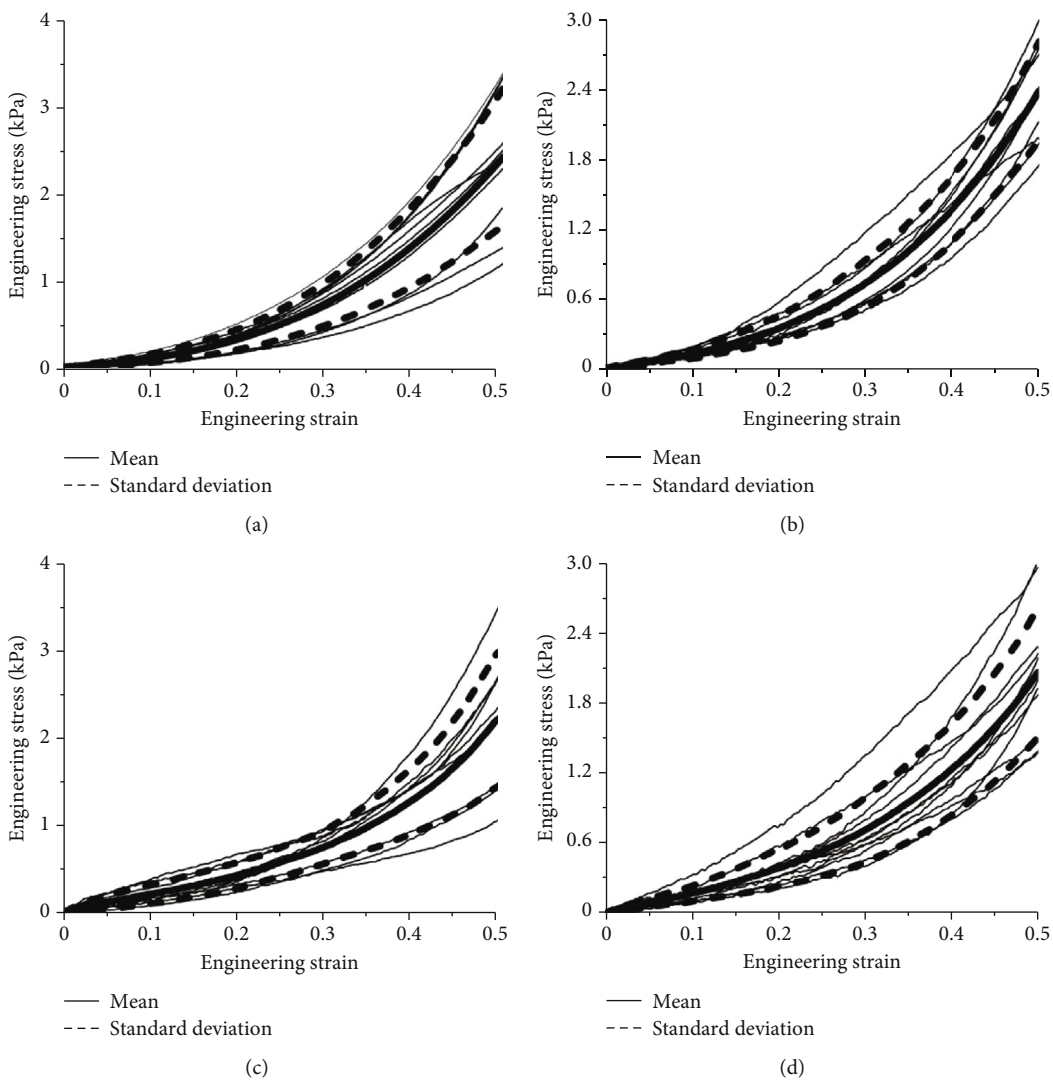

Figure 3: The compression engineering stress-strain curves of brain tissue under low strain rate (0.0083 s^{-1}) condition. (a) 13°C; (b) 20°C; (c) 27°C; (d) 37°C.

rates (0.05 mm/s and 5 mm/s) were performed, and each sample was compressed to a strain of 50%. The ratio of the compressive force to the reference cross-sectional area of the specimen was defined as the engineering stress [20, 28]. Once the compression test was completed, all data were processed using Origin software to obtain the engineering

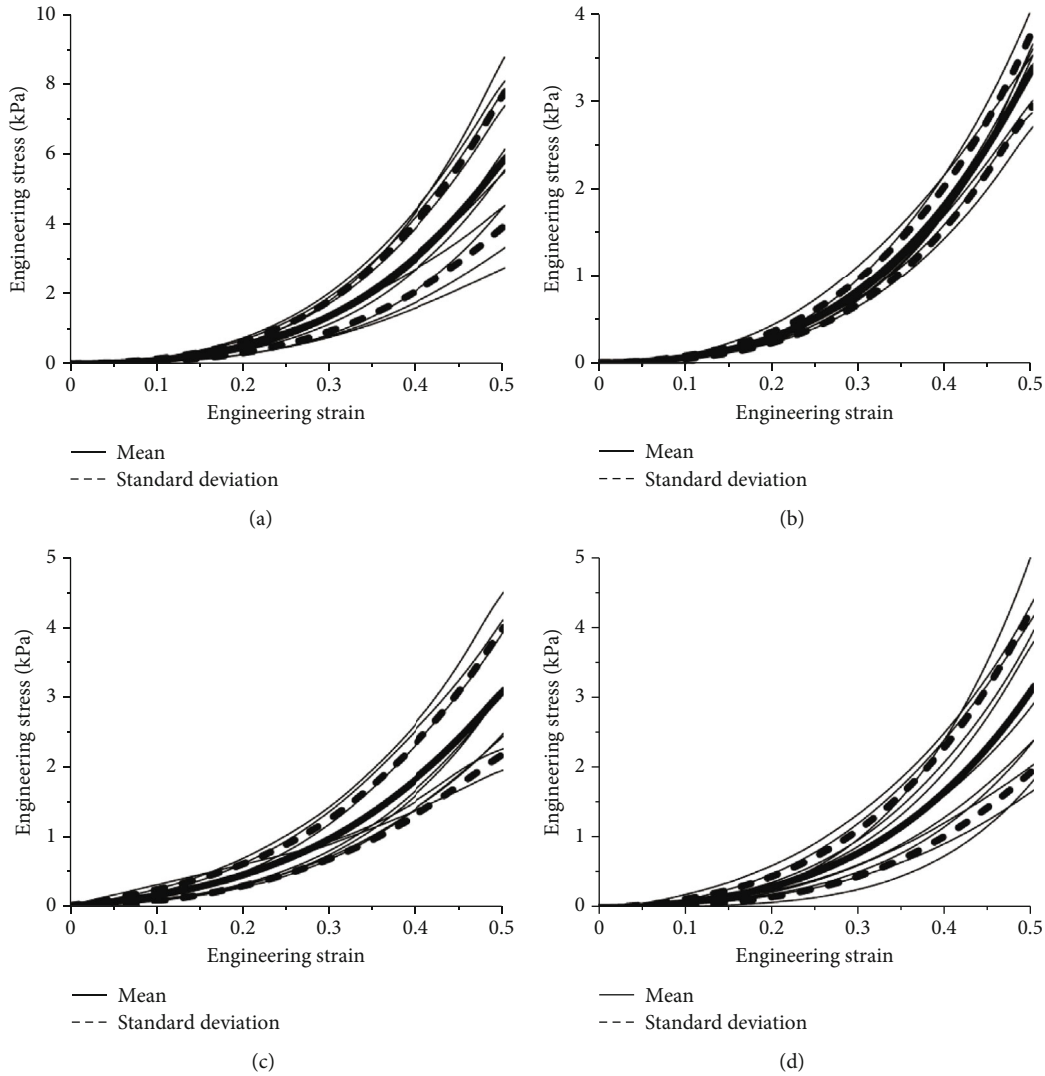

Figure 4: The compression engineering stress-strain curves of brain tissue under high strain rate (0.83 s^{-1}) condition. (a) 13°C; (b) 20°C; (c)27°C; (d) 37°C.

stress-strain curves at two strain rates and specific temperatures, and the average engineering stress-strain curve and standard deviation curve were calculated using linear interpolation method [29, 30], as shown in Figures 3 and 4. The average engineering stress-strain curves corresponding to the temperatures of the four samples under two different strain rates are shown in Figure 5. Under the condition of low strain rate, the influence of sample temperature on the engineering stress-strain curve was not obvious. Under high strain rate conditions, the engineering stress-strain curves at 20°C, 27°C, and 37°C were not significantly different, and the engineering stress at 13°C was significantly higher than those of the other three samples.

In order to study the influence of sample temperature on the mechanical properties of the sample, the corresponding engineering stress of samples was analyzed when the strain was 50%. The results are shown in Table 1. When the strain rate was 0.0083 s^{-1}, the engineering stresses were 2.45 ± 0.82 kPa, 2.39 ± 0.40 kPa, 2.24 ± 0.77 kPa, and 2.09 ± 0.56 kPa at 13°C, 20°C, 27°C, and 37°C, respectively. At a strain rate of 0.83 s^{-1}, the engineering stresses under a strain of 0.5 were 5.85 ± 1.90 kPa at 13°C, 3.37 ± 0.43 kPa at 20°C, 3.10 ± 0.90 kPa at 27°C, and 3.19 ± 1.16 kPa at 37°C.

The effects of temperature on engineering stress at two strain rates were investigated using one-way ANOVA. Under low-speed compression conditions, the effect of temperature on engineering stress was not significant ($p = 0.576$). However, under high-speed compression conditions, the temperature had a significant effect on engineering stress ($p < 0.001$). The difference of engineering stress between samples at different temperatures was further studied by using multiple comparison between groups, as shown in Figure 6. At low strain rate (0.0083 s^{-1}), the engineering stress gradually decreased with the increase of temperature, but the difference between the groups was not statistically significant ($p > 0.05$). At high strain rate (0.83 s^{-1}), the engineering stress of the specimen at 13°C is significantly different from that of the specimen at 20°C ($p = 0.001$), 27°C ($p < 0.001$), and 37°C ($p < 0.001$), and there was no statistically significant difference in engineering stress between samples at 20°C, 27°C, and 37°C ($p > 0.05$).

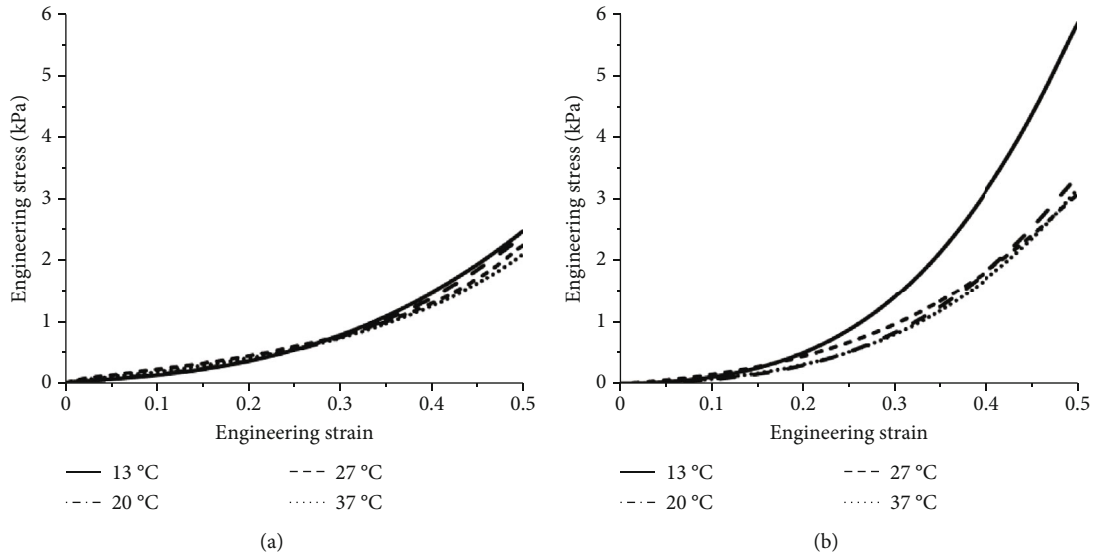

Figure 5: The average engineering stress-strain curves of brain tissue at different temperatures. (a) Low strain rate 0.0083 s^{-1}; (b) high strain rate 0.83 s^{-1}.

Table 1: The maximum engineering stress of sample under different conditions.

Strain rate (s^{-1})	Temperatures (°C)	Engineering strain (kPa)	Sample size
0.0083	13	2.45 ± 0.82	10
	20	2.39 ± 0.40	10
	27	2.24 ± 0.77	9
	37	2.09 ± 0.56	11
0.83	13	5.85 ± 1.90	12
	20	3.37 ± 0.43	9
	27	3.10 ± 0.90	9
	37	3.19 ± 1.16	11

4. Discussion

In this paper, the uncompressed uniaxial compression tests at different loading rates (0.05 mm/s and 5 mm/s) were used to study the compression mechanical properties of brain tissue at different sample temperatures (13°C, 20°C, 27°C, and 37°C). The effect of sample temperature on the compression performance of brain tissue under high strain rate conditions was obvious, especially when the sample temperature was 13°C, the hardening phenomenon of brain tissue was obvious (as shown in Figure 5). One-way ANOVA also showed that the temperature of the sample had a significant effect on the engineering stress at high strain rate ($p < 0.001$). Therefore, the temperature of brain tissue samples should be consistent with the in vivo state in the study aimed at exploring the biomechanical test of living tissue.

The results of this study also showed that there is no significant difference in the engineering stress of brain tissue at the sample temperature of 20-37°C regardless of low strain rate (0.0083 s^{-1}) and high strain rate (0.83 s^{-1}) ($p = 0.727$~0.961). Rashid et al. also carried out an unconstrained uniaxial compression test of brain tissue at dynamics train rates of 30 and 50 s^{-1} at 22°C and 37°C and pointed out that at 22°C and 37°C, there is no statistically significant difference in the engineering stress of brain tissue ($p = 0.856$~0.929). In this study, between 20°C and 37°C, a group of 27°C brain samples was added, and the loading rate extends to quasistatic, which further illustrated that there is no significant difference in the engineering stress of brain tissue within the sample temperature range of 20~37°C. This is consistent with the results of Rashid et al. [20]. Therefore, the mechanical properties of brain tissue obtained from experiments conducted at room temperature in the literature can still be used with caution.

Hrapko et al. analyzed the shear mechanical properties of fresh porcine brain samples at different temperatures of 37°C, 30°C, 23°C, 15°C, and 7°C at a strain rate of 1 s^{-1}. The results showed that the dynamic shear modulus of brain tissue was obviously temperature-dependent and the hardening response increased obviously with the decrease of temperature [1, 3]. In this study, when the sample temperature was 13°C, the engineering stress increased significantly ($p = 0.000$) with the decrease of temperature under the condition of high strain rate, which was consistent with the results obtained by Hrapko et al.

The experimental results in this study also showed that the sample temperature had no significant effect on the compression response of brain tissue at low strain rate, but it had a significant effect at high strain rate. Therefore, the strain rate may also play a role in the effect of sample temperature on the mechanical properties of brain tissue, and it is necessary to further study it in the future.

In this study, the engineering stress of brain tissue was used to analyze the influence of sample temperature. In the finite element model, the biomechanical properties of brain tissue can be characterized by various material constitutive models and corresponding parameters. Therefore, it is more meaningful to explore the influence of temperature on the constitutive parameters of materials in the future.

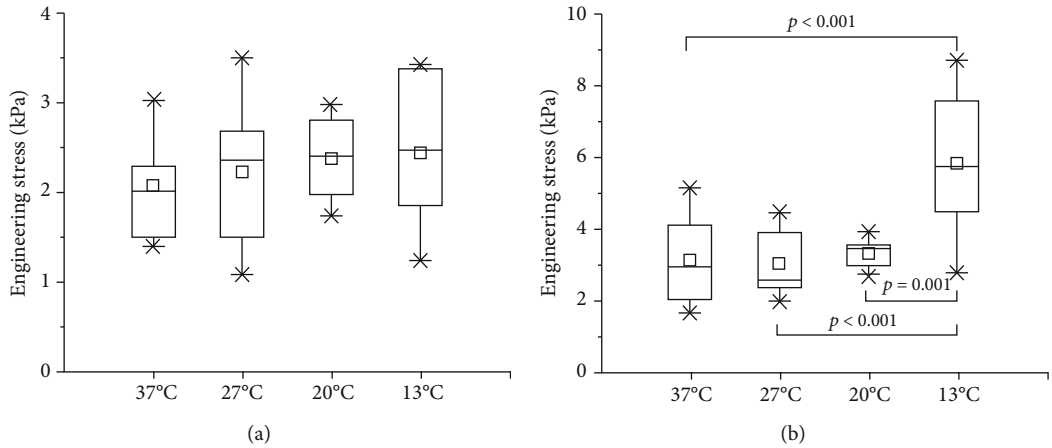

Figure 6: The specimen engineering stress at 50% engineering strain and inter group multiple comparison at four different temperatures. (a) Low strain rate 0.0083 s^{-1}; (b) high strain rate 0.83 s^{-1}.

5. Conclusion

Because the sample temperature is affected by the ambient temperature, it is more valuable to explore the mechanical properties of the brain tissue at the sample temperature. In this study, 81 samples were prepared from 24 porcine brains and randomly divided into 8 groups. The effects of sample temperature (13°C, 20°C, 27°C, and 37°C) on the uniaxial compression mechanical properties of the brain tissue under low (0.05 mm/s) and high (5 mm/s) loading rates were studied, respectively. With the decrease of the temperature of the sample, the engineering stress of the brain tissue was gradually increased. The results of one-way ANOVA showed that the effect of sample temperature on the mechanical properties of brain tissue was not statistically significant ($p = 0.576$) at low strain rate. At high strain rates, the influence of sample temperature on the mechanical properties of brain tissue is significant ($p < 0.001$). When the sample temperature is in the range of 27-37°C, the difference in the biomechanical response of the brain tissue is not obvious. When the sample temperature is lower than 14°C, the brain tissue at high strain rates appears obvious hardening. Therefore, it is necessary to control the sample temperature during the brain tissue test to obtain accurate brain tissue biomechanical response, especially under high strain rate conditions.

Data Availability

The data used to support the findings of this study have not been made available because the data also forms part of an ongoing study.

Conflicts of Interest

The authors declare that they have no conflicts of interest.

Acknowledgments

This research was funded by the Natural Science Foundation of Hunan Province (2019JJ50721 and 2019JJ40034).

References

[1] M. Hrapko, *Mechanical behaviour of brain tissue for injury prediction: characterisaton and modelling, [Ph.D. thesis]*, Technische Universiteitndhoven, 2008.

[2] D. W. Marion, *Craniocerebral trauma*, People's Health Publishing House, 2004.

[3] M. Hrapko, J. A. W. van Dommelen, G. W. Peters, and J. S. H. M. Wismans, "The influence of test conditions on characterization of the mechanical properties of brain tissue," *Journal of Biomechanical Engineering*, vol. 130, no. 3, article 031003, 2008.

[4] A. Kamkin and I. Kiseleva, "Mechanosensitivity of the Nervous System," in *Mechanical properties of brain tissue: characterisation and constitutive modelling*, J. A. W. Dommelen, M. Hrapko, and G. W. M. Peters, Eds., Springer Netherlands, 2009.

[5] J. A. W. van Dommelen, T. P. J. van der Sande, M. Hrapko, and G. W. M. Peters, "Mechanical properties of brain tissue by indentation: interregional variation," *Journal of the Mechanical Behavior of Biomedical Materials*, vol. 3, no. 2, pp. 158–166, 2010.

[6] F. Zhu, X. Jin, F. J. Guan et al., "Identifying the properties of ultra-soft materials using a new methodology of combined specimen-specific finite element model and optimization techniques," *Materials & Design*, vol. 31, no. 10, pp. 4704–4712, 2010.

[7] T. Kaster, I. Sack, and A. Samani, "Measurement of the hyperelastic properties of ex vivo brain tissue slices," *Journal of Biomechanics*, vol. 44, no. 6, pp. 1158–1163, 2011.

[8] R. Prabhu, M. F. Horstemeyer, M. T. Tucker et al., "Coupled experiment/finite element analysis on the mechanical response of porcine brain under high strain rates," *Journal of the Mechanical Behavior of Biomedical Materials*, vol. 4, no. 7, pp. 1067–1080, 2011.

[9] J. Zhang, N. Yoganandan, F. A. Pintar et al., "Effects of tissue preservation temperature on high strain-rate material properties of brain," *Journal of Biomechanics*, vol. 44, no. 3, pp. 391–396, 2011.

[10] B. Rashid, M. Destrade, and M. D. Gilchrist, "Mechanical characterization of brain tissue in compression at dynamic strain rates," *Journal of the Mechanical Behavior of Biomedical Materials*, vol. 10, no. 1, pp. 23–38, 2012.

[11] B. Rashid, M. Destrade, and M. D. Gilchrist, "Mechanical characterization of brain tissue in tension at dynamic strain rates," *Journal of the Mechanical Behavior of Biomedical Materials*, vol. 33, no. 1, pp. 43–54, 2014.

[12] S. Budday, G. Sommer, C. Birkl et al., "Mechanical characterization of human brain tissue," *Acta Biomaterialia*, vol. 48, no. 1, pp. 319–340, 2017.

[13] S. Chatelin, *Improvement of Traumatic Brain Injury Understanding in Case of Head Trauma*, University of Strasbourg, Strasbourg, 2010.

[14] K. Miller, *Biomechanics of the Brain*, Springer New York, 2011.

[15] W. Zhao, S. Ruan, H. Li, and S.-h. Cui, "Analysis on constitutive models and biomechanical properties of brain," *Journal of Medical Biomechanics*, vol. 29, no. 1, pp. 85–92, 2014.

[16] G. T. Fallenstein, V. D. Hulce, and J. W. Melvin, "Dynamic mechanical properties of human brain tissue," *Journal of Biomechanics*, vol. 2, no. 3, pp. 217–226, 1969.

[17] L. Z. Shuck and S. H. Advani, "Rheological response of human brain tissue in shear," *Journal of Basic Engineering*, vol. 94, no. 4, pp. 905–911, 1972.

[18] X. Jin, F. Zhu, H. Mao, M. Shen, and K. H. Yang, "A comprehensive experimental study on material properties of human brain tissue," *Journal of Biomechanics*, vol. 46, no. 16, pp. 2795–2801, 2013.

[19] A. Karimi, M. Navidbakhsh, H. Yousefi, A. M. Haghi, and S. J. A. Sadati, "RETRACTED: Experimental and numerical study on the mechanical behavior of rat brain tissue," *Perfusion*, vol. 29, no. 4, pp. 307–314, 2014.

[20] B. Rashid, M. Destrade, and M. D. Gilchrist, "Temperature effects on brain tissue in compression," *Journal of the Mechanical Behavior of Biomedical Materials*, vol. 14, no. 14, pp. 113–118, 2012.

[21] H. Fan, X. Jin, J. Hu, and K. H. Yanga, "Age dependent material properties of infant and adolescent porcine brain," in *WSU 75th Anniversary Symposium Injury Biomechanics, Prevention, Diagnosis & Treatment*, Detroit, MI, USA, 2014.

[22] F. Velardi, F. Fraternali, and M. Angelillo, "Anisotropic constitutive equations and experimental tensile behavior of brain tissue," *Biomechanics and Modeling in Mechanobiology*, vol. 5, no. 1, pp. 53–61, 2006.

[23] A. Karimi, M. Navidbakhsh, B. Beigzadeh, and S. Faghihi, "Retracted: Hyperelastic mechanical behavior of rat brain infected byPlasmodium bergheiANKA – experimental testing and constitutive modeling," *International Journal of Damage Mechanics*, vol. 23, no. 7, pp. 857–871, 2014.

[24] S. Nicolle, M. Lounis, and R. Willinger, "Shear properties of brain tissue over a frequency range relevant for automotive impact situations: new experimental results," *Stapp Car Crash Journal*, vol. 48, no. 48, pp. 239–258, 2004.

[25] F. Shen, T. E. Tay, J. Z. Li, ,S. Nigen, P. V. S. Lee, and H. K. Chan, "Modified Bilston nonlinear viscoelastic model for finite element head injury studies," *Journal of Biomechanical Engineering*, vol. 128, no. 5, pp. 797–801, 2006.

[26] A. Garo, M. Hrapko, J. A. van Dommelen, and G. W. Peters, "Towards a reliable characterisation of the mechanical behaviour of brain tissue: the effects of post-mortem time and sample preparation," *Biorheology*, vol. 44, no. 1, pp. 51–58, 2007.

[27] T. P. Prevost, A. Balakrishnan, S. Suresh, and S. Socrate, "Biomechanics of brain tissue," *Acta Biomaterialia*, vol. 7, no. 1, pp. 83–95, 2011.

[28] B. Rashid, M. Destrade, and M. D. Gilchrist, "Determination of friction coefficient in unconfined compression of brain tissue," *Journal of the Mechanical Behavior of Biomedical Materials*, vol. 14, no. 5, pp. 163–171, 2012.

[29] G. J. Zhang, J. Yang, F. J. Guan et al., "Quantifying the effects of formalin fixation on the mechanical properties of cortical bone using beam theory and optimization methodology with specimen-specific finite element models," *Journal of Biomechanical Engineering*, vol. 138, no. 9, 2016.

[30] G. Zhang, X. Deng, J. Yang, N. Zhai, X. Deng, and L. Cao, "A study on cortical bone specimens preparation and method to calculate the mechanical parameters," *Chinese Journal of Biomedical Engineering*, vol. 36, no. 1, pp. 75–82, 2017.

Hindawi
Applied Bionics and Biomechanics
Volume 2020, Article ID 8880786, 13 pages
https://doi.org/10.1155/2020/8880786

Research Article

Risk Assessment of Hip Fracture Based on Machine Learning

Alessio Galassi,[1] José D. Martín-Guerrero,[1] Eduardo Villamor,[2] Carlos Monserrat,[3] and María José Rupérez[2]

[1]*Intelligent Data Analysis Laboratory (IDAL), Dept. of Electronic Engineering, ETSE-UV, Universitat de València, Avinguda de la Universitat s/n. 46100 Burjassot, València, Spain*
[2]*Centro de Investigación en Ingeniería Mecánica (CIIM), Universitat Politècnica de València, Camino de Vera s/n, 46022 València, Spain*
[3]*VRAIN, Universitat Politècnica de València, Camino de Vera s/n, 46022 València, Spain*

Correspondence should be addressed to María José Rupérez; mjrupere@upvnet.upv.es

Received 28 September 2020; Revised 17 November 2020; Accepted 8 December 2020; Published 22 December 2020

Academic Editor: C. R. Torres-San Miguel

Identifying patients with high risk of hip fracture is a great challenge in osteoporosis clinical assessment. Bone Mineral Density (BMD) measured by Dual-Energy X-Ray Absorptiometry (DXA) is the current gold standard in osteoporosis clinical assessment. However, its classification accuracy is only around 65%. In order to improve this accuracy, this paper proposes the use of Machine Learning (ML) models trained with data from a biomechanical model that simulates a sideways-fall. Machine Learning (ML) models are models able to learn and to make predictions from data. During a training process, ML models learn a function that maps inputs and outputs without previous knowledge of the problem. The main advantage of ML models is that once the mapping function is constructed, they can make predictions for complex biomechanical behaviours in real time. However, despite the increasing popularity of Machine Learning (ML) models and their wide application to many fields of medicine, their use as hip fracture predictors is still limited. This paper proposes the use of ML models to assess and predict hip fracture risk. Clinical, geometric, and biomechanical variables from the finite element simulation of a side fall are used as independent variables to train the models. Among the different tested models, Random Forest stands out, showing its capability to outperform BMD-DXA, achieving an accuracy over 87%, with specificity over 92% and sensitivity over 83%.

1. Introduction

The continuous increase in life expectancy also raises the incidence of problems related to the weakening of the body due to age. Among the diseases and medical conditions that afflict the countries of the first world, next to the cardiovascular and nervous system ones, but very underestimated in comparison, there are the problems related to bones. In particular, one of the biggest problems for people over 65 is hip fracture due to osteoporosis. Osteoporosis is a skeletal disease primarily characterized by reduced bone mass [1].

According to data from the International Osteoporosis Foundation (IOF), approximately 1.6 million hip fractures occur around the world each year, and in 2050, this number will increase to figures between 4.5 and 6.3 million, due mainly to the aging population [2]. In addition, it is also estimated that about 75% of all fractures occur in women, due to the accumulation of certain risk factors that are linked to gender. In the case of Spain, in 2015, this disease was suffered by 2.2 million women and 0.6 million men, which is practically 1% of the current Spanish population. According to the IOF, it is also estimated that around 330,000 fragility fractures occurred in this country in 2017.

The gold standard for osteoporosis diagnosis and hip fracture risk assessment is currently the Bone Mineral Density (BMD), which is measured by Dual-Energy X-Ray Absorptiometry (DXA) [3]. However, its ability for discrimination between fractured and control cases is limited. BMD distributions for aged people of both groups overlap to a large extent, reducing the classification accuracy to about 65% [4]. Alternative methods have been proposed to calculate the risk of fracture as FRAX and the Garvan [5, 6]; they are statistical

models based on clinical variables in which patient data are compared to a large database from the USA population that includes many clinical features: age, gender, previous fractures, etc. The classification accuracy is about 70% [7], which is not a significant improvement compared to BMD. Another alternative method is measuring the volumetric distribution of the BMD (vBMD) by quantitative computed tomography QCT, which is considered to be more sensitive for osteoporosis [8]. However, although QCT allows to obtain the three-dimensional geometry of the bone and provides the volumetric distribution of BMD, QCT is not integrated in the clinical routine because of its higher cost, processing time, and radiation exposure [9].

Other radically different approaches are the data-based strategies, which consist in training a Machine Learning (ML) model from simulations (e.g., obtained from finite element methods (FEM)) or directly from clinical data. ML algorithms are able to automatically learn nonlinear mappings between several inputs (clinical data, biomechanical data, etc.) and several outputs (e.g., fracture risk factors). Although the training process is relatively slow, once trained, these algorithms provide extremely quick inference times, therefore fulfilling the requirement to predict solutions in real time [10]. This situation opens a possibility to use FEM to generate data off-line that ML models can use to estimate a function that maps inputs (mechanical properties, geometry mesh, boundary conditions, etc.) and outputs (nodal displacements, stresses, strains, etc.) [11] to provide valuable fracture risk predictors in real time.

Machine Learning (ML) has become a robust and relatively usual approach to use in dealing with complex data in order to extract unexpected risk factors in the field of preventive medicine [12]. However, the literature only shows a few studies related to the assessment of the osteoporosis hip fracture. One of the mentioned works can be found in [13]. In this work, a clustering analysis for identifying subgroups of osteoporosis Danish patients based on similarities of traits was carried out. Nine patient clusters of different fracture risks were identified making use of a dataset made up of 10,775 subjects. Four clusters represented postmenopausal women with high-fracture risk profiles of low BMD and between-group differences of poor versus good antiresorptive treatment compliance. One cluster formed by 9% of the subjects was particularly worrisome due to the poor treatment compliance and the very low BMD. Three clusters representing the majority were women with average-fracture risk profiles. Finally, two clusters of perimenopausal and very young women represented low-fracture risk subjects with high BMD and low comorbidity. The authors claimed that for patients older than 60 years a clear distinction between groups of high-fracture risk and average-fracture risk was achieved.

Another remarkable work can be found in [14], where artificial neural networks (ANN) were used to predict hip fracture. The data included information about age, BMD, clinical factors, and lifestyle factors which had been obtained from a longitudinal study that involved 1167 women aged 60 years and above from Dubbo, Australia. The women were followed up for up to 10 years, and during the period, the incidence of new hip fractures was ascertained, although only 90 sustained a hip fracture. Two models were developed: the former was produced by combining only lumbar spine and femoral neck BMD and the latter non-BMD factors, with accuracies of 82% and 84%, respectively. A third model was produced by combining BMD and non-BMD factors, reaching an accuracy of 87%. In summary, the authors showed that ANNs were able to predict hip fracture more accurately than other existing statistical models. However, in spite of the good results, no mechanical attributes were included into the models; as they are considered the main responsible factors for bone failure, this might limit the accuracy of the model if applied to a different dataset.

The mechanical behaviour of the femur during a sideways fall is the main responsibility of hip fracture. In fact, the comparison of the impact load at the fall with the femur strength will determine the bone failure. It is true that BMD is the main contributor to the femur strength, but most of the statistical models do not carry out this comparison to predict hip fracture. Obtaining the mechanical characteristics of the bone has been commonly addressed in the literature by finite element (FE) approaches. QCT-based models construct a biomechanical model from the 3D geometry of the bone and the 3D volumetric distribution of the BMD, which is used to obtain the material properties of the bone [15, 16]. However, even though they are pretty accurate models, its hard implementation, limitations, and computational cost make them unfeasible to be used in clinical routine. In contrast, FE models based on DXA construct the biomechanical model from a 2D representation of the bone and a 2D distribution of the BMD. Therefore, its implementation is easier and their computational cost is lower. In addition, they are very attractive for clinical practice since they do not interrupt the current clinical workflow. These models have provided estimates of the bone strength and have increased the classification accuracy to about 80% [17–19]. Furthermore, fracture risk and Hip Structural Analyses (HSA) derived from both QCT and DXA-based models seem to be significantly correlated [20].

There are some studies that have used ML techniques combining both clinical data and mechanical data. Nishiyama et al. [21] performed patient-specific QCT-based FE analyses under multiple loading conditions to feed a Support Vector Machine (SVM) classifier with a radial basis kernel to address uncertainty in the fall configuration. Jiang et al. [22] investigated the combination of clinical and FE-derived mechanical attributes by means of SVM using a fully parameterized three-dimensional FE model that was created using the given values of geometric attributes; however, this model was global instead of patient-specific. A recent study used high-resolution Magnetic Resonance Imaging- (MRI-) derived data to compare 15 ML classifiers at predicting any kind of osteoporotic fracture [23]; the data comprised bone tissue elasticity and topology of the proximal femur at specific volumes of interest computed with microfinite elements; although this study gave some insight into the relevance of microstructural parameters, the dataset was small and it was not specially focused on hip fracture. It is important to notice that in all these studies the authors did not use a FE

model including patient-specific data describing geometry or BMD distribution. Our conjecture is that including mechanical attributes into a ML model may enhance hip fracture prediction rather than using clinical attributes alone.

In the field of osteoporosis and hip fracture risk assessment, supervised Machine Learning has been scarcely applied in conjunction with computationally driven mechanical attributes. Our group recently published a study where supervised Machine Learning was applied in conjunction with clinical and computationally driven mechanical attributes [24]. A total number of 137 postmenopausal women aged 81.4 ± 6.95 were included in the study and separated into a fracture group ($n = 89$) and a control group ($n = 48$). A semiautomatic and patient-specific DXA-based FE model was used to generate mechanical attributes describing the geometry, impact force, bone structure, and mechanical response of the bone after a sideways fall. After preprocessing the whole dataset, 19 attributes were selected as predictors. SVM with radial basis function (RBF), Logistic Regression (LR), Shallow Neural Networks, and Random Forests (RF) were tested through a comprehensive validation procedure to compare their predictive performance. The results showed that SVM generated the best-learned algorithm for both experimental setups, when clinical and mechanical attributes were included and also when only clinical attributes were taken into account. The first setup generated the best-learned model outperforming the accuracy of BMD by 14pp (79%).

This paper enhances the study presented in [24] by making use of clinical, geometric, and biomechanical variables of the previous database followed by a relevance ranking to find out which variables are the most important ones for the problem. With the selected variables, different ML models were trained. The results show that RF is the best option with an accuracy over 87%, specificity over 92%, and sensitivity over 83%. These values are much better than the current BMD clinically used whose classification accuracy is around 65% and also better than the accuracy of our previous work that was 79%. On top of that, the use of data generation techniques is also remarkable to balance the number of samples in the two classes that were biased originally.

The rest of the paper is outlined as follows. Section 2 presents the methods as well as the characteristics of the dataset and the process to select attributes. The achieved results are shown in Section 3, ending up the paper with the concluding remarks and our proposals for the future research in Section 5.

2. Material and Methods

2.1. Biomechanical Model

2.1.1. Study Population. The database was the same used in [24]. A total number of 137 patients were included in the study with a mean age of 81.4 ± 6.95 years. The inclusion criteria comprised postmenopausal women, older than 50 years, with clinical risk factors related to osteoporosis. Women showing evidence of hip fracture were recruited after being admitted to the emergency room of Hospital Mútua Terrassa (Terrassa, Spain). A densitometry exploration was indicated for each subject.

The scans were performed at CETIR Medical Group, after informed consent was obtained. The time between fracture and DXA acquisition was less than two weeks. DXA scans were taken on the opposite femur to the fractured one using GE Healthcare Prodigy Advance bone densitometer (GE Healthcare, Madison, WI, USA). Subjects were placed on the DXA table in the prone position, with feet parallel to the table and a leg internal rotation of 25-30°, according to the manufacturer's recommendations. The image pixel size was 0.6 mm × 1.05 mm. Patients were separated into a fracture group ($n = 89$), with fall-related incident hip fracture, and a control group ($n = 48$). Within the fracture group, 45 accounted for a trochanteric fracture and 44 for a neck fracture.

2.1.2. Patient-Specific FE Model. A 2D patient-specific FE model was created aimed at obtaining the mechanical attributes to be used in the ML models [24]. For each DXA scan, the proximal femur was segmented manually (Figure 1). Regions of interests (ROIs) defining the trochanteric and neck region were defined semiautomatically. The inputs required for the construction of the FE model were the segmented image of the femur, along with the basic clinical information of the patient (height, weight, and gender).

After the segmentation, the process does not require human interaction. The femur shaft is rotated 10 degrees to the physiological configuration. Pads are placed covering the femoral head and the greater trochanter to avoid local damage due to the applied boundary conditions [25, 26]. The femur, trochanteric pad, and femoral head pad are meshed using TetGen [27]; following a convergence analysis, the mesh size was defined with approximately 60,000 elements, depending on the subject. The model was built under the assumptions of plane strain and linear elasticity behaviour.

The bone material properties were calculated from the BMD per pixel, using the empirical equations obtained in [28–30]. The Poisson ratio was set to 0.3 [31]. Based on previous studies involving mechanical tests [32] and FE models [33], the PMMA (Polymethylmethacrylate) material properties, 1.5 GPa for the Young modulus and 0.37 for the Poisson's ratio, were used for the pads. The heterogeneous material distribution obtained for the Young's modulus is shown in Figure 2(a). This figure shows how the elastic modulus varies according to the BMD distribution from the femur shown in Figure 1.

To obtain the mechanical attributes, a sideway fall was simulated with the FE patient-specific model for each patient. The open-source FE package FEBio [34] was used to obtain the numerical solution. Regarding the boundary conditions, the displacement of the nodes at the distal end of the femoral shaft was totally restricted, and the medial displacement of the nodes at the femoral head pad was prevented. Figure 2(b) specifies the location of the applied loads as well as the location of the boundary conditions. The load was applied to the greater trochanter through its pad, representing the fall-related impact force [35, 36]. This load was

(a) (b)

Figure 1: Original image from the iDXA densitometer database enhanced by a Gaussian filter (a). Manually segmented image (b).

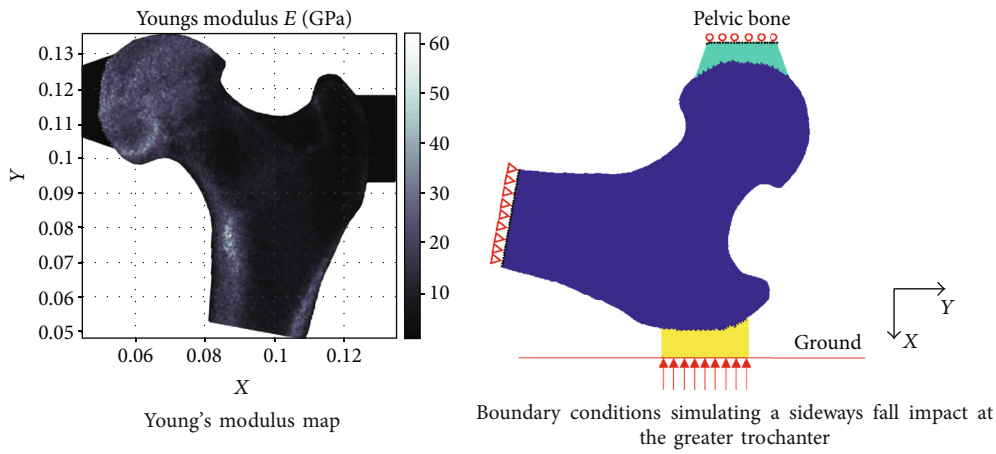

(a) (b)

Figure 2: Material properties, loading, and boundary conditions automatically generated.

calculated with the mass-spring impact model of [37], whose input variables were the weight, the height, and the gender of the patient. Once the peak impact force (FPK) was obtained, the attenuated impact force (FP) was calculated subtracting the attenuation force: $\mathrm{FAT} = 71 \cdot \mathrm{STH}$, based on previous studies regarding the effect of soft tissue thickness (STH) [38] and correlations between body mass index (BMI) and STH [39]. Finally, the applied load pressure over the hip (HP) was computed dividing the attenuated impact force by the length of the greater trochanter pad (b) and a subject-specific thickness (t) [24].

2.2. ML Models

2.2.1. Inputs to the ML Models. Five groups of attributes where collected for each patient [24]: clinical, geometrical, fall-related, bone tissue-related, and that derived from the FE analysis (FEA). Table 1 shows the clinical attributes obtained from the clinical report; mean values and standard deviations (SD) are provided for each attribute and both groups (fractured and control).

The general scheme to obtain the geometrical attributes is shown in Figure 3. This figure graphically describes the geometrical attributes to introduce in the model. These attributes were obtained through a morphometric analysis performed on the proximal femur geometry [19]. Their values are shown in Table 2.

The fall-related attributes computed for each patient are shown in Table 3. Regarding to bone tissue structural properties, the cortical bone was defined as having an apparent density greater than $1.0\,\mathrm{g/cm^3}$ [33]. The percentage of the trabecular bone (TB) and cortical bone (CT) within the femur bone was estimated using this threshold as well as the average Young's modulus within each tissue (TBE and CTE). These values are shown in Table 4.

From the FE linear simulation of the side-fall performed with FEBio, several mechanical attributes were selected and they are shown in Table 5; some of them were computed to define the failure of the whole bone as the load-to-strength-ratio (LSR) and the femoral strength (FS), following the criterium of [15]. LSR was defined as the minimum ratio in a contiguous area of $9\,\mathrm{mm^2}$. This area comprised the elements with the highest ratios between the Principal Compressive Strain and the Compressive Yield Strain. The most common sites for femur fracture are the neck and the trochanteric regions. Because of this, mechanical attributes at each region were computed (index N is used for the variables at neck region, and index T for the variables at the trochanteric region). The volume weighted average value of maximum and minimum principal stresses (S_1 and S_3), the maximum and minimum principal strains (E_1 and E_3), the major principal stress (MPStress), the major principal strain (MPStrain), the strain energy density (SED), and the fracture risk index (FRI) were computed. MPStress and MPStrain were defined

Table 1: Clinical attributes.

Clinical attributes			
Attribute	Description	Fractured (mean ± SD)	Control (mean ± SD)
Age (years)	Patient's age	81.39 ± 6.98	82.56 ± 3.88
Height (cm)	Patient's height	152.67 ± 7.09	151.75 ± 5.09
Weight (kg)	Patient's weight	63.61 ± 14.03	65.21 ± 10.01
BMI (mm)	Body mass index	27.28 ± 5.70	28.31 ± 4.02
BMD (g/cm^2)	Total Bone Mineral Density	0.70 ± 0.13	0.8 ± 0.1

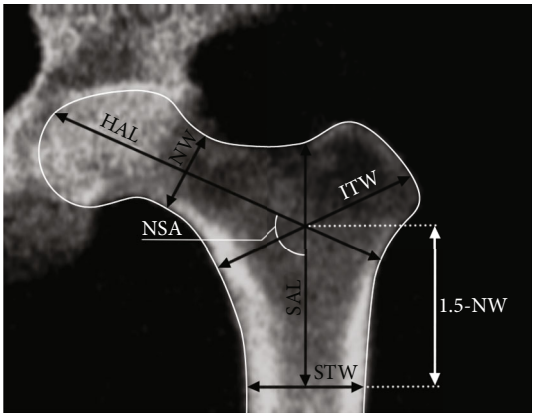

Figure 3: Graphical description of geometrical attributes [24].

as the maximum eigenvalue in the stress and strain tensor, respectively. FRI was computed as the weighted average ratio between the Von Mises stress and the yield stress in the region.

To build the model, the cohort (137 patients) was divided into training (70% of the data) and test (the remainder 30%) with an equal distribution of fractured and healthy patients. Since the number of subjects used for training might be insufficient to obtain conclusive results, Synthetic Minority Over-sampling Technique (SMOTE) was used [40]. The goal of using SMOTE is two-fold: the first one is to increase the size of the dataset so that models can be trained with a more meaningful information and have more parameters without overfitting the data, and the second one is to balance both classes (fractured and control). Classification models may worsen their performance when dealing with unbalanced classes; hence, by creating synthetic samples, both classes can have a similar number of samples. In particular, the number of samples was increased up to 400 distributed in 200 of healthy and 200 of fractured samples. For the sake of reliability, the synthetic samples produced by SMOTE were only applied to the training set in order to ensure that potentially incorrect synthetic points did not affect the models eventually obtained.

2.2.2. Attribute Selection Process. After a process of attribute normalisation, the selection of the most significant attributes was performed in two steps: Principal Component Analysis (PCA) and correlation analysis. Table 6 shows the percentage of variance included in the 39 components of the PCA. Thus, the first principal component (with the 91.88% of the accumulated variance) is clearly dominant compared to the rest. Moreover, adding the second and the third components, we can represent 99% of the total variance of the dataset. Since PCA is a linear combination of all the attributes, it is necessary to analyse the contribution of each one to the linear combination. As most of the attributes have very low weights (between 10^{-3} and 10^{-15}), their contribution can be deprecated. Those principal attributes with significant contribution (weights ≈1) to the first six principal components are the following:

(i) PC1: TB and CT

(ii) PC2, PC3, and PC4: BMI, STH, FPK, FAT, and FP

(iii) PC5: BMD, HP, FRI_N, and FRI_T

(iv) PC6: BMD, HP, TBE, LSR, FRI_N, and FRI_T

Focusing on the three first principal components that, as mentioned above, contain 99% of the variance, only seven make a contribution:

(i) TB: ratio of trabecular bone

(ii) CT: ratio of cortical bone

(iii) BMI: body mass index

(iv) STH: soft tissue thickness

(v) FPK: peak impact force

(vi) FAT: force of attenuation

(vii) FP: attenuated impact force

Additionally, to the PCA Analysis, a correlation analysis was performed: Pearson's correlation index and Spearman's Rank correlation index were obtained. Figure 4 shows Pearson's correlation index of all 39 attributes. The coloured squares with ones inside mark the pair of attributes with correlation higher than 0.9; all except one of the high-correlated attributes were hence removed in order to reduce the dimensionality of the problem.

Pearson's correlation is based on two hypotheses: the populations are normally distributed and the subpopulations do not have the same variance. If at least one of the two hypotheses fails, Pearson's index should not be applied. To avoid these limitations, we have also made use of Spearman's

Table 2: Geometrical attributes.

Geometrical attributes			
Attribute	Description	Fractured (mean ± SD)	Control (mean ± SD)
NW (mm)	Neck width	29.29 ± 2.02	29.68 ± 2.32
HAL (mm)	Hip axis length	89.74 ± 6.31	88.98 ± 5.48
NSA (°)	Neck-shaft axis angle	126.48 ± 6.11	124.21 ± 6.24
SAL (mm)	Shaft axis length	83.16 ± 5.34	85.79 ± 5.19
ITW (mm)	Intertrochanteric width	50.29 ± 3.12	50.15 ± 3.32
STW(mm)	Subtrochanteric width	27.65 ± 2.17	26.44 ± 1.52
FA (mm^2)	Proximal femur area	4580.09 ± 490.35	4574.10 ± 372.61

Table 3: Fall-related attributes.

Fall-related attributes			
Attribute	Description	Fractured (mean ± SD)	Control (mean ± SD)
STH (mm)	Soft tissue thickness	30.43 ± 13.43	32.85 ± 9.42
FPK (N)	Peak impact force	5206.08 ± 641.10	5284.01 ± 455.86
FAT (N)	Attenuation force	2160.27 ± 947.06	2332.19 ± 668.80
FP (N)	Impact force	3045.81 ± 518.10	2951.82 ± 371.04
HP (MPa)	Hip pressure	6.74 ± 1.14	6.46 ± 0.87

Table 4: Attributes related to the bone tissue.

Bone tissue related attributes			
Attribute	Description	Fractured (mean ± SD)	Control (mean ± SD)
TB (%)	Percentage of trabecular bone	86.94 ± 9.04	82.10 ± 8.92
TBE (GPa)	Average Young's modulus of trabecular bone	3.59 ± 0.53	3.85 ± 0.39
CT (%)	Percentage of cortical bone	13.06 ± 9.04	17.90 ± 8.92
CTE (GPa)	Average Young's modulus of cortical bone	10.89 ± 1.96	11.57 ± 1.00

correlation that basically translates the values into ranges before calculating the correlation coefficients. As in the previous case, Figure 5 shows the corresponding heat map. Figure 6 joins Spearman's and Pearson's correlations in a single visualisation.Starting from the seven variables selected by the PCA, our proposal is to include some additional features as the result of the correlation analysis. In particular, we considered those variables which correlated with (at least) four other attributes not previously included by the PCA. The columns of Table 7 show the most highly-correlated variables not previously included by the PCA and the rows those features linked to them with a correlation higher than 0.9 (marked with the check sign). These are HP, S3_N, FRI_N, and FRI_T. It is remarkable that only four features can include most of the information stored in 18 variables.

A final analysis was done for those features already selected by the PCA but with a high interdependence according to the corresponding correlation coefficients, namely, BMI, FAT, and STH. In particular, FAT is calculated as follows:

$$\mathrm{FAT} = 71 \times \mathrm{STH}\left(\mathrm{g/cm^2}\right), \tag{1}$$

while STH is (for female patients) as follows:

$$\mathrm{STH} = 2.3451 \cdot \mathrm{BMI} - 33.4440\left(\mathrm{g/cm^2}\right), \tag{2}$$

And hence,

$$\mathrm{FAT} = 71 \cdot \left(2.3451 \cdot \mathrm{BMI} - 33.4440\right)\left(\mathrm{g/cm^2}\right). \tag{3}$$

Due to this high interdependence, FAT and STH were removed because BMI is more easily and routinely collected. Besides, it can also be observed that TB and CT are linked by a strong correlation. In fact,

$$\mathrm{CT} + \mathrm{TB} = 1. \tag{4}$$

Therefore, only one attribute is enough to include the information provided by the two. The variable TB was eventually selected. Summing up, eight attributes out of 39 were finally used to build the ML models. These eight attributes actually included information related to 26 out of the 39 attributes according to the correlation analysis (Table 8).

Table 5: Attributes obtained from the FE analysis of the side fall.

		FE analysis attributes	
Attribute	Description	Fractured	Control
N = neck; T = trochanter		(mean ± SD)	(mean ± SD)
LSR	Load-to-strength-ratio	0.98 ± 0.65	0.63 ± 0.28
FS (N)	Femoral strength	4421.34 ± 2553.70	5285.70 ± 1718.72
S1_N (MPa)	Maximum principal stress	1.49 ± 0.40	1.46 ± 0.36
S3_N (MPa)	Minimum principal stress	−3.88 ± 0.77	−3.81 ± 0.68
E1_N (μstrain)	Maximum principal strain	1042.10 ± 430.64	816.49 ± 180.71
E3_N (μstrain)	Minimum principal strain	−2250.30 ± 1016.03	−1689.79 ± 400.75
MPStress_N (MPa)	Major principal stress	5.15 ± 1.07	5.12 ± 0.94
MPStrain_N (μstrain)	Major principal strain	2353.53 ± 1034.01	1784.85 ± 414.42
SDE_N (J/m^3)	Strain energy density	7473.06 ± 4113.33	5669.81 ± 1903.91
S1_T (MPa)	Maximum principal stress	0.40 ± 0.13	0.38 ± 0.11
S3_T (MPa)	Minimum principal stress	−2.94 ± 0.55	−2.84 ± 0.49
E1_T (μstrain)	Maximum principal strain	689.95 ± 363.99	499.23 ± 124
E3_T (μstrain)	Minimum principal strain	−1457.57 ± 875.67	−1105.74 ± 273.43
MPStress_T (MPa)	Major principal stress	3.24 ± 0.59	3.12 ± 0.52
MPStrain_T (μstrain)	Major principal strain	1571.41 ± 883.43	1122.79 ± 276.95
SDE_T (J/m^3)	Strain energy density	3536.94 ± 2194.64	2540.23 ± 896.58
FRI_N (μstrain)	Fracture risk index	0.32 ± 0.14	0.24 ± 0.06
FRI_T (μstrain)	Fracture risk index	0.21 ± 0.12	0.15 ± 0.04

Table 6: Percentage of variance included in the 39 components of the PCA.

PC1	PC2	PC3	PC4	PC5	PC6	PC7-39
91.88%	5.28%	2.16%	0.38%	0.26%	0.04%	0%

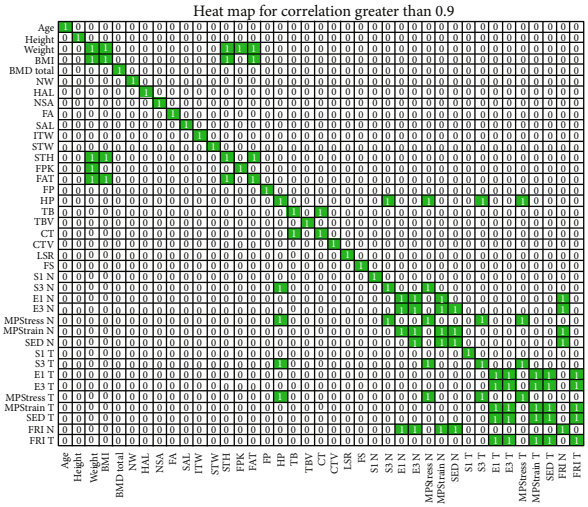

Figure 4: Pearson's correlation: heat map considering a threshold of 0.9. The white zeros represent a correlation lower than the threshold while the coloured ones stand for a correlation equal or higher than 0.9.

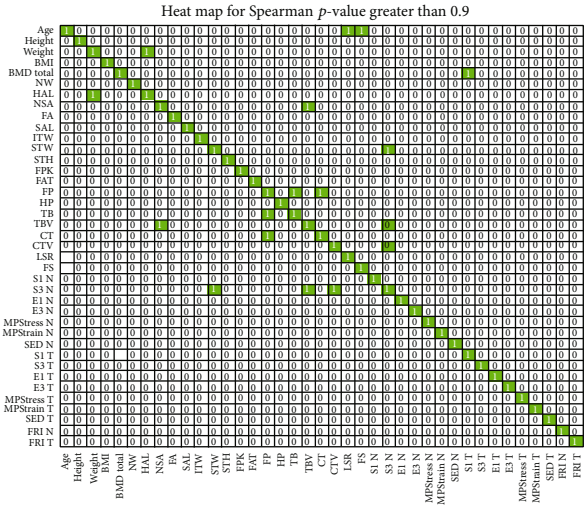

Figure 5: Spearman's correlation: heat map considering a threshold of 0.9.

2.2.3. Fracture Discrimination. To build the classifier, we considered some of the most popular ML approaches: LR, SVM, Decision Trees (DT) and RF. All the models were trained considering that the positive class—coded as 1—corresponds with fractured patients and the negative class—coded as 0—with control samples. The goodness of the models was assessed by means of sensitivity (Se), specificity (Sp), and accuracy (Acc).

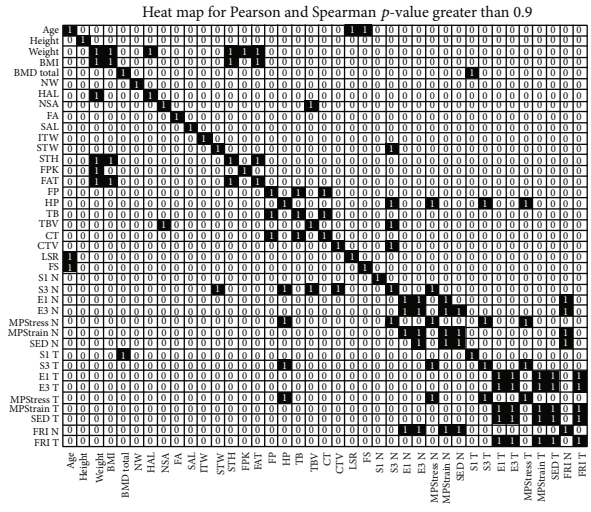

Figure 6: Heat map result of joining the information provided by Person's and Spearman's indices: the black squares represent a correlation higher than 0.9 while the white zeros indicate that the threshold is not reached.

LR was obtained after 1000 trials, randomly selecting the training and test sets. After this random selection, SMOTE was applied to the training set to increase the number of training samples. We also analysed if increasing the number of predictive attributes could improve the prediction results. The features that were added for this analysis were NW, NSA, FA, and SAL that were the lowest correlated attributes not previously considered. A clear degradation of the results was observed when including even more attributes.

As the data set is considerably sparse, SVM could be a good option to model it. Different kernels were considered: linear; linear with posterior probability regions; sigmoid; sigmoid with posterior probability regions; Gaussian; Gaussian with posterior probability regions; and Bayesian with posterior probability regions. As in the case of LR, each SVM was run 1000 times with random selection of training and test sets.

With respect to DT, the same experimental setup was taken into account. The Gini score was used as a splitting criterion. Finally, RF also followed the same training procedure. Different architectures were considered trying to avoid overfitting by limiting the number of trees and their depth.

3. Results

The mean values, standard deviations, and best result among the 1,000 runs are shown in the tables describing the performance of the different models; all results correspond with the test sets. The eight attributes selected as the result of applying PCA and correlation were taken into account; besides, an analysis with 12 features adding the four features mentioned in Section 2.2.3 was also considered.

3.1. Logistic Regression. Tables 9 and 10 show the results achieved by LR using eight and 12 predictive attributes, respectively. Although the best model does yield a very powerful result, the mean values of Se, Sp, and Acc slightly improve the ones provided by the widely used BMD. There are no meaningful differences between the results obtained with eight or 12 features.

3.2. SVM Models. The results obtained by the seven SVM models described in Section 2.2.3 are shown in Tables 11–17. There is a remarkable difference between Se and Sp. Obviously, a model capable of classifying well both classes is always desired, but if the model has to be biased to one of the classes and in order to have a model useful for its real application, sensitive models are preferred. As a result, the number of false negatives is very low, and hence, the predictive capability to detect fractured patients is very high. This is why in order to achieve an Acc as high as possible, we decided to bias the model towards Se. The obtained models are sensitive enough, but unfortunately, the Sp is so poor (near 50%) that would not justify its actual use as a clinical decision support system (CDSS). SVM in general do not benefit from the inclusion of the four additional features.

3.3. Decision Trees. Table 18 shows the results achieved by DT. They do not benefit from the use of the additional features, likely because it reduces the density of branches in the tree and hence its ability to find homogeneous groups of patients. The results are slightly worse than those provided by LR and quite close to what BMD can attain. The standard deviations are too large suggesting the low reliability of the modelling.

3.4. Random Forest. In the case of RF, the robustness of the model is in its own design formed by many single DT so the experimental setup of 1,000 runs was not considered here. For the sake of a fair comparison, RF were made up of 1,000 trees. Therefore, no mean values and standard deviations are given in Table 19, which describes the RF results. The inclusion of the four additional features has a positive effect in the RF performance, slightly improving Se, Sp, and Acc. RF provides the best results of all the tested models with great prediction capabilities for both classes, turning out to get an Acc of 87%, well above the Acc reported by BMD.

Although this work can be considered a pilot study, the promising results yielded by RF encourage us to carry on with the study, hopefully increasing the size of the dataset. If RF performance is similar when applied to a large cohort of subjects, we reckon that its use as CDSS should be taken into account.

4. Discussion

As has been shown, the Linear Regression approximation has quite poor results. The low ratios of sensitivity, specificity, and accuracy only a little over 70% with extremely high standard deviation (higher than ±10%) transform Logistic Regression in a bad approximation. Bearing in mind, in addition, there can be no underfitting (we got 200 samples because of the use of SMOTE) and neither overfitting, as 8-12 features are less than a tenth of the number of subjects. It can be observed that using more attributes does not significantly improve the behaviour of the model.

With regard to the SVM, it is clear that the sigmoid totally misunderstands the "shape" of the hyperplane. The

Table 7: Variables whose correlation is higher than 0.9 and was not included by PCA are shown in the columns. The rows show variables that are highly correlated with the column attributes, coded by the check sign.

	HP	S3_N	StressN	StrainN	E1_T	E3_T	StressT	StrainT	FRI_N	FRI_T	Final
STW		✓									✓
HP		✓	✓				✓				✓
TBE		✓									✓
CTE		✓									✓
S3_N	✓		✓								✓
E1_N				✓					✓		✓
E3_N				✓					✓		✓
StressN	✓	✓					✓				✓
StrainN								✓	✓		✓
SED_N				✓				✓	✓		✓
S3_T	✓		✓				✓				✓
E1_T						✓				✓	✓
E3_T					✓					✓	✓
StressT	✓		✓								✓
StrainT					✓	✓				✓	✓
SED_T					✓	✓		✓		✓	✓
FRI_N				✓							✓
FRI_T					✓	✓		✓			✓

Table 8: Attributes directly included and those included because of their high correlation (≥0.9).

Directly included	Correlation ≥ 0.9	
BMI	Weight	S3_T
FPK	STH	E1_T
FP	TBE	E3_T
HP	CTE	MPStress_T
TB	E1_N	MPStrain_T
S3_N	E3_N	SED_T
FRI_N	MPStress_N	FAT
FRI_T	MPStrain_N	STH
	SED_N	CT

Table 9: Results for Logistic Regression with the selected 8 features.

8 features	Mean	St. deviation	Best
Sensitivity	68.22%	12.61%	94.44%
Specificity	72.69%	12.77%	84.61%
Accuracy	70.10%	8.92%	90.32%

Table 10: Results for Logistic Regression with 12 features.

12 features	Mean	St. deviation	Best
Sensitivity	70.33%	12.31%	100.00%
Specificity	71.46%	13.62%	84.61%
Accuracy	70.81%	10.15%	93.54%

Table 11: Results of SVM with a linear kernel.

Linear	Mean	St. deviation	Best
Sensitivity (8 features)	61.22%	10.20%	83.33%
Specificity (8 features)	76.69%	10.85%	92.30%
Accuracy (8 features)	67.71%	8.81%	87.10%
Sensitivity (12 features)	68.44%	9.76%	88.89%
Specificity (12 features)	75.62%	13.35%	92.30%
Accuracy (12 features)	71.45%	9.17%	90.32%

Table 12: Results of SVM with a linear kernel and posterior probability regions.

Linear + PPR	Mean	St. deviation	Best
Sensitivity (8 features)	63.94%	9.75%	88.89%
Specificity (8 features)	75.08%	12.28%	100.00%
Accuracy (8 features)	68.61%	9.05%	93.54%
Sensitivity (12 features)	68.17%	9.63%	88.89%
Specificity (12 features)	77.23%	12.17%	92.31%
Accuracy (12 features)	71.97%	8.71%	90.32%

highest value given is 61% of specificity, for 12 features. Accuracy does not move from values around 57-58% that is quite lower that actual models based only on BMD that achieves an accuracy around 65% (see Section 1). Linear kernel returns sensibly higher results, but nothing considerable good: while specificity increases around 75-77%, the sensitivity is still lower than 70%. Following, the maximum accuracy is lower than 72%.

Table 13: Results of SVM with a sigmoid kernel.

Sigmoid	Mean	St. deviation	Best
Sensitivity (8 features)	56.33%	12.61%	77.78%
Specificity (8 features)	60.62%	14.35%	84.61%
Accuracy (8 features)	58.13%	9.17%	80.65%
Sensitivity (12 features)	56.50%	12.41%	66.67%
Specificity (12 features)	60.77%	14.36%	100.00%
Accuracy (12 features)	58.29%	9.16%	80.65%

Table 14: Results of SVM with a sigmoid kernel and posterior probability regions.

Sigmoid + PPR	Mean	St. deviation	Best
Sensitivity (8 features)	55.39%	12.37%	77.78%
Specificity (8 features)	59.23%	14.40%	84.62%
Accuracy (8 features)	57.00%	10.09%	80.65%
Sensitivity (12 features)	55.94%	11.23%	83.33%
Specificity (12 features)	58.38%	15.66%	69.23%
Accuracy (12 features)	56.97%	8.67%	77.41%

Table 15: Results of SVM with a Bayesian kernel and posterior probability regions.

Bayesian + PPR	Mean	St. deviation	Best
Sensitivity (8 features)	56.67%	2.48%	55.56%
Specificity (8 features)	80.00%	6.88%	84.62%
Accuracy (8 features)	66.45%	2.89%	67.74%
Sensitivity (12 features)	71.11%	3.51%	77.78%
Specificity (12 features)	80.77%	8.31%	92.31%
Accuracy (12 features)	75.16%	4.57%	83.87%

Table 16: Results of SVM with a Gaussian kernel.

Gaussian	Mean	St. deviation	Best
Sensitivity (8 features)	82.56%	9.24%	88.89%
Specificity (8 features)	66.31%	14.90%	100.00%
Accuracy (8 features)	75.74%	8.23%	93.54%
Sensitivity (12 features)	96.22%	5.05%	100.00%
Specificity (12 features)	58.08%	15.09%	76.92%
Accuracy (12 features)	80.23%	6.96%	90.32%

Table 17: Results of SVM with a Gaussian kernel and posterior probability regions.

Gaussian + PPR	Mean	St. deviation	Best
Sensitivity (8 features)	86.22%	9.39%	100.00%
Specificity (8 features)	63.38%	15.35%	100.00%
Accuracy (8 features)	76.65%	8.97%	100.00%
Sensitivity (12 features)	93.67%	5.91%	100.00%
Specificity (12 features)	62.92%	16.56%	92.31%
Accuracy (12 features)	80.77%	7.57%	96.77%

Table 18: Results of Decision Trees.

Decision Tree	Mean	St. deviation	Best
Sensitivity (8 features)	59.22%	13.91%	88.89%
Specificity (8 features)	73.08%	12.46%	84.62%
Accuracy (8 features)	65.03%	8.85%	87.10%
Sensitivity (12 features)	59.67%	15.46%	99.44%
Specificity (12 features)	74.46%	18.09%	92.31%
Accuracy (12 features)	65.87%	11.66%	93.55%

Table 19: Results of Random Forest.

	8 features	12 features
Sensitivity	79.50	83.33%
Specificity	87.75	92.31%
Accuracy	82.66	87.10%

Bayesian kernel, along with PPR, increases a little bit the numbers: considering 12 features, the sensitivity is around 71%, the specificity is 10% higher, and the accuracy overreaches the 75%. Finally, using a Gaussian kernel, the sensitivity builds on a lot, reaching values up to 83% (8 features) and for the simple elaboration, and almost 94% for the Gaussian + PPR, handling 12 features. Both with and without PPR, the accuracy overreached 80% of accuracy.This is the best result obtained for the SVM modeling and reaches levels of the state of the art published to date (see Section 1).

On the other hand, Decision Trees do not return good results. Generally, the values for sensitivity, specificity, and accuracy are lower than SVM (considering the best fitting kernels). On the other hand, the standard deviation is sensibly greater (in average) than all the previous models, being the weak spot of this model. Accuracy is good, but sensitivity and specificity are unbalanced, in favor of the latter. For both 8 and 12 predictive attributes selected, the accuracy is around 65-66%.

Finally, Random Forest is the best among all the built models. Although the model built with only 8 features is less precise (around 5% for each value) than the one built with 12, it outrages the results obtained by models published until now. We have also observed that adding more attributes (up to 15), the results do not improve significantly, so the best move is to keep 12 features to grant a lighter dataset. In conclusion, neither of the previous models obtain such great results: 83% for sensitivity, 92% for specificity, and an accuracy of 87%.

As it was commented in Section 1, this paper enhances the study presented in [24]. The same clinical, geometric, and biomechanical variables of the previous database were used in this paper. However, this paper presents some novelties that improve our previous work. One of them is the relevance ranking carrying out to find out which variables are the most important ones for the problem. In our previous work, this ranking was performed only studying Pearson's correlation. In the present work, the relevance ranking was performed in two steps: Principal Component Analysis (PCA) and correlation analysis, analyzing both Pearson's

correlation index and Spearman's Rank correlation. However, the true improvement was obtained by the Principal Component Analysis.

As PCA is based on a reduction of the problem dimensions keeping the maximum information, our models are more precise, with more capability of generalization to be applied to new data and with more capability of interpretation for the post-processing of the results.

Another improvement is related to the application of the SMOTE technique in order to increase the number of training samples, which improved the results of our models. Finally, ML models different to those used in our previous work were used in this work as Decision Trees (DT) and Random Forest (RF), which provided with better results in terms of sensitivity, specificity, and accuracy. In fact, RF was the best option with an accuracy over 87%, specificity over 92%, and sensitivity over 83%. These values are much better than the current BMD clinically used whose classification accuracy is around 65% and also better than the accuracy of our previous work that was of 79%.

One of the main limitations of the present study was the sample size. Although the sample size was larger than other studies, it is still not larger enough, which might limit the learning process. Another of the limitation of this study is related to the resolution of the images. Pixel size was approximately 8 times greater than in other commercial densitometers (e.g., GE Healthcare iDXA Advance), thus providing low resolution images. The discriminative power of FEM-derived attributes highly depends on the material properties, which are extracted from the BMD maps. The details of these maps depend on the quality of the image, and if the image resolution is low, some information might have been lost.

There exits an inherent limitation in the present study due to the 2D model, which is developed on the overlapping of cortical and trabecular bone on the image plane. Therefore, stress and strain distributions may be altered, and the failure starting location might not be fully reliable. On the other hand, as it was commented previously, we could not construct ML models that differentiate between neck and trochanteric fractures due to the size of the dataset. Finally, although our study focused on prediction of hip fracture in postmenopausal women, hip fracture also happens in the male population [41]. Moreover, differences between male and female fracture attributes, both clinic and biomechanical, have been shown in the literature. This should be addressed in order to build an effective predictive model for both genders.

5. Conclusions

This paper proposes the use of Machine Learning (ML) models trained with data from a biomechanical model that simulates a sideway fall, aimed at improving the accuracy of the current gold-standard in osteoporosis clinical assessment. The current gold standard is Bone Mineral Density (BMD) measured by Dual-Energy X-Ray Absorptiometry (DXA), and its classification accuracy is only around 65%. Among the different tested models, Random Forest stands out, showing its capability to outperform BMD-DXA, achieving an accuracy over 87%, with specificity over 92% and sensitivity over 83%.

This paper enhances the study presented in [24]. The same clinical, geometric, and biomechanical variables of the previous database were also used in this work. However, this paper presents some novelties that improve it, as the relevance ranking carried out to find out the most important ones for the problem, which was performed by PCA. Thus, the models developed in this work were more precise, with more capability of generalization to be applied to new data and with more capability of interpretation for the postprocessing of the results.

The application of the SMOTE technique to increase the number of training samples also improved the models. In addition, different ML models to those used in our previous work were used in this work: Decision Trees (DT) and Random Forest (RF), which provided with better results in terms of sensitivity, specificity, and accuracy. These values were much better than the current BMD clinically used whose classification accuracy is around 65% and also better than the accuracy of our previous work that was of 79%.In conclusion, this study has shown that hip fracture prediction can be modelled by a multitechnique approach, considering clinical and biomechanical data into a ML classifier. This approach is economical and fast and could be integrated in the clinical routine without changing the clinical workflow. Future research works should include a greater 480 volume of samples, better image quality, and more specific predictions of the fracture location.

Data Availability

The data used to support the findings of this study are restricted by ASCIRES company in order to protect patient privacy. Data are available from María José Rupérez for researchers who meet the criteria for access to confidential data.

Conflicts of Interest

All authors state that they have no conflicts of interest.

Acknowledgments

This study was partially funded by the FPI grant (FPI-SP20170111) from the Universitat Politècnica de València obtained by Eduardo Villamor.

References

[1] World Health Organization, "Assessment of fracture risk and its application to screening for postmenopausal osteoporosis. Report of a WHO Study Group," 1994, http://www.who.int/iris/handle/10665/39142, http://apps.who.int//iris/handle/10665/39142.

[2] C. Cooper, G. Campion, and L. J. Melton, "Hip fractures in the elderly: a world-wide projection," *Osteoporosis International*, vol. 2, no. 6, pp. 285–289, 1992.

[3] A. El Maghraoui and C. Roux, "DXA scanning in clinical practice," *QJM*, vol. 101, no. 8, pp. 605–617, 2008.

[4] D. Testi, M. Viceconti, A. Cappello, and S. Gnudi, "Prediction of hip fracture can be significantly improved by a single biomedical indicator," *Annals of Biomedical Engineering*, vol. 30, no. 6, pp. 801–807, 2002.

[5] N. D. Nguyen, S. A. Frost, J. R. Center, J. A. Eisman, and T. V. Nguyen, "Development of prognostic nomograms for individualizing 5-year and 10-year fracture risks," *Osteoporosis International*, vol. 19, no. 10, pp. 1431–1444, 2008.

[6] J. A. Kanis, A. Oden, H. Johansson, F. Borgström, O. Ström, and E. McCloskey, "FRAX® and its applications to clinical practice," *Bone*, vol. 44, no. 5, pp. 734–743, 2009.

[7] M. J. Bolland, A. T. Siu, B. H. Mason et al., "Evaluation of the FRAX and Garvan fracture risk calculators in older women," *Journal of Bone and Mineral Research*, vol. 26, no. 2, pp. 420–427, 2011.

[8] N. Li, X.-M. Li, L. Xu, W.-J. Sun, X.-G. Cheng, and W. Tian, "Comparison of QCT and DXA: Osteoporosis Detection Rates in Postmenopausal Women," *International Journal of Endocrinology*, vol. 2013, Article ID 895474, 5 pages, 2013.

[9] G. Fountoulis, T. Kerenidi, C. Kokkinis et al., "Assessment of bone mineral density in male patients with chronic obstructive pulmonary disease by DXA and quantitative computed tomography," *International Journal of Endocrinology*, vol. 2016, Article ID 6169721, 6 pages, 2016.

[10] O. J. Pellicer-Valero, M. J. Rupérez, S. Martínez-Sanchis, and J. D. Martín-Guerrero, "Real-time biomechanical modeling of the liver using machine learning models trained on finite element method simulations," *Expert Systems with Applications*, vol. 143, article 113083, 2020.

[11] F. Martínez-Martínez, M. J. Rupérez-Moreno, M. Martínez-Sober et al., "A finite element-based machine learning approach for modeling the mechanical behavior of the breast tissues under compression in real-time," *Computers in Biology and Medicine*, vol. 90, pp. 116–124, 2017.

[12] T. Davenport and R. Kalakota, "The potential for artificial intelligence in healthcare," *Future Healthcare Journal*, vol. 6, no. 2, pp. 94–98, 2019.

[13] C. Kruse, P. Eiken, and P. Vestergaard, "Clinical fracture risk evaluated by hierarchical agglomerative clustering," *Osteoporosis International*, vol. 28, no. 3, pp. 819–832, 2017.

[14] T. P. Ho-Le, J. R. Center, J. A. Eisman, T. V. Nguyen, and H. T. Nguyen, "Prediction of hip fracture in post-menopausal women using artificial neural network approach," in *2017 39th Annual International Conference of the IEEE Engineering in Medicine and Biology Society (EMBC)*, pp. 4207–4210, Seogwipo, South Korea, July 2017.

[15] E. Dall'Ara, R. Eastell, M. Viceconti, D. Pahr, and L. Yang, "Experimental validation of DXA-based finite element models for prediction of femoral strength," *Journal of the Mechanical Behavior of Biomedical Materials*, vol. 63, pp. 17–25, 2016.

[16] W. S. Enns-Bray, H. Bahaloo, I. Fleps et al., "Biofidelic finite element models for accurately classifying hip fracture in a retrospective clinical study of elderly women from the AGES Reykjavik cohort," *Bone*, vol. 120, pp. 25–37, 2019.

[17] D. Testi, M. Viceconti, F. Baruffaldi, and A. Cappello, "Risk of fracture in elderly patients: a new predictive index based on bone mineral density and finite element analysis," *Computer Methods and Programs in Biomedicine*, vol. 60, no. 1, pp. 23–33, 1999.

[18] L. Yang, L. Palermo, D. M. Black, and R. Eastell, "Prediction of incident hip fracture with the estimated femoral strength by finite element analysis of DXA scans in the study of osteoporotic fractures," *Journal of Bone and Mineral Research*, vol. 29, no. 12, pp. 2594–2600, 2014.

[19] Y. Luo, S. Ahmed, and W. D. Leslie, "Automation of a DXA-based finite element tool for clinical assessment of hip fracture risk," *Computer Methods and Programs in Biomedicine*, vol. 155, pp. 75–83, 2018.

[20] M. Terzini, A. Aldieri, L. Rinaudo, G. Osella, A. L. Audenino, and C. Bignardi, "Improving the hip fracture risk prediction through 2D finite element models from DXA images: validation against 3D models," *Frontiers in Bioengineering and Biotechnology*, vol. 7, p. 220, 2019.

[21] K. K. Nishiyama, M. Ito, A. Harada, and S. K. Boyd, "Classification of women with and without hip fracture based on quantitative computed tomography and finite element analysis," *Osteoporosis International*, vol. 25, no. 2, pp. 619–626, 2014.

[22] P. Jiang, S. Missoum, and Z. Chen, "Fusion of clinical and stochastic finite element data for hip fracture risk prediction," *Journal of Biomechanics*, vol. 48, no. 15, pp. 4043–4052, 2015.

[23] U. Ferizi, H. Besser, P. Hysi et al., "Artificial intelligence applied to osteoporosis: a performance comparison of machine learning algorithms in predicting fragility fractures from MRI data," *Journal of Magnetic Resonance Imaging*, vol. 49, no. 4, pp. 1029–1038, 2019.

[24] E. Villamor, C. Monserrat, L. Del Río, J. A. Romero-Martín, and M. J. Rupérez, "Prediction of osteoporotic hip fracture in postmenopausal women through patient-specific FE analyses and machine learning," *Computer Methods and Programs in Biomedicine*, vol. 193, article 105484, 2020.

[25] A. E. H. Love, *A treatise on the mathematical theory of elasticity*, Dover Publications, 1944, https://books.google.es/books/about/A{_}Treatise{_}on{_}the{_}Mathematical{_}Theory{_}of.html?id=z8rCbeD{_}MrYC{&}source=kp{_}cover{&}redir{_}esc=y.

[26] T. Rossman, V. Kushvaha, and D. Dragomir-Daescu, "QCT/FEA predictions of femoral stiffness are strongly affected by boundary condition modeling," *Computer Methods in Biomechanics and Biomedical Engineering*, vol. 19, no. 2, pp. 208–216, 2015.

[27] H. Si, "TetGen, a Delaunay-based quality tetrahedral mesh generator," *ACM Transactions on Mathematical Software*, vol. 41, no. 2, pp. 1–36, 2015.

[28] E. F. Morgan and T. M. Keaveny, "Dependence of yield strain of human trabecular bone on anatomic site," *Journal of Biomechanics*, vol. 34, no. 5, pp. 569–577, 2001.

[29] E. F. Morgan, H. H. Bayraktar, and T. M. Keaveny, "Trabecular bone modulus-density relationships depend on anatomic site," *Journal of Biomechanics*, vol. 36, no. 7, pp. 897–904, 2003.

[30] H. H. Bayraktar, E. F. Morgan, G. L. Niebur, G. E. Morris, E. K. Wong, and T. M. Keaveny, "Comparison of the elastic and yield properties of human femoral trabecular and cortical bone tissue," *Journal of Biomechanics*, vol. 37, no. 1, pp. 27–35, 2004.

[31] D. C. Wirtz, N. Schiffers, T. Pandorf, K. Radermacher, D. Weichert, and R. Forst, "Critical evaluation of known bone material properties to realize anisotropic FE-simulation of the proximal femur," *Journal of Biomechanics*, vol. 33, no. 10, pp. 1325–1330, 2000.

[32] F. Eckstein, C. Wunderer, H. Boehm et al., "Reproducibility and side differences of mechanical tests for determining the structural strength of the proximal femur," *Journal of Bone and Mineral Research*, vol. 19, no. 3, pp. 379–385, 2003.

[33] E. S. Orwoll, L. M. Marshall, C. M. Nielson et al., "Finite element analysis of the proximal femur and hip fracture risk in older men," *Journal of Bone and Mineral Research*, vol. 24, no. 3, pp. 475–483, 2009.

[34] S. A. Maas, B. J. Ellis, G. A. Ateshian, and J. A. Weiss, "FEBio: finite elements for biomechanics," *Journal of Biomechanical Engineering*, vol. 134, no. 1, article 011005, 2012.

[35] S. Abe, A. Ylinen, N. Narragirish et al., "Exploration of different boundary conditions in the sideways falling situation in hip fracture finite element modeling," in *Proceedings of the XII Finnish Mechanics Days*, pp. 130–135, Tampere, Finland, 2015, http://meshlab.sourceforge.net/.

[36] W. J. Choi, P. A. Cripton, and S. N. Robinovitch, "Effects of hip abductor muscle forces and knee boundary conditions on femoral neck stresses during simulated falls," *Osteoporosis International*, vol. 26, no. 1, pp. 291–301, 2015.

[37] A. J. van den Kroonenberg, W. C. Hayes, and T. A. McMahon, "Dynamic models for sideways falls from standing height," *Journal of Biomechanical Engineering*, vol. 117, no. 3, pp. 309–318, 1995.

[38] S. N. Robinovitch, T. A. McMahon, and W. C. Hayes, "Force attenuation in trochanteric soft tissues during impact from a fall," *Journal of Orthopaedic Research*, vol. 13, no. 6, pp. 956–962, 1995.

[39] A. B. Dufour, B. Roberts, K. E. Broe, D. P. Kiel, M. L. Bouxsein, and M. T. Hannan, "The factor-of-risk biomechanical approach predicts hip fracture in men and women: the Framingham Study," *Osteoporosis International*, vol. 23, no. 2, pp. 513–520, 2012.

[40] K. W. Bowyer, N. V. Chawla, L. O. Hall, and W. P. Kegelmeyer, "SMOTE: synthetic minority over-sampling technique-CoRRhttps://arxiv.org/abs/1106.1813.

[41] E. Villamor, J. A. Romero-Martín, C. Monserrat, and M. J. Rupérez, "Desarrollo de una herramienta de software para la evaluación automática del riesgo de fractura de cadera basada en modelos biomecánicos paciente-específico, VIII Reunión del Capítulo Español de la Sociedad Europea de Biomecánica (ESB)," pp. 40-41, 2018, http://repositori.uji.es/xmlui/handle/10234/180657.